CRREL
REPORT 87-10

US Army Corps
of Engineers
Cold Regions Research &
Engineering Laboratory

Creep and strength behavior of frozen silt in uniaxial compression

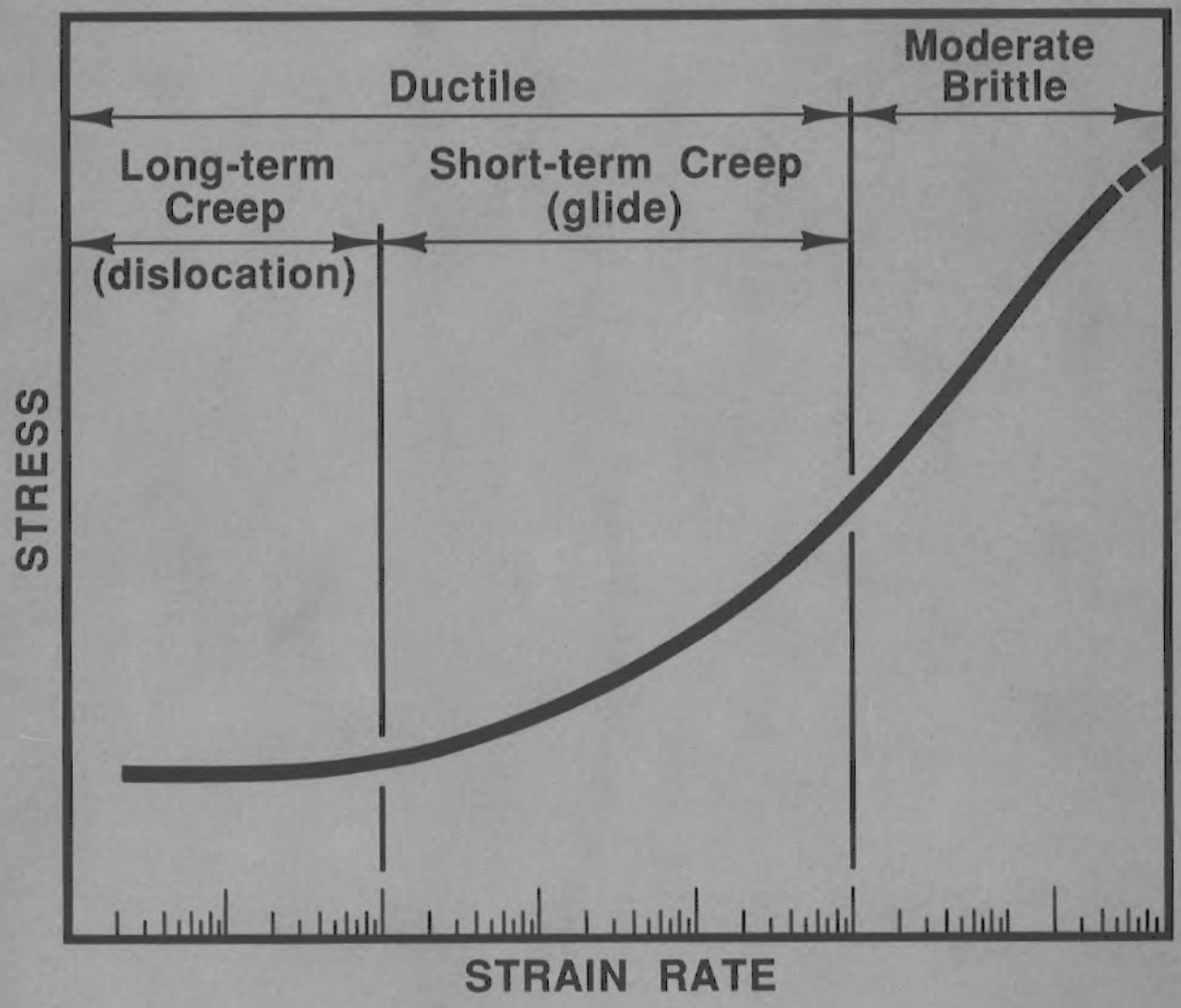

CRREL Report 87-10

July 1987

Creep and strength behavior of frozen silt in uniaxial compression

Zhu Yuanlin and David L. Carbee

Unclassified

SECURITY CLASSIFICATION OF THIS PAGE

REPORT DOCUMENTATION PAGE

Form Approved
OMB No. 0704-0188
Exp. Date: Jun 30, 1986

1a. REPORT SECURITY CLASSIFICATION Unclassified	1b. RESTRICTIVE MARKINGS
2a. SECURITY CLASSIFICATION AUTHORITY	3. DISTRIBUTION / AVAILABILITY OF REPORT
2b. DECLASSIFICATION / DOWNGRADING SCHEDULE	
4. PERFORMING ORGANIZATION REPORT NUMBER(S) CRREL Report 87-10	5. MONITORING ORGANIZATION REPORT NUMBER(S)
6a. NAME OF PERFORMING ORGANIZATION U.S. Army Cold Regions Research and Engineering Laboratory 6b. OFFICE SYMBOL (If applicable) CECRL	7a. NAME OF MONITORING ORGANIZATION
6c. ADDRESS (City, State, and ZIP Code) Hanover, New Hampshire 03755-1290	7b. ADDRESS (City, State, and ZIP Code)
8a. NAME OF FUNDING / SPONSORING ORGANIZATION 8b. OFFICE SYMBOL (If applicable)	9. PROCUREMENT INSTRUMENT IDENTIFICATION NUMBER
8c. ADDRESS (City, State, and ZIP Code)	10. SOURCE OF FUNDING NUMBERS PROGRAM ELEMENT NO. / PROJECT NO 4A1611 01A91D / TASK NO. 00 / WORK UNIT ACCESSION NO 397

11. TITLE (Include Security Classification)
Creep and Strength Behavior of Frozen Silt in Uniaxial Compression

12. PERSONAL AUTHOR(S)
Zhu Yuanlin and David L. Carbee

13a. TYPE OF REPORT	13b. TIME COVERED FROM _____ TO _____	14. DATE OF REPORT (Year, Month, Day)	15. PAGE COUNT
		July 1987	75

16. SUPPLEMENTARY NOTATION

17. COSATI CODES			18. SUBJECT TERMS (Continue on reverse if necessary and identify by block number)
FIELD	GROUP	SUB-GROUP	Frozen soils; Stress-strain relations; Silt; Soil tests

19. ABSTRACT (Continue on reverse if necessary and identify by block number)

Uniaxial constant-stress and constant-strain-rate compression tests were conducted on more than 200 remolded, saturated, frozen specimens of Fairbanks silt under various conditions. A series of curves of stress vs strain rate for various temperatures for strain rates ranging from about 6×10^{-2} to 10^{-8} s^{-1} show a close strength correspondence between the constant-stress and constant-strain-rate tests. All of these "complete" stress vs strain rate curves could not be described by a single power law or exponential equation, indicating that different deformation mechanisms are dominant within different ranges of strain rate. Two critical strain rates for distinguishing between the different deformation mechanisms were observed to be near 10^{-3} and 10^{-6} s^{-1} for the medium-dense frozen Fairbanks silt. The former indicates the transition from ductile failure to moderate brittle fracture as strain rate increases, while the latter indicates the transition from dislocation creep to glide creep (by the authors' definition). Based on the changes in flow law, two fundamental creeps were classified: short-term creep, which is governed by glide creep, and long-term creep, which is governed by dislocation creep. The failure criterion of frozen silt has a general form of $\dot{\varepsilon}_m \times t_m^m = \varepsilon_f$, where m depends only on density, and t_m is in minutes if m is not 1. The failure

20. DISTRIBUTION / AVAILABILITY OF ABSTRACT	21. ABSTRACT SECURITY CLASSIFICATION
☒ UNCLASSIFIED/UNLIMITED ☐ SAME AS RPT ☐ DTIC USERS	Unclassified
22a. NAME OF RESPONSIBLE INDIVIDUAL David Carbee	22b. TELEPHONE (Include Area Code) 603-646-4477 / 22c. OFFICE SYMBOL CECRL-EG

DD FORM 1473, 84 MAR — 83 APR edition may be used until exhausted. All other editions are obsolete.

SECURITY CLASSIFICATION OF THIS PAGE
Unclassified

19. Abstract (cont'd)

strain ε_f was not sensitive to temperature and strain rate over a certain range of strain rates, but it was very sensitive to density. Assur's creep model (1980) for ice was used to fit the creep data in this study. It works well for short-term creep but does not fit as well for long-term creep. The rate process theory was applied to the creep data. A very high value of experimental activation energy was obtained for lower stresses, and a very high value of apparent activation energy was observed for higher temperatures. The peak compressive strength was very sensitive to temperature and strain rate but relatively insensitive to density. While the initial tangent modulus is not sensitive to strain rate, it increases with decreasing temperature and density.

PREFACE

This report was prepared by Zhu Yuanlin, a visiting associate professor on leave from Lanzhou Institute of Glaciology and Geocryology, Academia Sinica, Lanzhou, China, and David L. Carbee, Civil Engineering Technician, Geotechnical Research Branch, Experimental Engineering Division, U.S. Army Cold Regions Research and Engineering Laboratory.

The study was funded through an FY83-84 ILIR (in-house laboratory independent research) program at CRREL titled "Mechanical Properties of Frozen Silt." The objective was to investigate uniaxial and triaxial compressive strength and creep behavior and also uniaxial tensile strength of frozen, remolded Fairbanks tunnel silt under varying test conditions (temperature, stress, strain rate and physical properties). The results will be published in three CRREL reports. This report covers the results of the comprehensive portion on uniaxial compression strength and creep tests.

The authors appreciate the technical advice from Dr. Andrew Assur, William Quinn, Edwin Chamberlain, Francis Sayles, David Cole and Dr. Malcolm Mellor. They also thank the support staff of the CRREL Soils Laboratory, John Bayer and J. Rajkowski, and they appreciate the machine operation and instrumentation assistance from Glenn Durell. This report was technically reviewed by F. Sayles and E. Chamberlain, CRREL. The final review prior to publication was done by Dr. Yin-Chao Yen, CRREL. The authors thank the reviewers for their constructive comments and suggestions.

CONTENTS

ILLUSTRATIONS

TABLES

Creep and Strength Behavior of Frozen Silt in Uniaxial Compression

ZHU YUANLIN AND DAVID L. CARBEE

INTRODUCTION

The design of stable structures in cold regions requires an understanding of the creep and strength behavior of frozen soils. While many researchers have studied this subject for a long time, detailed studies are still required to gain a better understanding of the subject. The presence of ice and unfrozen water in frozen soil makes its stress–strain–strength behavior to be strongly time and temperature dependent because the phase equilibrium between ice and unfrozen water is controlled by temperature and the stress state. This temperature and stress dependency can be evaluated in the laboratory using either constant-stress or constant-strain-rate tests. Mellor (1980) pointed out that there is a correspondence between these two test methods for ice, making them interchangeable. Ladanyi (1981) reported that this was also true for frozen soil.

The purposes of this study were to evaluate the influences of applied stress (or applied strain rate) and temperature on the strength and creep behavior of frozen soil and to systematically investigate the correspondence of results obtained by constant-strain-rate and constant-stress tests.

These tests were conducted on a frozen silt at seven temperatures ranging from –0.5° to –10°C and three nominal densities ranging from 1.08 to 1.40 g/cm^3. The constant-stress creep tests were conducted at stress levels causing test durations from a few minutes to more than two months. Constant-head velocity tests were employed in lieu of constant-strain-rate tests because of difficulties in the testing procedures. The resulting average strain rates ranged from 1.1×10^{-6} to 6.2×10^{-2} s^{-1}.

This report presents representative test results, the analysis of the stress–strain–temperature relationships, and the determination of the correspondence of the constant-stress and constant-strain-rate test results. Readers interested in the raw data and graphs are referred to Zhu and Carbee (1983) available at the U.S. Army Cold Regions Research and Engineering Laboratory.

REVIEW OF PREVIOUS WORK

Since Tsytovich published the first paper reporting a study of the mechanical properties of frozen soil in 1930, numerous investigations in this field have been published. In 1937 and 1952, Tsytovich and his co-workers published two monographs in which the fundamental principles of frozen soil mechanics were first set forth. In 1952, the Arctic Construction and Frost Effects Laboratory (ACFEL) published a report summarizing test data obtained up to that time, including the results of ACFEL investigations. In later years, Tsytovich (1954,

1958) and Vialov (1959, 1962, 1963) published rather complete data on the strength and deformational properties of both remolded and undisturbed frozen soils. These publications summarized and formulated qualitative theories and empirical equations describing strength and deformation of frozen soil as a function of temperature and duration of load application. These results are still widely used in engineering practice. Meanwhile, Sanger and Kaplar (1963) published unconfined compression creep test data on a variety of soils at various temperatures from 0° to -7.8°C, and presented empirical equations relating creep strain and strain rate to applied stress and temperature.

To apply the rate process theory (RPT) to the creep process of frozen soil, Andersland and Akili (1967) performed unconfined compression creep tests on a partially saturated frozen clay and arrived at an activation energy of 93.1 kcal/mole for a stress range of 42.2–56.3 kg/cm^2 and temperature range of -12° to -18°C. They presented an empirical equation for predicting strain rate based on the RPT. Mitchell et al. (1968) and others have shown that the temperature and stress dependency qualitatively fit RPT predictions very well. Goughnour and Andersland (1968) published unconfined compression strength and creep data for ice and Ottawa sand-ice samples with various volumetric ratios. An empirical equation relating creep rate to stress, temperature, strain and strain energy was fitted to the ice sample data. Using this equation for ice and the stress-strain curves for Ottawa sand-ice samples, they plotted creep curves for sand-ice specimens by means of stress factors. The stress factors were related to the percent of sand by volume. Sayles (1968) and Sayles and Haines (1974) published unconfined compression creep data for frozen Ottawa sand, Manchester fine sand, Suffield clay, Hanover silt and columnar-grained ice for temperatures ranging from -0.56° to -9.45°C. Sayles found that Vialov's creep equation fit the test data very well. He also developed a simplified method for predicting creep deformation that also provided a good fit to the test data.

Combining classical creep theories for metals and existing creep theories for frozen soil, Ladanyi (1972) developed a macroanalytical secondary creep model (an engineering theory of creep) for frozen soil, which is simpler than Vialov's primary creep model for predicting long-term creep deformation and strength of frozen silt. Moreover, Vialov (1973) established a micromechanistic theory of creep deformation and failure of clayey soil based on an investigation of the kinetics of changes in the soil microstructure. The proposed equations for predicting creep deformation and long-term strength also fit their test data very well.

In the past decade, CRREL has published many reports on constant-strain-rate compression tests on frozen soils. Sayles (1974) published constant-strain-rate tests on frozen silt and clay at an average strain rate of 0.14–0.15 min^{-1}. Empirical power-law equations were presented to evaluate the peak (maximum) compressive strength and the 50% peak strength modulus as a function of temperature. Haynes et al. (1975) investigated the strain rate effect on the strength of frozen Fairbanks silt at -9.4°C. They concluded that the unconfined compressive strength is very sensitive to strain rate and increased 10 times over a strain rate range of 2.9×10^{-4} to 2.9 s^{-1}. They reported, however, that the initial tangent modulus is not very sensitive to strain rate and has a magnitude ranging from 10^4 to 2.2×10^5 kg/cm^2. Later, Haynes and Karalius (1977) studied the effect of temperature on the strength of the silt at machine speeds of 0.0423 and 4.23 cm/s. They pointed out that both the strength and the initial tangent modulus are very sensitive to temperature, and they increased about one order of magnitude as the temperature was lowered from 0° to -56.7°C. Empirical equations relating the peak strength with unfrozen water content were also presented. Sayles and Carbee (1981) investigated the effect of ice content and dry unit weight on the strength of frozen Fairbanks silt at a strain rate of 5×10^{-3} s^{-1} and a temperature of -1.67°C. They found that the relationship between the compressive stress at the onset of fracturing and the dry unit weight was better defined than that between peak strength and dry unit weight, and the "ice matrix strength" was nearly proportional to the volumetric ice content of the soil.

More recently, a number of researchers evaluated the applicability of the rate process theory for frozen soil. Analyzing the kinetic nature of the long-term strength of frozen soils, Fish (1980) reported that the failure activation energy of frozen soils was relatively stable; it varied only from 12.9 to 19.7 kcal/mole in the temperature range from -0.55° to -20°C. Based on this analysis, Fish derived a unified constitutive equation that can describe the entire creep curve from the primary through the tertiary stage. This equation has a form similar to Assur's (1980) creep model for ice. Martin et al. (1981) and Ting (1981) published rather complete creep data for frozen Manchester fine sand and ice at a temperature range of -11° to -27°C. The free energy of activation was reported by Martin et al. (1981) to have a value of 114 kcal/mole for an ice saturation of 40% and 76 kcal/mole at 100%. A "tertiary" creep model similar to Assur's model was also developed by Fish (1980) and Ting (1981).

Zhu et al. (1982) reported an in-situ investigation of creep of massive ground ice with soil at a temperature of -0.4°C. A simple power law was suggested for describing the flow law of warm ground ice. Wu et al. (1982) published a comprehensive report summarizing the results of laboratory circular-footing creep tests for various frozen soils. They presented a number of empirical equations relating steady-state creep rate, time to failure and failure strain to applied stress, temperature and water content. A $t^{1/3}$ primary creep model fit decaying creep curves very well. A simple power-law strength-loss equation was also presented.

By analyzing the creep and strength test data on frozen sand (Martin et al. 1981, Ting 1981), Ting et al. (1983) proposed and quantified various mechanisms of strength of frozen sand.

SPECIMEN PREPARATION

Material

The material used in this investigation was a remolded silt from the CRREL experimental permafrost tunnel at Fox, near Fairbanks, Alaska. Its gradation curve is shown in Figure 1.

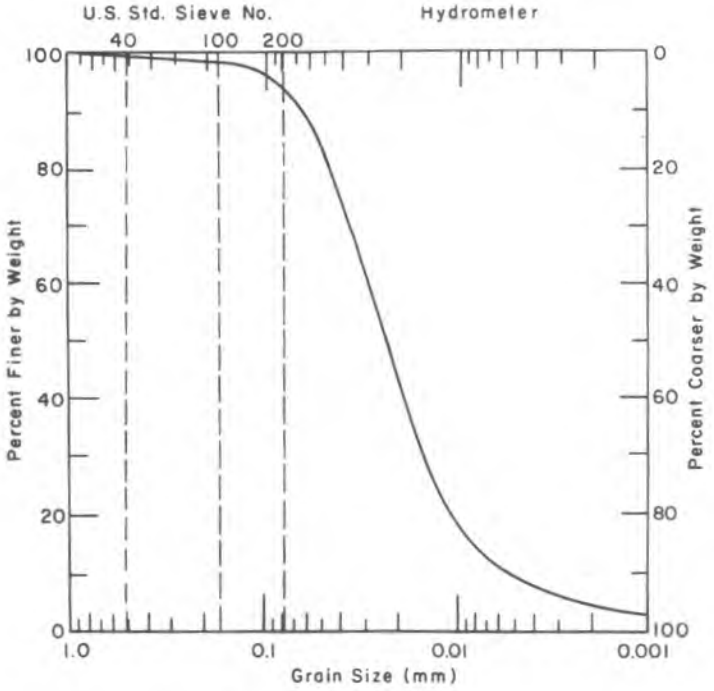

Figure 1. Gradation curve of Fairbanks silt.

Some of the physical properties of the silt are as follows:

Plastic limit	34.2%
Liquid limit	38.4%
Organic content	5.5%
Specific gravity	2.680
Specific surface area	35.0 m^2/g.

The silt is classified as ML using the Unified Soil Classification System. The relationship between unfrozen water content and temperature for this silt is shown in Appendix A.

Molding

Distilled water was added to 40 lb of air-dried Fairbanks silt to make an initial water content of 12% by weight. After storage overnight to allow for moisture equilibration, the moist soil was carefully compacted to the desired density in a gang mold. The mold, machined from acrylic plastic (Fig. 2), could form nineteen 7-cm-diameter by 19.3-cm-long specimens. A specially designed compactor was used to uniformly tamp the silt–water mixture in 12 layers, each layer having a thickness of 1.61 cm. Samples

Figure 2. Soil specimen gang mold.

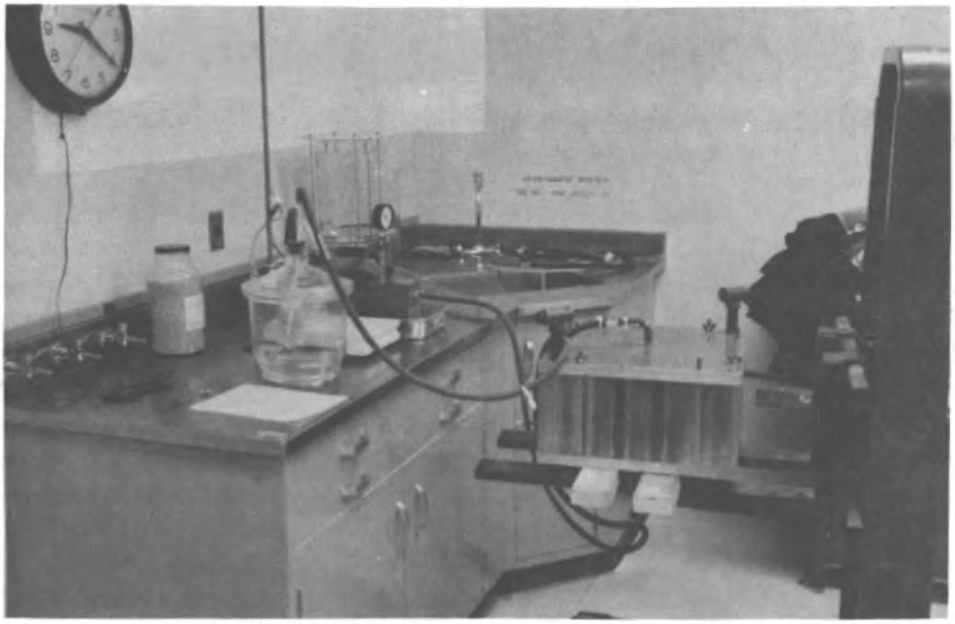

Figure 3. Set-up of saturation system.

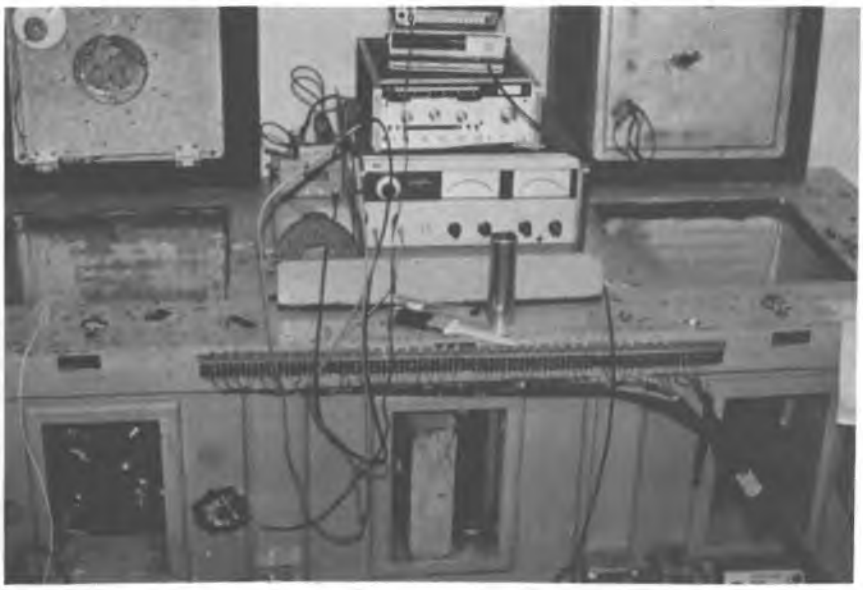

Figure 4. Freezing cabinet with free water channel through bottom.

were compacted to nominal dry densities of 1.08, 1.20 and 1.40 g/cm^3. These dry densities are referred to as low, medium and high in the remainder of this report.

After compaction the specimens were saturated with the deaerated, distilled water under a vacuum of 73 mm Hg. The saturation system set-up is shown in Figure 3.

The specimen-charged mold was then placed into a freezing cabinet (Fig. 4) and quickly frozen from the top down in an open system with an upper boundary temperature of lower than -30°C. To minimize the formation of ice lenses during freezing, the samples were cooled in the cabinet at 0°C overnight before freezing. Examination of the cut face of specimens revealed no visible ice lenses except for those specimens with the lowest density, in which some ice lenses can be seen, as shown in Figure 5.

After freezing, the specimens were ejected from the mold. One specimen from each mold was cut into three pieces to evaluate any density and water content variations. The results for the representative samples from 12 molds are shown in Table 1. For the specimens with medium and low density, the distribution of dry density and water content along the specimen length is quite uniform. However, for those specimens with high density (molds 12 and 13), a significant amount of water appears to have migrated towards the top of the specimen during freezing.

The remaining specimens were inspected for imperfections, and then the ends were carefully trimmed flat and parallel on a lathe in a coldroom (Fig. 6). The nominal size of the specimen after trimming was 70 mm in diameter by 152 mm long. The average squareness of the specimens ranged from 0.1 to 0.2 mm. The bulk density was determined, and each specimen was sealed with a piece of T-600 Series membrane and two steel end caps. Before testing, all specimens were tempered at the appropriate testing temperature for at least 48 hours.

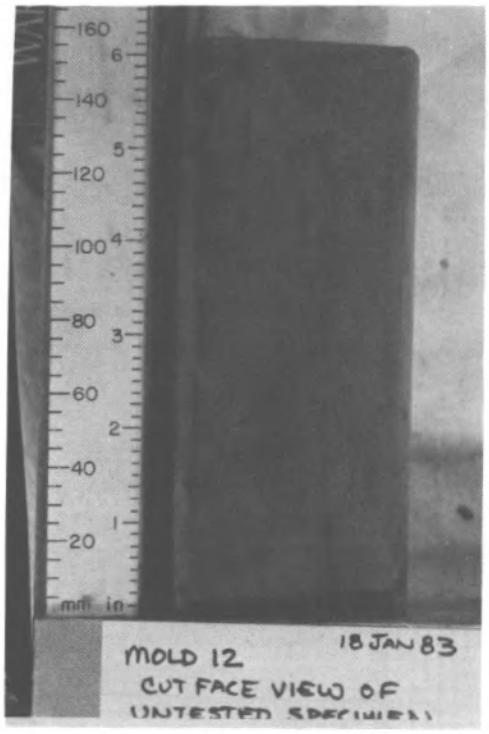

a. Medium-density specimen from mold 12, showing no ice lenses.

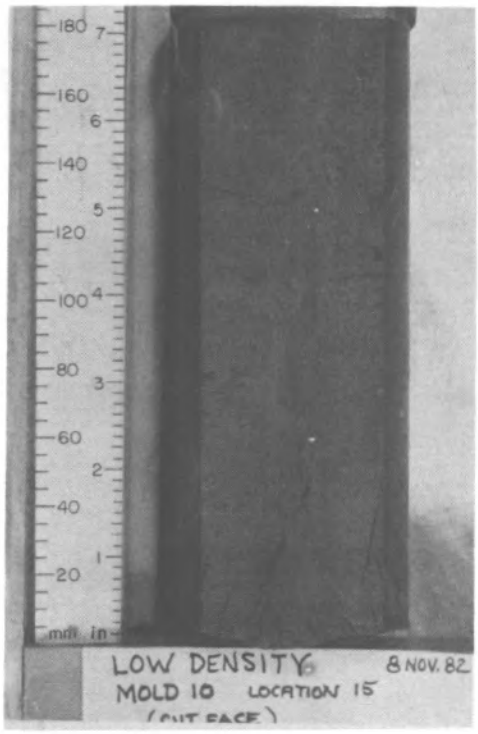

b. Low-density specimen from mold 10, showing some ice lenses.

Figure 5. Cut face of untested specimens.

Figure 6. Trimming a specimen on a lathe in a coldroom.

Table 1. Dry density and water content profile data for 12 molds.

Mold no.	Water content (%)			Dry density (g/cm³)		
	Top (0–5 cm)	Middle (5–10 cm)	Bottom (10–15 cm)	Top (0–5 cm)	Middle (5–10 cm)	Bottom (10–15 cm)
1	42.4	43.6	43.7	1.198	1.178	1.181
2	44.2	44.9	45.2	1.177	1.167	1.162
3	41.9	40.2	40.6	1.204	1.235	1.227
4	43.8	43.9	43.0	1.167	1.173	1.182
5	40.2	40.2	41.3	1.208	1.212	1.200
6	40.7	40.5	40.7	1.228	1.227	1.227
7	41.4	42.0	42.6	1.218	1.202	1.187
8	41.5	40.3	40.8	1.216	1.237	1.229
9	44.7	44.0	43.3	1.163	1.175	1.186
10	50.7	51.1	49.8	1.082	1.077	1.092
12	32.1	29.9	29.3	1.388	1.432	1.446
13	32.7	28.7	31.1	1.368	1.461	1.411

TESTING PROCEDURE AND APPARATUS

The uniaxial constant-stress creep tests were conducted using the constant-stress test apparatus (Fig. 7) designed by Sayles (1968). It allows the applied load to increase proportionally to the increase in the diameter as the specimen deforms so that the true stress remained constant during a test. The test results showed that the maximum deviation of the axial true stress from the initial applied stess is less than 1% of the initial stress during tests.

The major portion of the uniaxial constant-strain-rate test program was conducted in a coldroom on a screw-driven Instron universal testing machine installed with a temperature-controlled chamber (Fig. 8). Some tests with the highest machine speed (50 cm/min) were

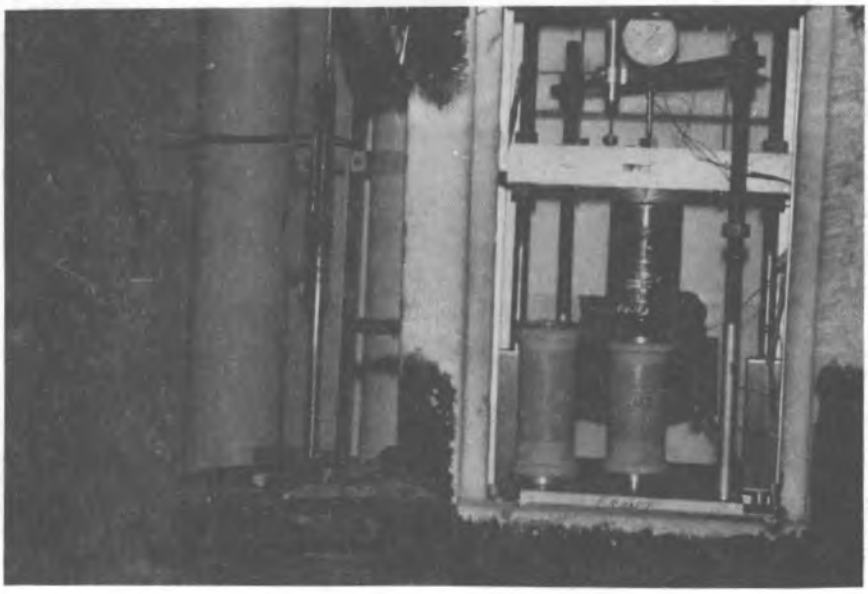

Figure 7. Constant-stress test apparatus.

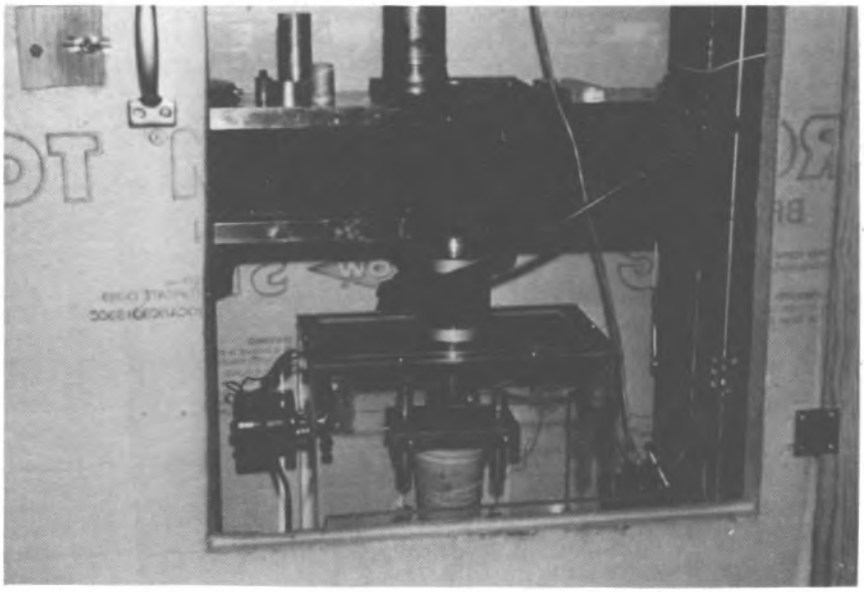

a. Temperature-controlled testing chamber.

b. Operating panel and recording system.

Figure 8. Instron universal testing machine model TT-CM-L with an environmental chamber.

performed on a closed-loop servo-controlled electrohydraulic MTS testing machine (Fig. 9). Temperature-controlled cabinets were employed to maintain the desired test temperature.

The applied axial loads were measured with various types of load cells according to their appropriate working ranges. The deformations were measured with Collins Corp. direct-current displacement transducers, which have a sensitivity of 2×10^{-5}.

For the creep tests and the constant-strain-rate tests conducted on the Instron universal

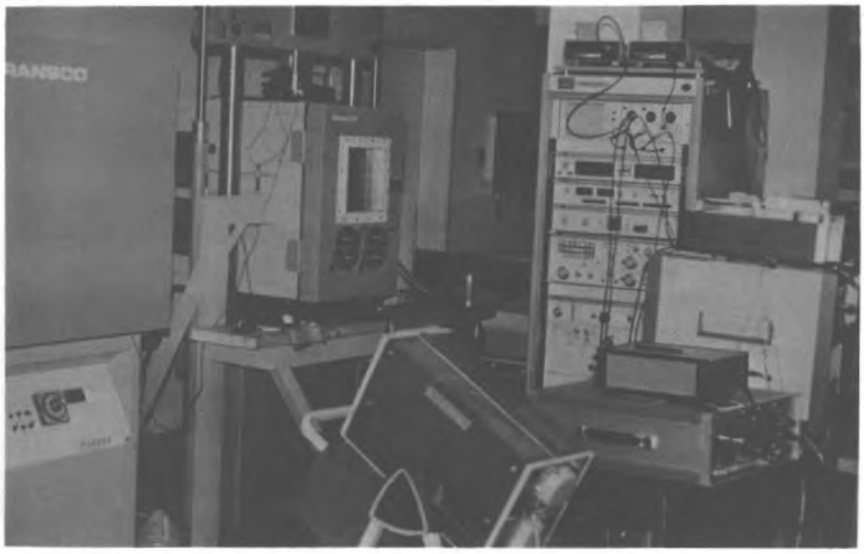

Figure 9. MTS machine and Ransco temperature-controlled cabinets.

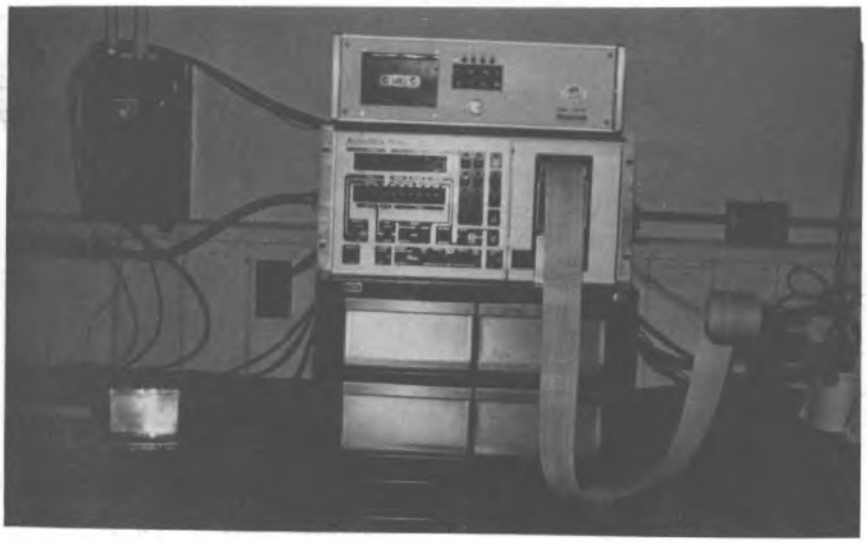

Figure 10. Autodata Nine data logger with a Memodyne tape recorder, model 3765-8BV.

machine in a coldroom, testing temperatures were controlled by a thermistor positioned inside the testing chamber around the specimens; the thermistor actuated a temperature controller to supply heat upon demand. For the constant-strain-rate tests performed on the closed-loop MTS machine, test temperatures were maintained by the Ransco refrigeration unit and the temperature-controlled cabinets. During tests, the environmental temperatures around specimens were measured by a thermistor with a sensitivity of 0.01℃. The observations showed that temperatures were held well within 0.05℃ of the desired values.

During a test, the applied load, deformation and temperature were recorded with a data logger, Autodata Nine (Fig. 10), or a strip-chart recorder, model 83373-30 (Fig. 11), or both.

After testing, the samples were photographed, and the bulk densities and water contents were determined.

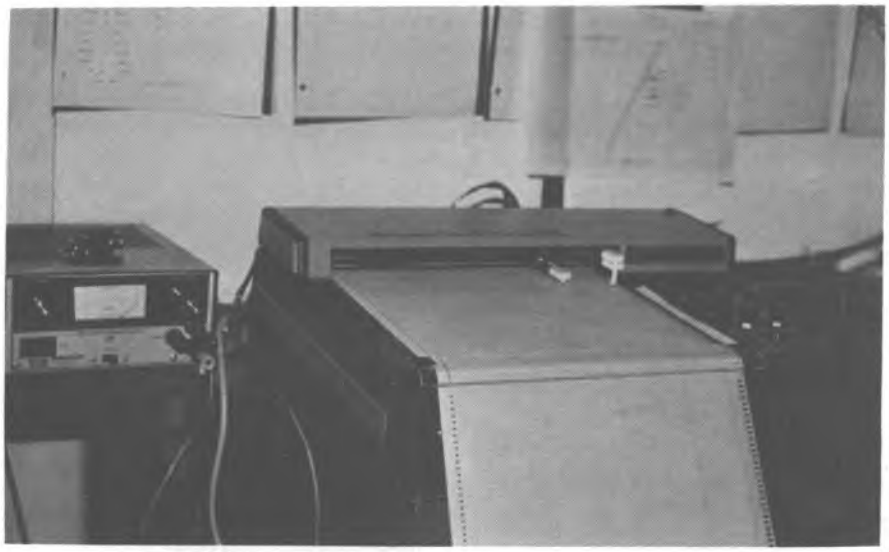

Figure 11. Strip-chart recorder, model 83373-30.

TEST RESULTS

The detailed test results and substantiating graphs for each specimen are available in a CRREL Internal Report entitled "Constant Stress and Constant Strain Rate Compression Test Data of Frozen Fairbanks Silt" (Zhu and Carbee 1983). The complete raw data can be found on magnetic tapes at CRREL. Only a few representative graphs and summary tables of the test results are presented here. Tables 2 and 3 summarize the creep test results for saturated and partially saturated samples, respectively. The constant-strain-rate test results for saturated and partially saturated samples are shown in Tables 4 and 5. The detailed physical data for each specimen can be found in Appendix B. Some unspecified quantities in these tables are defined as follows.

Definition of strain and stress

Before discussing the test results, it is appropriate to define stress and strain. True (or natural) axial strain and true axial stress are used in this investigation. They are defined as follows:

$$\text{True strain } \epsilon = -\ln \frac{\text{final length}}{\text{initial length}} = \ln\left(\frac{1}{1-\epsilon_c}\right) \tag{1}$$

where ϵ_c is the conventional (or engineering) strain, which equals $\Delta L/L_0$, where ΔL and L_0 are the axial deformation and the initial length of specimens, respectively.

$$\text{True stress } \sigma = \frac{\text{axial load}}{\text{instantaneous cross-sectional area}} = \frac{P}{A} . \tag{2}$$

If the volume did not change during testing and the samples maintained the shape of right

Table 2. Summary of creep test results for saturated samples.

Specimen no.	Applied stress σ (kg/cm²)	Minimum creep rate $\dot{\epsilon}_m$ (s^{-1})	Time to failure t_m (min)	Failure strain ϵ_f
		Medium density		
		θ = -0.5°C		
6-95	2.7	3.90×10^{-4}	14,000	0.113
6-93*	3.0	3.47×10^{-7}	4,623	0.152
9-148	3.0	6.11×10^{-7}	329	0.017
6-98*	3.5	1.46×10^{-6}	1,504	0.173
6-89	4.0	4.99×10^{-6}	111	0.037
6-88	6.0	3.43×10^{-5}	20.3	0.049
7-87	10.0	3.50×10^{-4}	3.17	0.077
6-86	12.0	1.58×10^{-3}	0.88	0.095
		θ = -1.0°C		
2-18	4.5	2.50×10^{-4}	27,300	0.082
6-94*	5.0	3.03×10^{-7}	8,429	0.181
9-146	5.0	6.36×10^{-7}	1,384	0.062
2-20	5.8	2.04×10^{-6}	1,013	0.161
6-92	6.0	2.31×10^{-6}	637	0.107
9-147	6.0	2.24×10^{-6}	111	0.021
6-91	7.0	9.84×10^{-6}	70	0.051
4-69	7.0	9.50×10^{-6}	66.4	0.044
1-13	9.7	6.30×10^{-5}	15.7	0.068
1-15	9.7	6.19×10^{-5}	14.5	0.063
1-14	14.2	4.74×10^{-4}	3.67	0.112
1-12	18.9	1.57×10^{-3}	1.08	0.110
6-90	20.0	1.27×10^{-3}	0.92	0.083
		θ = -2.0°C		
2-26	7.6	1.80×10^{-4}	29,580	0.087
6-97	7.9	4.50×10^{-4}	15,470	0.090
4-70	8.5	8.00×10^{-7}	1,156	0.069
2-23	9.5	4.28×10^{-6}	384	0.112
6-96	11.0	1.04×10^{-5}	115	0.090
2-25	14.4	6.27×10^{-5}	23.8	0.108
2-24	18.9	2.48×10^{-4}	6.17	0.109
3-62	20.0	2.97×10^{-4}	4.25	0.088
4-75	24.8	8.17×10^{-4}	1.67	0.091
		θ = -3.0°C		
9-140	11.0	3.90×10^{-4}	5,800	0.038
6-100	11.5	2.97×10^{-7}	1,733	0.059
4-80	12.0	1.29×10^{-6}	636	0.075
4-83	12.0	1.13×10^{-6}	573	0.061
6-99	13.0	2.24×10^{-6}	243	0.048
4-77	15.0	1.65×10^{-5}	51.5	0.070
4-72	20.0	1.11×10^{-4}	11.8	0.094
4-81	20.0	1.18×10^{-4}	11.0	0.097
4-71	25.0	3.26×10^{-4}	4.5	0.015
4-73	30.0	8.01×10^{-4}	1.83	0.104
		θ = -5.0°C		
7-110	17.0	1.50×10^{-7}	3,864	0.094
1-8	18.0	8.54×10^{-7}	1,064	0.093
1-7	19.1	1.10×10^{-6}	680	0.101
7-102	20.0	7.35×10^{-6}	180	0.092
10-155	20.0	8.48×10^{-6}	108	0.070
7-105	22.0	1.81×10^{-5}	63.7	0.090
1-10	23.6	3.67×10^{-5}	36.0	0.107
1-9	24.4	3.82×10^{-5}	36.5	0.102
1-2	28.6	1.32×10^{-4}	11.8	0.109
1-4	28.6	1.34×10^{-4}	10.7	0.097
1-3	28.6	1.40×10^{-4}	11.8	0.120
7-103	30.0	1.32×10^{-4}	9.83	0.099
1-6	37.7	6.27×10^{-4}	2.42	0.098
1-5	38.2	7.34×10^{-4}	2.0	0.091
6-101	40.0	6.20×10^{-4}	2.0	0.089
		θ = -7.0°C		
7-11	22.0	3.30×10^{-4}	14,860	0.074
7-112	23.7	8.62×10^{-7}	1,294	0.097
7-106	25.0	2.11×10^{-6}	454	0.083
7-109	25.0	2.16×10^{-6}	479	0.087
7-107	30.0	2.20×10^{-5}	58	0.094
11-171†	35.0	8.03×10^{-5}	11.2	0.057
7-104	40.0	2.08×10^{-4}	6.5	0.100
11-172†	40.0	2.60×10^{-4}	3.5	0.060
		θ = -10.0°C		
7-114	32.0	4.06×10^{-7}	1,584	0.070
7-113	35.0	2.44×10^{-6}	471	0.103
7-115	37.0	5.04×10^{-6}	224	0.105
7-116	40.0	1.59×10^{-5}	52.7	0.071
11-175†	50.0	2.22×10^{-4}	5.20	0.078
11-179†	60.0	3.60×10^{-4}	1.70	0.047
11-180†	60.0	5.14×10^{-4}	1.73	0.054
		Low density		
		θ = -0.5°C		
10-154	3.5	1.48×10^{-6}	80	0.010
		θ = -2.0°C		
10-168	7.0	9.00×10^{-6}	974	0.0090
10-164	7.5	1.11×10^{-7}	453	0.0069
10-161	8.0	2.67×10^{-7}	340	0.0088
10-158	8.5	1.10×10^{-6}	168	0.0160
10-163	11.0	2.98×10^{-6}	80	0.0206
10-160	15.0	1.80×10^{-5}	3.33	0.0061
10-157	16.5	4.70×10^{-5}	2.58	0.0108
10-159	20.0	1.44×10^{-4}	0.75	0.0093
		High density		
		θ = -2.0°C		
12-202	10.0	4.98×10^{-6}	22,940	0.0863
12-197	11.0	5.00×10^{-6}	8,478	0.1030
12-200	12.0	2.19×10^{-6}	460	0.161
12-196	13.0	7.94×10^{-6}	207	0.171
12-195	15.0	1.82×10^{-5}	93	0.168
12-186	20.0	2.69×10^{-4}	8.33	0.189
12-199	25.0	7.30×10^{-4}	3.25	0.191

* Failure did not occur during test. Values shown for "Time to failure" and "Failure strain" are for the time and strain when the test was terminated.

† Tested on a servo-controlled MTS machine.

Table 3. Summary of creep test results for partially saturated samples with medium density.

Specimen no.	Saturation degree s_i (%)	Temperature θ (°C)	Applied stress σ (kg/cm²)	Minimum creep rate $\dot{\epsilon}_m$ (s^{-1})	Time to failure t_m (min)	Failure strain ϵ_f
5-85	95.7	-0.5	4.0	6.08×10^{-6}	103	0.045
5-82	95.3	-0.5	6.0	1.94×10^{-5}	22.6	0.034
5-84	95.2	-0.5	10.0	4.74×10^{-4}	2.17	0.078
5-65	95.5	-1.0	8.0	7.31×10^{-6}	48.3	0.027
5-66	95.3	-1.0	9.5	8.42×10^{-5}	15.1	0.090
5-64	95.9	-1.0	15.0	4.69×10^{-4}	3.0	0.097
5-63	95.5	-1.0	20.0	1.61×10^{-3}	0.83	0.091
5-68	96.2	-2.0	8.5	7.72×10^{-7}	598	0.043
5-78	96.3	-2.0	10.0	5.24×10^{-6}	74.0	0.034
5-79	95.7	-2.0	15.0	9.86×10^{-5}	8.70	0.063
5-67	96.1	-2.0	20.0	4.10×10^{-4}	3.17	0.091

Table 4. Summary of constant-strain-rate compression test results for saturated samples.

Specimen no.	Average strain rate* $\dot{\epsilon}$ (s^{-1})	Peak strength σ_m (kg/cm²)	Strain at σ_m ϵ_f	Time to failure t_m (min)	Initial yield strength σ_y (kg/cm²)	Strain at σ_y ϵ_y	Initial tangent modulus E_i (kg/cm²)	50% strength modulus E_1 (kg/cm²)
			Medium density					
			θ = -0.5°C					
14-215†	6.20×10^{-2}	41.0	0.0614	0.017	—	—	—	—
14-216†	6.20×10^{-2}	38.2	0.0612	0.017	—	—	—	—
9-149	5.85×10^{-3}	21.0	0.0928	0.28	15.4	0.0058	3360	3360
9-151	1.06×10^{-3}	14.7	0.0646	1.02	13.1	0.0059	2661	2550
9-152	1.14×10^{-3}	13.1	0.0764	1.12	11.1	0.0058	—	2690
10-153	1.00×10^{-4}	7.2	0.0093	1.55	6.4	0.0036	4017	2101
11-184	9.23×10^{-6}	4.1	0.0144	26.0	3.2	0.0021	3130	2005
			θ = -1.0°C					
14-213†	6.40×10^{-2}	49.8	0.0774	0.020	—	—	—	—
14-214†	6.20×10^{-2}	58.0	0.0615	0.017	—	—	—	—
9-150	5.73×10^{-3}	28.6	0.0757	0.22	20.7	0.0033	3900	3900
2-21	1.10×10^{-3}	21.1	0.1150	1.75	12.8	0.0046	4710	2776
2-31	1.12×10^{-3}	18.3	0.1399	2.08	—	—	3420	2790
2-32	1.10×10^{-3}	18.4	0.1377	2.08	12.5	0.0044	4250	2500
2-29	1.12×10^{-4}	9.9	0.1140	17.0	8.3	0.0037	7500	3570
2-30	1.11×10^{-4}	10.2	0.1261	19.0	8.4	0.0041	4000	2800
2-33	1.00×10^{-3}	5.4	0.0219	38.0	4.4	0.0027	3978	1786
2-28	1.06×10^{-3}	6.1	0.0323	51.0	4.7	0.0028	2152	2152
3-59	1.01×10^{-3}	5.9	0.0207	34.0	4.6	0.0026	3978	1591
9-145	1.06×10^{-4}	4.4	0.0185	290	3.4	0.0021	5943	1453
			θ = -2.0°C					
14-208†	6.20×10^{-2}	68.5	0.0457	0.013	—	—	—	—
14-210†	6.20×10^{-2}	72.7	0.0460	0.013	—	—	—	—
14-207†	5.85×10^{-3}	42.3	0.0772	0.22	35.0	0.0060	—	6330
14-211†	5.85×10^{-3}	34.9	0.0770	0.22	27.8	0.0060	—	5100
3-38	1.15×10^{-3}	26.5	0.1088	1.58	20.6	0.0056	5333	4766
4-51	1.07×10^{-3}	24.6	0.0854	1.33	18.4	0.0055	7130	5100

* Computed by $\dot{\epsilon} = \epsilon_t/(t_m\times60)$.

† Tested on an MTS machine.

Table 4 (cont'd). Summary of constant-strain-rate compression test results for saturated samples.

Specimen no.	Average strain rate* $\dot{\epsilon}$ (s^{-1})	Peak strength σ_m (kg/cm^2)	Strain at σ_m ϵ_f	Time to failure t_m (min)	Initial yield strength σ_y (kg/cm^2)	Strain at σ_y ϵ_y	Initial tangent modulus E_i (kg/cm^2)	50% strength modulus E_1 (kg/cm^2)
3-36	1.11×10^{-4}	14.7	0.1271	19.0	10.1	0.0036	5258	2285
3-40	1.14×10^{-4}	15.0	0.1219	20.0	11.3	0.0039	7450	3200
4-50	1.13×10^{-4}	14.9	0.1208	20.0	11.5	0.0039	6135	3200
2-34	1.12×10^{-5}	9.7	0.0768	114	5.7	0.0026	3635	2737
3-42	1.11×10^{-5}	10.3	0.0898	135	7.6	0.0031	5000	2455
3-41	1.11×10^{-6}	8.0	0.0817	1227	5.0	0.0024	3200	1650
3-49	1.03×10^{-6}	7.3	0.0383	619	4.3	0.0023	2800	1520
				θ = -3.0°C				
14-219†	6.10×10^{-2}	93.3	0.0301	0.008	—	—	—	—
14-220†	6.10×10^{-2}	89.9	0.0271	0.008	—	—	—	—
9-142	5.63×10^{-3}	48.3	0.0563	0.17	39.1	0.0062	10560	7786
9-143	1.12×10^{-3}	33.7	0.0752	1.12	28.5	0.0052	10300	6073
3-44	1.12×10^{-3}	32.9	0.1066	1.58	23.9	0.0044	6490	4900
3-43	1.13×10^{-4}	19.5	0.1080	16.0	14.8	0.0036	8750	4114
3-47	1.12×10^{-4}	20.0	0.0940	14.0	14.0	0.0037	6250	3509
3-45	1.10×10^{-3}	13.5	0.0759	115	9.6	0.0029	4500	3395
3-46	1.11×10^{-3}	13.4	0.0853	128	10.3	0.0029	11970	3248
3-48	1.03×10^{-6}	11.0	0.0239	387	9.1	0.0031	6875	3458
9-144	1.08×10^{-6}	11.1	0.0240	369	8.9	0.0028	7632	3500
				θ = -5.0°C				
14-217†	6.00×10^{-2}	121.2	0.0149	0.004	—	—	—	—
14-218†	6.00×10^{-2}	122.5	0.0149	0.004	—	—	—	—
9-138	5.62×10^{-3}	58.7	0.0438	0.13	—	—	—	—
8-130	1.11×10^{-3}	37.7	0.0813	1.22	30.5	0.0041	11360	8545
8-131	1.12×10^{-3}	41.8	0.0872	1.30	33.3	0.0041	12000	8840
8-132	1.15×10^{-4}	25.8	0.1245	18.1	19.5	0.0031	14540	5803
8-133	1.06×10^{-5}	19.4	0.0325	51.2	15.1	0.0027	11400	5134
8-134	1.13×10^{-5}	20.1	0.0853	126	15.5	0.0029	10500	4090
8-135	1.07×10^{-6}	17.3	0.0458	711	13.1	0.0029	12280	4518
				θ = -7.0°C				
14-222†	6.00×10^{-2}	138.8	0.0180	0.005	—	—	—	—
14-223†	6.00×10^{-2}	135.8	0.0180	0.005	—	—	—	—
9-139	5.57×10^{-3}	81.2	0.0334	0.10	61.5	0.0050	22390	22390
8-124	1.11×10^{-3}	52.0	0.0851	1.28	40.2	0.0047	14200	9430
8-125	1.11×10^{-3}	52.4	0.0798	1.20	41.9	0.0044	16800	11800
8-126	1.05×10^{-4}	33.9	0.0450	7.13	30.1	0.0039	15410	10590
8-127	1.15×10^{-5}	23.3	0.0925	134	19.2	0.0030	12600	7500
8-128	1.04×10^{-5}	25.2	0.0446	71.3	19.4	0.0030	17000	6070
				θ = -10.0°C				
14-221†	6.00×10^{-2}	176.4	0.0210	0.006	—	—	—	—
11-177†	5.56×10^{-3}	100.3	0.0222	0.07	—	—	—	—
11-178†	5.15×10^{-3}	103.9	0.0206	0.07	82.9	0.0055	—	—
9-137	5.57×10^{-3}	100.1	0.0334	0.10	77.0	0.0047	—	17700
8-120	1.11×10^{-3}	70.2	0.0872	1.31	54.1	0.0044	22600	14500
8-121	1.23×10^{-3}	72.5	0.0971	1.32	58.8	0.0041	21200	12260
7-118	1.15×10^{-4}	49.1	0.1208	17.5	40.1	0.0038	27200	15200
8-119	1.13×10^{-3}	38.8	0.0993	147	30.0	0.0031	26910	12860
8-122	1.12×10^{-3}	38.6	0.0872	130	22.2	0.0024	10000	9400
8-123	1.09×10^{-4}	33.1	0.0651	998	17.8	0.0024	9000	6210

* Computed by $\dot{\epsilon} = \epsilon_f/(t_m \times 60)$.
† Tested on an MTS machine.

Table 4 (cont'd). Summary of constant-strain-rate compression test results for saturated samples.

Specimen no.	Average strain rate* $\dot{\epsilon}$ (s^{-1})	Peak strength σ_m (kg/cm^2)	Strain at σ_m ϵ_f	Time to failure t_m (min)	Initial yield strength σ_y (kg/cm^2)	Strain at σ_y ϵ_y	Initial tangent modulus E_i (kg/cm^2)	50% strength modulus E_1 (kg/cm^2)
				Low density				
				$\theta = -2.0°C$				
11-185	5.85×10^{-3}	41.5	0.0246	0.07	36.7	0.0057	—	6600
10-165	5.58×10^{-3}	37.5	0.0106	0.04	32.0	0.0050	—	7100
10-166	1.00×10^{-3}	29.2	0.0093	0.16	23.9	0.0041	—	7600
10-167	1.00×10^{-4}	15.8	0.0082	1.50	13.6	0.0026	11700	5030
10-169	1.01×10^{-5}	9.3	0.0146	24.0	7.0	0.0018	21200	3214
10-162	8.1×10^{-7}	8.0	0.0102	210	6.2	0.0019	5350	3125
				High density				
				$\theta = -2.0°C$				
14-203†	6.22×10^{-2}	56.0	0.0933	0.025	—	—	—	—
14-204†	6.09×10^{-2}	50.7	0.1096	0.029	—	—	—	—
14-205†	6.55×10^{-3}	37.7	0.1965	0.50	21.6	0.0060	—	—
12-188	6.14×10^{-3}	39.3	0.1842	0.50	20.7	0.0060	6670	953
12-189	1.24×10^{-3}	25.5	0.2046	2.75	10.5	0.0040	—	—
12-190	1.24×10^{-3}	27.8	0.2146	2.88	13.4	0.0049	3550	980
12-191	1.24×10^{-4}	17.6	0.2243	30.0	8.0	0.0036	5000	732
12-192	1.23×10^{-5}	13.1	0.1863	253	5.4	0.0028	6000	475
12-193	1.22×10^{-5}	12.3	0.1692	231	5.0	0.0028	4750	300
12-194	1.19×10^{-6}	11.6	0.1504	2098	4.7	0.0032	4006	396
12-198	1.18×10^{-6}	11.8	0.1507	2126	5.6	0.0037	5000	438

* Computed by $\dot{\epsilon} = \epsilon_t/(t_m \times 60)$.
† Tested on an MTS machine.

Table 5. Summary of constant-strain-rate compression test results for partially saturated samples with medium density.

Specimen no.	Saturation degree s_i (%)	Temperature θ (°C)	Average strain rate $\dot{\epsilon}$ (s^{-1})	Peak strength σ_m (kg/cm^2)	Strain at σ_m ϵ_f	Time to failure t_m (min)	Initial yield strength σ_y (kg/cm^2)	Strain at σ_y ϵ_y	Initial tangent, modulus E_i (kg/cm^2)	50% strength modulus E_1 (kg/cm^2)
5-57	96.0	-1.0	1.17×10^{-3}	16.4	0.1405	2.0	11.9	0.0055	2900	2320
5-58	95.7	-1.0	1.10×10^{-4}	9.4	0.0715	12.0	7.8	0.0046	3760	2300
5-54	96.0	-2.0	1.11×10^{-3}	20.6	0.1052	1.58	15.7	0.0055	5000	3550
5-56	96.2	-2.0	1.12×10^{-4}	13.8	0.0805	12.0	11.4	0.0037	5400	3000
5-52	96.2	-3.0	1.12×10^{-4}	17.1	0.1011	15.0	13.7	0.0038	7700	4150
5-53	98.1	-3.0	1.00×10^{-6}	9.7	0.0420	738	6.8	0.0020	4930	3600

circular cylinders, the true axial stress can be calculated by

$$\sigma = P(1-\epsilon_c)/A_0 \tag{3}$$

where A_0 is the initial cross-sectional area of samples.

Definition of creep failure

Figure 12, a typical $\log\dot{\epsilon}$ vs $\log t$ curve for a relatively high stress, clearly shows that the axial strain rate $\dot{\epsilon}$ changes with time t and attains a minimum creep rate at a definite time. Fol-

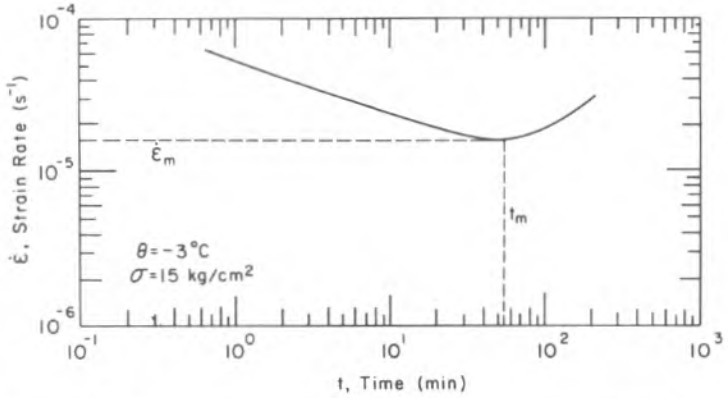

Figure 12. Typical curve of log$\dot{\epsilon}$ vs log$t$ under relatively high stress.

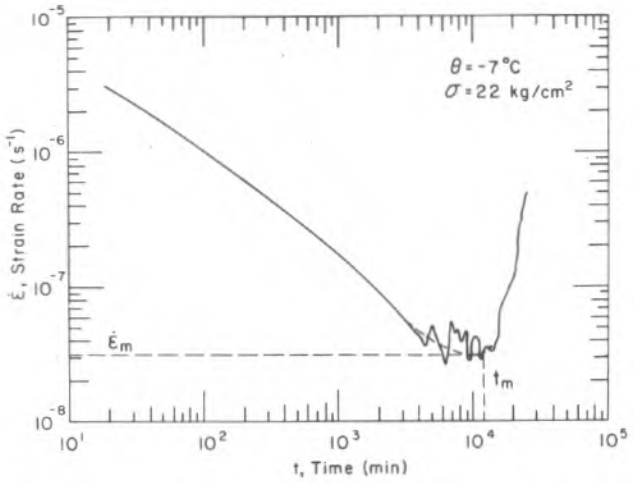

Figure 13. Typical curve of log$\dot{\epsilon}$ vs log$t$ under relatively low stress for medium-density samples.

lowing the definition of creep failure by many researchers (Fish 1979, Assur 1980, Martin et al. 1981, Mellor and Cole 1982), we define creep failure as the point at which the creep rate reaches its minimum value $\dot{\epsilon}_m$. Correspondingly, the time to the minimum is the time to creep failure t_m, and the strain at the minimum is the failure strain ϵ_f. These three quantities—$\dot{\epsilon}_m$, t_m and ϵ_f—are designated as the creep failure parameters.

Because the strain rate curves for the medium-density samples tested at relatively low stress (Fig. 13) fluctuated frequently within the so-called secondary creep stage, it was difficult to identify a minimum strain rate on this type of curve. To determine the minimum strain rate on this type of curve in a consistent manner, we smoothed out the "spikes" in the log$\dot{\epsilon}$ vs log$t$ curves by averaging strain rates over larger time intervals, as shown in Figure 13.

Definition of failure in constant-strain-rate tests

Figure 14 shows a typical set of stress–strain curves for various strain rates at a temperature of -3°C. Each curve has a definite maximum. Failure in uniaxial compression is thus defined as the point at which the true axial stress attains its maximum value σ_m. Similarly, the time to the peak is called the time to failure t_m, and the strain at the peak is the failure strain ϵ_f.

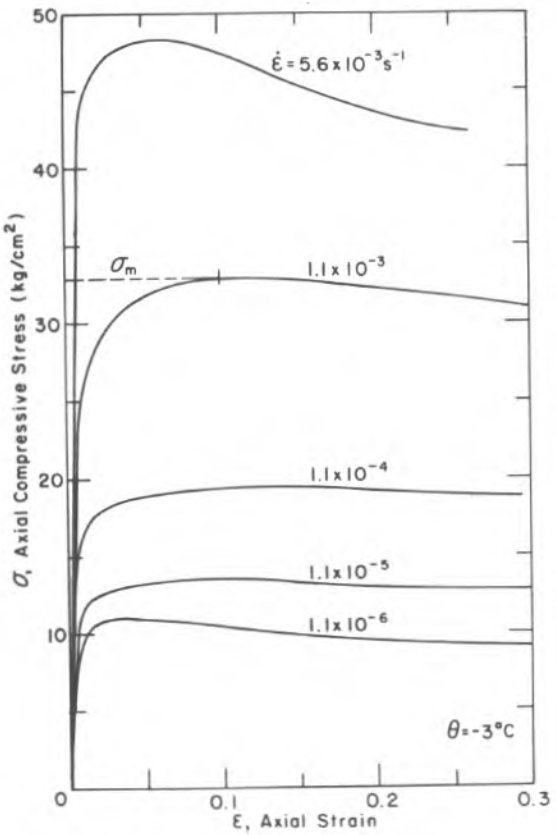

Figure 14. Typical stress-strain curves for specimens with medium density under various $\dot{\epsilon}$ at -3 °C.

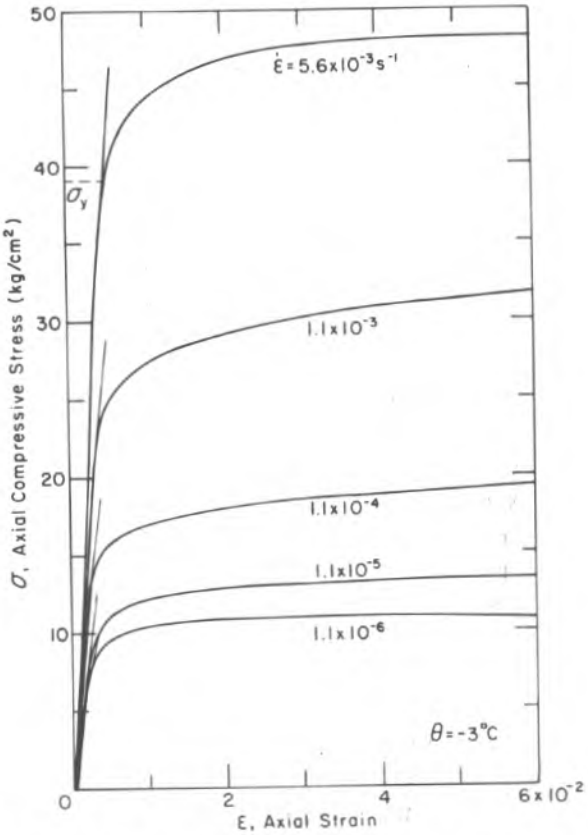

Figure 15. Stress-strain curves shown in Figure 14 expanded for the the initial 6% strain.

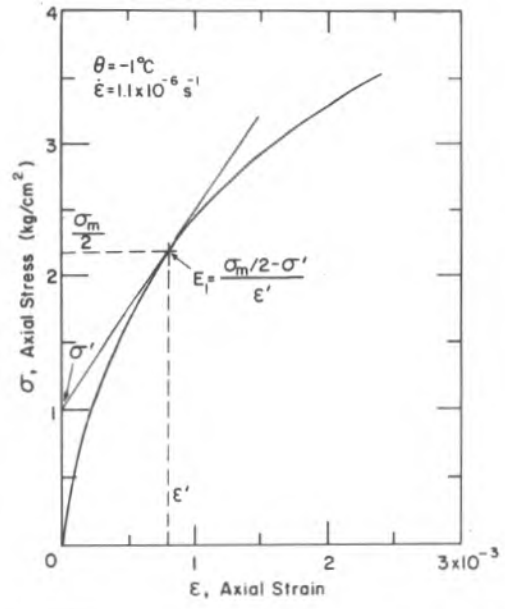

Figure 16. Determination of 50% peak strength modulus.

Definition of initial yield strength

Following Sayles and Carbee (1981), we define the initial yield strength σ_y, as shown in Figure 15, as the stress at which the slope of a stress-strain curve starts to decrease perceptibly from the initial tangent to the curve, which is at the strain where the pore ice would be expected to fracture. The strain at this stress is defined as the initial yield strain ϵ_y. Although the determination of σ_y is not as precise as one would like, meaningful data can still be obtained as long as a consistent procedure is used in determining the yield strength for all expanded stress-strain curves.

Determination of initial tangent modulus and 50% peak strength modulus

It is well known that the determination of the initial tangent modulus of a nonelastic material based on a stress-strain curve is difficult, particularly when the curve is rounded as shown in Figure 16. As far as we know,

there is no standard procedure for determining the initial tangent modulus. The reported values of initial tangent modulus E_i in Tables 4 and 5 are determined graphically from stress–strain curves. The 50% peak strength modulus E_1 is defined as the tangent modulus of a point on a stress–strain curve at which $\sigma = \sigma_m/2$, as is illustrated in Figure 16. These values are also determined graphically.

CREEP BEHAVIOR

General nature of the creep process and the failure mode

The variation of strain rate in the creep process can be illustrated with a log$\dot{\varepsilon}$ vs log$t$ plot. Typical log$\dot{\varepsilon}$ vs log$t$ curves for various test conditions are presented in Figure 17. All of these curves reveal the same general law of the creep process: When a constant stress is applied to a specimen, the creep rate continuously decreases with time (strain hardening dominates), reaches a minimum value (point F in these figures), and then starts to accelerate until fracture or plastic failure occurs (strain softening dominates). That is, there must be an equilibrium (or critical) stress–strain state between these two opposite processes—strain hardening and strain softening. At this moment, samples must be in equilibrium with the external stress. In this sense, it is reasonable to define the minimum point on log$\dot{\varepsilon}$ vs log$t$ curves as the creep failure. The creep rate seldom remains constant within the secondary creep stage. Therefore, the so-called steady-state creep may exist only at one point, at least for the investigating conditions reported here.

Examining all of the log$\dot{\varepsilon}$ vs log$t$ curves for low stresses, we found that there was a large decrease in creep rate at the onset of secondary creep for samples with medium and high densities but not for the low-density samples. This suggests that different deformation mechanisms dominate the creep process of ice-rich low-density samples than for dense frozen silt samples.

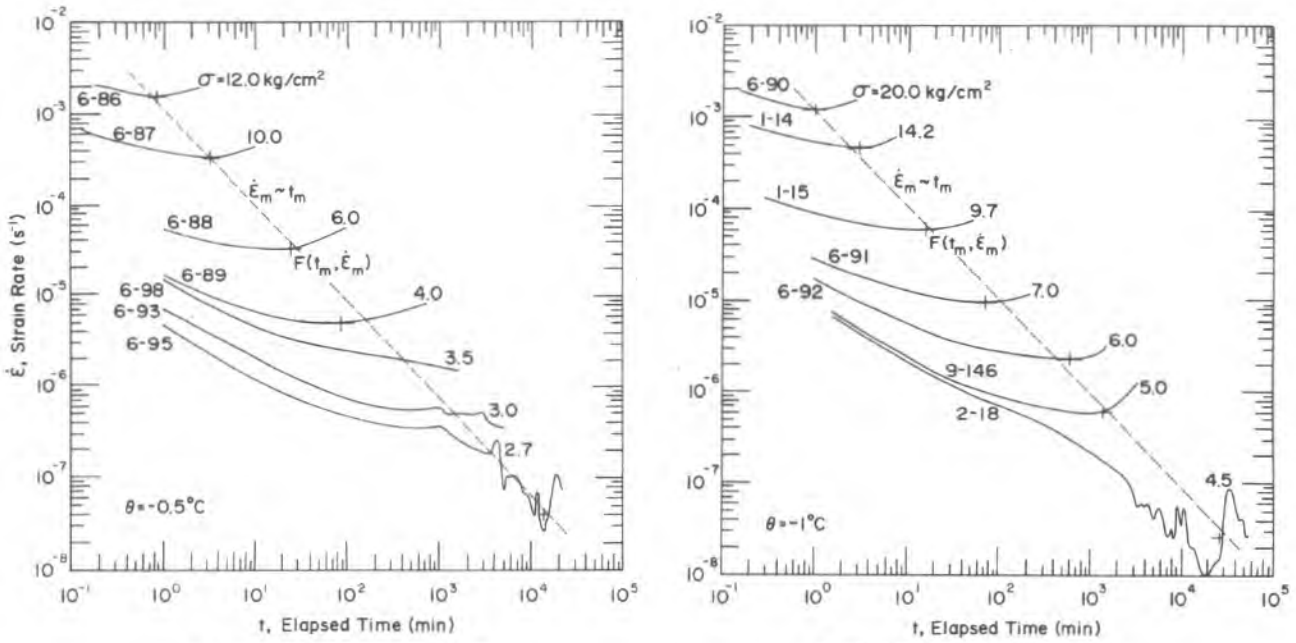

a. Medium density at -0.5 °C.

b. Medium density at -1 °C.

Figure 17. Log$\dot{\varepsilon}$ vs log$t$ curves for different conditions.

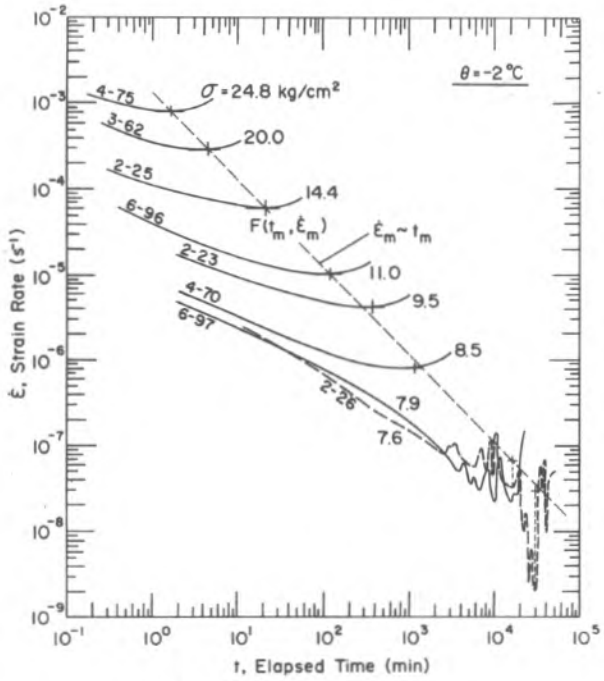

c. Medium density at -2°C.

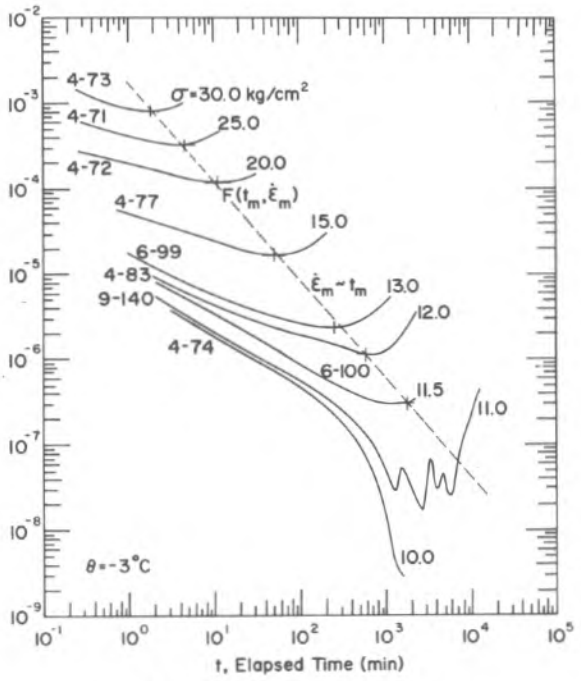

d. Medium density at -3°C.

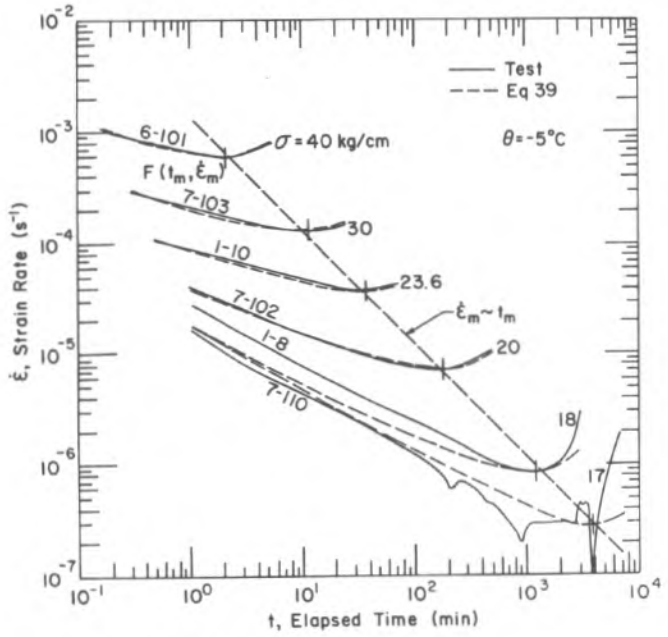

e. Medium density at -5°C.

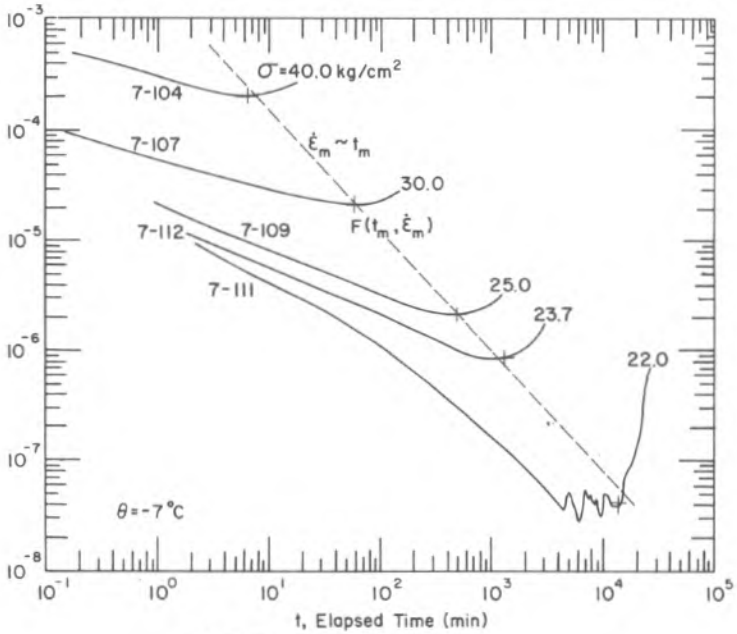

f. Medium density at -7°C.

Figure 17 (cont'd). Log ε̇ vs log t curves for different conditions.

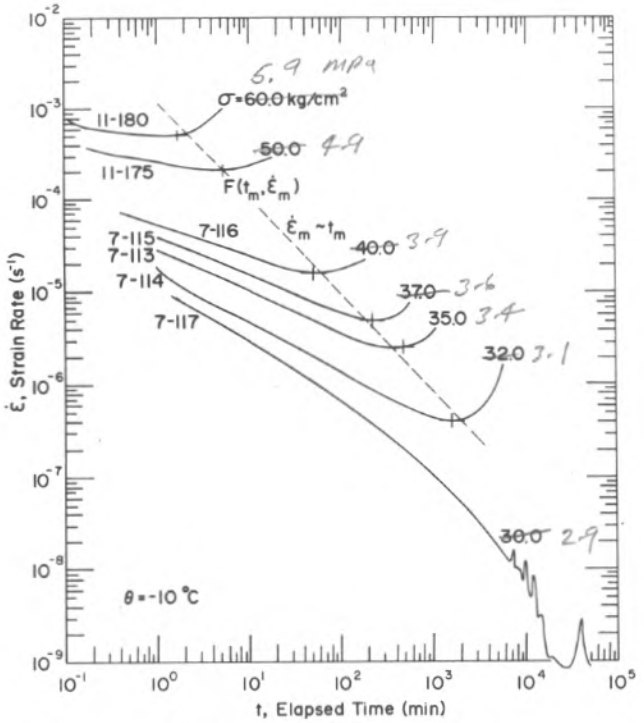

g. Medium density at -10°C.

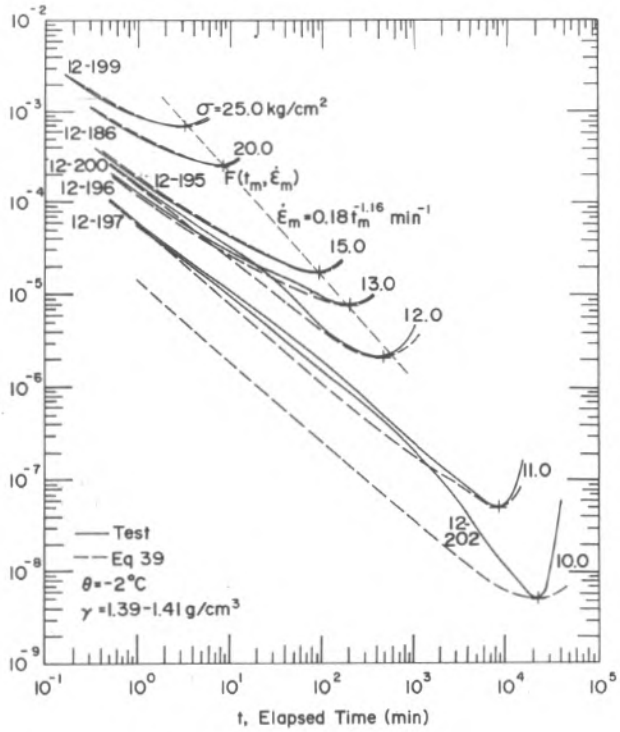

h. High density at -2°C.

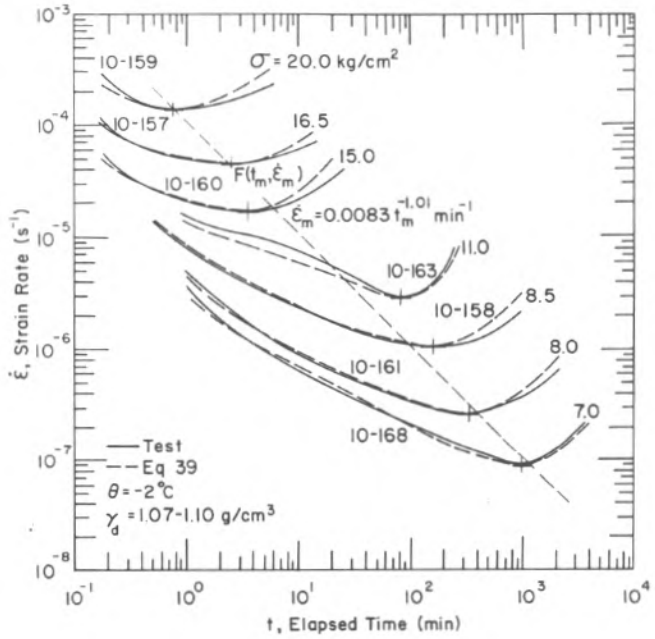

i. Low density at -2°C.

Figure 17 (cont'd).

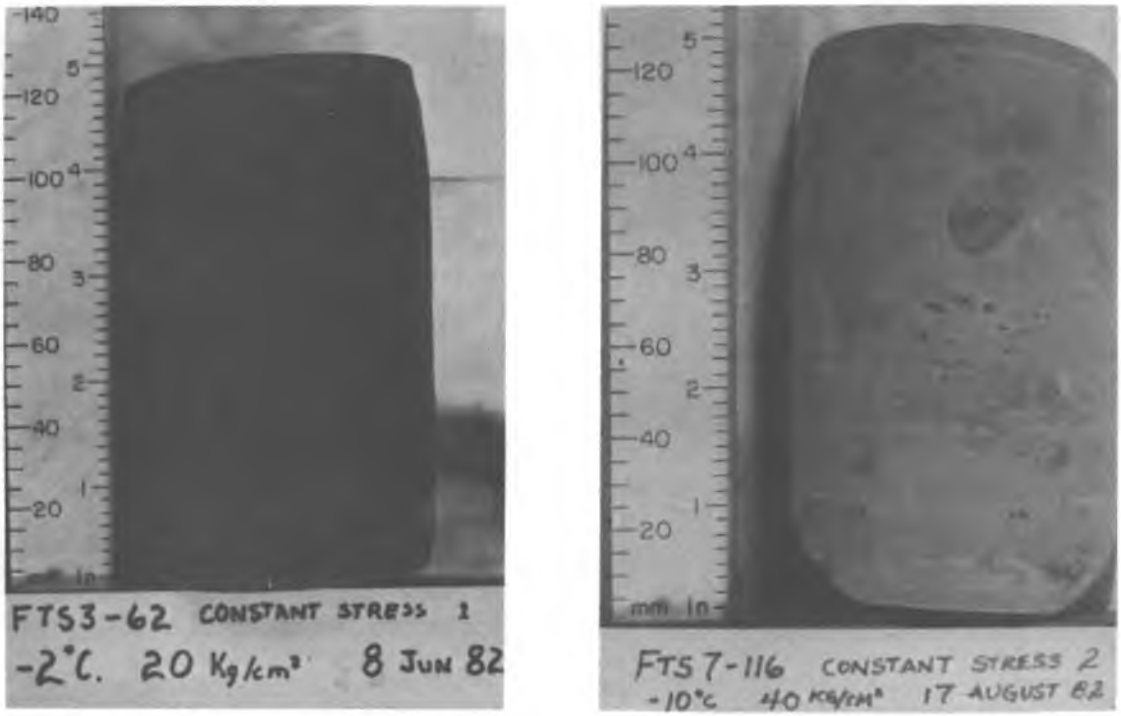

a. $\theta = -2°C$, $\sigma = 20$ kg/cm². *b.* $\theta = -10°C$, $\sigma = 40$ kg/cm².

Figure 18. Typical Fairbanks silt specimens after short-term creep tests.

Another observation was the occurrence of spikes in the $\log\dot{\varepsilon}$ vs $\log t$ curves within the secondary creep stage for medium-density samples tested at low stresses (Fig. 17a–g). The spikes occurred over a time of a few days to more than one month even though the stresses and temperatures were constant. The spikes did not occur for both high- and low-density tests for the same orders of strain rate (Fig. 17h, i). This evidence indicates that the spikes are not artifacts of the test apparatus but are sample responses. The same phenomena (both the drop of the creep rate and the occurrence of spikes in secondary creep) have been observed on a frozen sand (Martin et al. 1981).

The constant-stress creep tests showed that all specimens failed plastically under the ranges of stress and temperature employed. No brittle failures were observed. However, in examining the failed specimens, we found that different failure features could be distinguished, even though they all appeared to fail plastically. For example, for the short-term creep test (less than 1 day to failure) all test specimens failed plastically without visible cracks, even for strains greater than 25% and low temperatures (Fig. 18). However, for the long-term creep tests (greater than about 1 day to failure), after large plastic strains, ×-shaped shearing cracks were visible on the sample surface as shown in Figure 19, especially for dense frozen silt. The same phenomenon was observed by Vialov (1962) for a frozen dense clayey soil. We call this plastic failure with cracks.

Minimum creep rate

In the following section, we will concentrate on the quantitative evaluation of the minimum creep rate $\dot{\varepsilon}_m$ and time to creep failure t_m as a function of stress and temperature, since they are the basic parameters chosen in this study for predicting creep deformation and long-term strength of frozen soils. We found from this study that the minimum creep rate strongly depends upon applied stress, temperature and dry density of the soil.

a. $\theta = -2°C$, $\sigma = 10$ kg/cm².

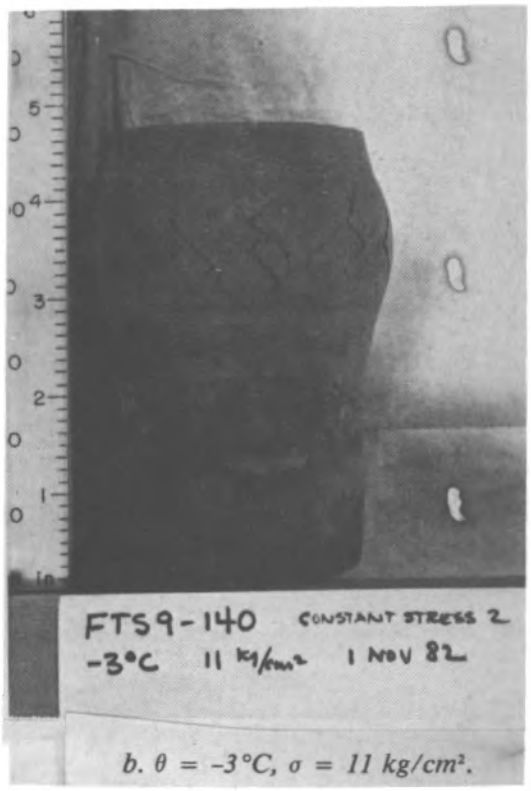

b. $\theta = -3°C$, $\sigma = 11$ kg/cm².

c. $\theta = -5°C$, $\sigma = 17$ kg/cm².

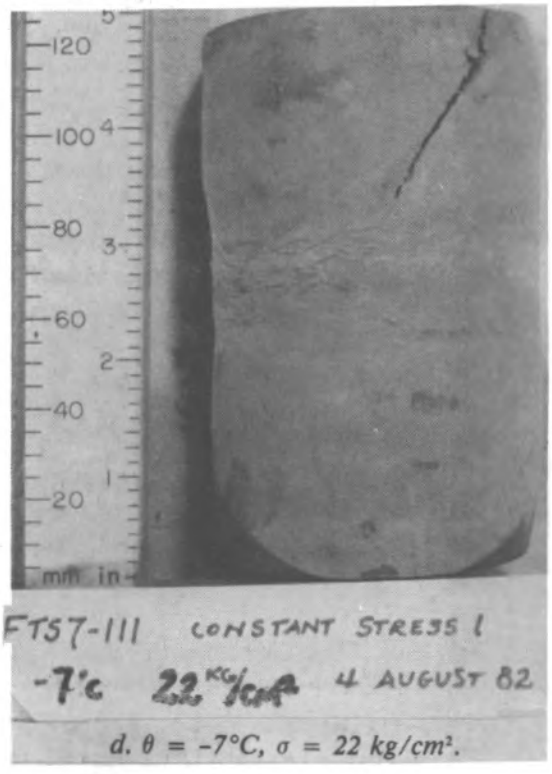

d. $\theta = -7°C$, $\sigma = 22$ kg/cm².

Figure 19. Typical Fairbanks silt specimens after long-term creep tests, showing ×-shaped shear cracks.

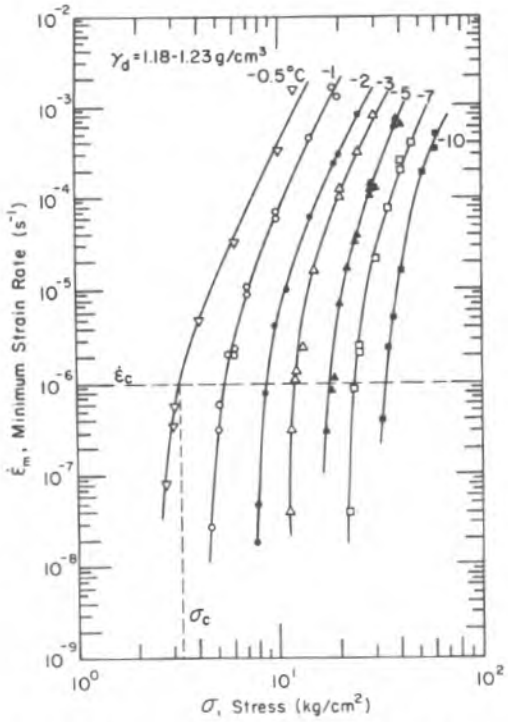

Figure 20. Log-log plot of $\dot{\varepsilon}_m$ vs σ for various temperatures.

Stress dependence

The minimum creep rate $\dot{\varepsilon}_m$ as a function of stress σ at various test temperatures for medium dry density is plotted in Figure 20 on a log–log scale. The curves in this figure are not straight lines, but they can be considered a set of quasi-parallel curves. The slopes of these curves perceptibly increase at a certain minimum strain rate as stresses decrease. This can be seen more clearly in plots of $\log\dot{\varepsilon}_m$ vs $1/\sigma$ (Fig. 21). This figure shows a family of bilinear curves that all deflect at about the same minimum strain rate (10^{-6} s^{-1}). For convenience in describing these data, we define a critical creep rate $\dot{\varepsilon}_c$ that can be considered the minimum strain rate for distinguishing between two types of creep of frozen soil: short-term creep, which has a minimum creep rate greater than $\dot{\varepsilon}_c$, and long-term creep, which has a minimum creep rate less than $\dot{\varepsilon}_c$. The stresses corresponding to $\dot{\varepsilon}_c$ for various temperatures are defined as the critical creep stresses. Moreover, these two types of creep are governed by different deformation mechanisms, which will be discussed later. In addition, Figure 21 shows that at high strain rates all of the curves converge at a common point. Thus, the constitutive equations for the frozen silt with medium density can be described by the following exponential equations.

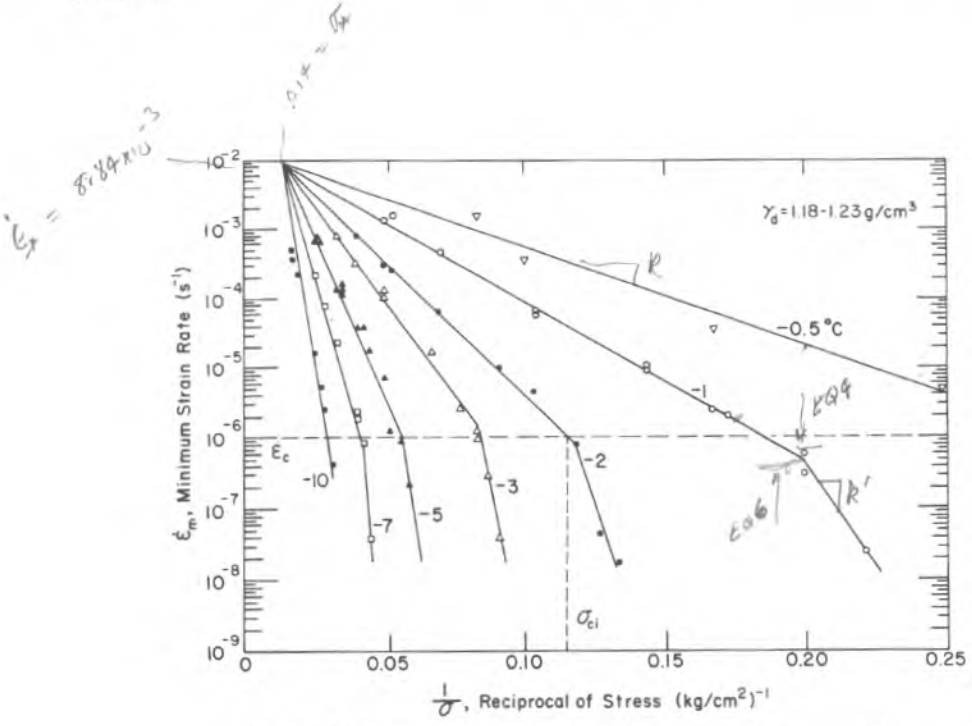

Figure 21. Log $\dot{\varepsilon}_m$ vs $1/\sigma$ curves for various temperatures.

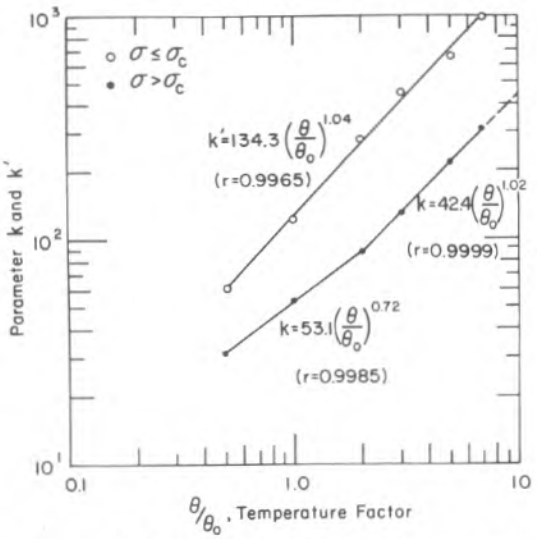

Figure 22. Parameters k *and* k′ *as a function of temperature.*

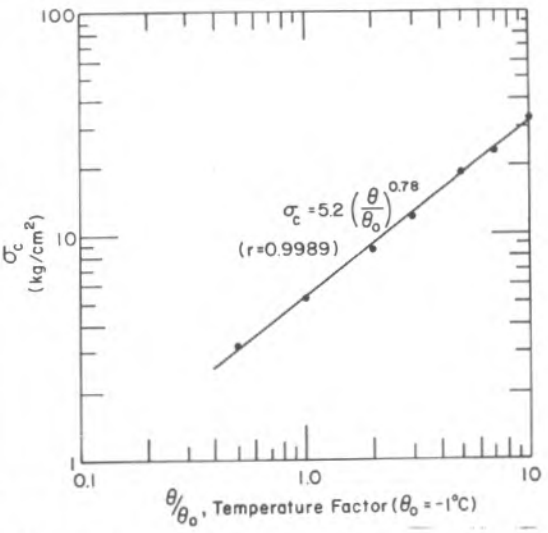

Figure 23. Critical creep strength σ_c as a function of temperature.

For short-term creep ($\sigma > \sigma_c$),

$$\dot{\varepsilon}_m = \dot{\varepsilon}_* \exp\left[-k\left(\frac{1}{\sigma} - \frac{1}{\sigma_*}\right)\right] \tag{4}$$

where $\dot{\varepsilon}_*$ and σ_* are reference values independent of temperature and are used for convenience in presenting this data. By linear regression analysis, we obtained $\dot{\varepsilon}_* = 8.84 \times 10^{-3}\ s^{-1}$ and $\sigma_* = 71.4\ kg/cm^2$ for the tested silt with dry density r_d ranging from 1.18 to 1.23 g/cm³. The parameter k is plotted as a function of temperature in Figure 22 and can be determined by

Table 6. Values of σ_c in eq 6.

θ (°C)	σ_c (kg/cm²)	θ (°C)	σ_c (kg/cm²)
-0.5	3.2	-5	18.4
-1	5.2	-7	23.5
-2	8.5	-10	32.5
-3	11.7		

$$k = 53.1(\theta/\theta_0)^{0.72} \qquad \text{for } -0.5° \ge \theta \ge -2℃$$

and (5)

$$k = 42.4(\theta/\theta_0)^{1.02} \qquad \text{for } -2° \ge \theta \ge -7℃$$

where θ is the test temperature in ℃, and θ_0 is a reference temperature taken as -1℃.

For long-term creep ($\sigma \le \sigma_c$),

$$\dot{\varepsilon}_m = \dot{\varepsilon}_c \exp\left[-k'\left(\frac{1}{\sigma} - \frac{1}{\sigma_c}\right)\right] \tag{6}$$

where $\dot{\varepsilon}_c$ is the critical creep rate, equal to $10^{-6}\ s^{-1}$, and σ_c is the critical creep strength defined above. The variation of σ_c with temperature is illustrated in Table 6 and Figure 23 and can be expressed as

$$\sigma_c = 5.2(\theta/\theta_0)^{0.78} \tag{7}$$

where σ_c is in kg/cm².

The parameter k' in eq 6 as a function of temperature is also plotted in Figure 22 and can be determined by

$$k' = 134(\theta/\theta_0)^{1.04}. \tag{8}$$

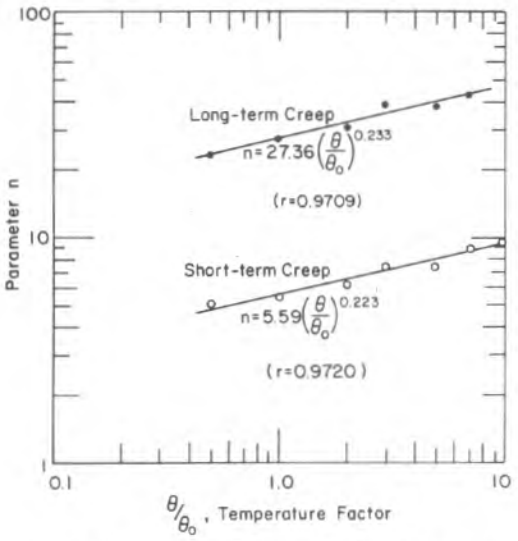

Figure 24. Power n *as a function of temperature.*

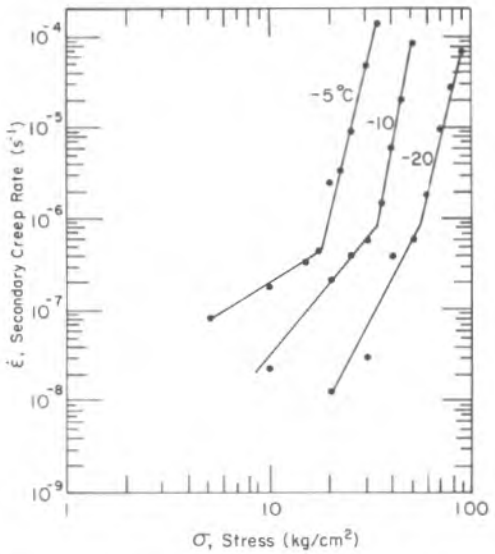

Figure 25. Plot of log$\dot{\varepsilon}$ vs logσ for Callovian silty sandy loam. (After Vialov 1962, Table 7.)

The log$\dot{\varepsilon}_m$ vs logσ curves in Figure 20 can also be represented approximately as a set of bilinear curves, which deflect at the strain rate $\dot{\varepsilon}_c$ of 10^{-6} s^{-1}. Thus, assuming straight lines, the stress dependence of $\dot{\varepsilon}_m$ for medium density can be also expressed by a power equation:

$$\dot{\varepsilon}_m = \dot{\varepsilon}_c(\sigma/\sigma_c)^n \tag{9}$$

where the exponent n depends upon temperature. Its variation with temperature for both long-term and short-term creep is shown in Figure 24 and can be evaluated by

$$n = 5.59(\theta/\theta_0)^{0.223} \tag{10}$$

for short-term creep and

$$n = 27.36(\theta/\theta_0)^{0.233} \tag{11}$$

for long-term creep.

A similar power function was reported by Ladanyi (1972) to evaluate secondary creep rates as a function of stress, based on work in metals by Hult (1966). However, the parameter σ_c referred to a proof stress in his equation is not defined as discussed here.

Vialov (1962) also observed a consistent deflection on log$\dot{\varepsilon}$ vs logσ curves at a strain rate of near 10^{-6} s^{-1} for a comparable soil (Fig. 25). In addition, the slope of the log$\dot{\varepsilon}$ vs logσ curves for short-term creep from Vialov's data is also very close to that from our results. However, there is a substantial difference between the results for long-term creep; the slope is much greater for our data than for Vialov's.

Temperature dependence

In recent years, attempts have been made to apply the rate process theory (RPT) to the creep of frozen soil (Akili 1966, 1970, Andersland and Akili 1967, Goughnour 1967, Andersland and Douglas 1970, Vialov 1973, Mitchell 1976, Fish 1980, Martin et al. 1981, Ting 1981). The different individuals have presented various formulas relating creep rate to tem-

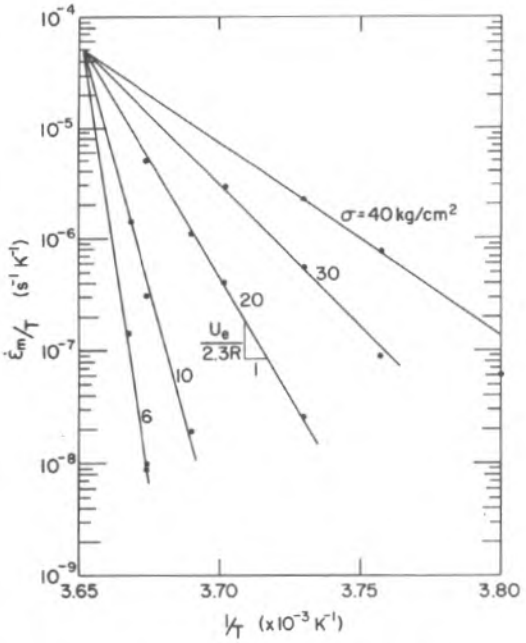

Figure 26. Plot of log($\dot{\varepsilon}_m$/T) vs 1/T.

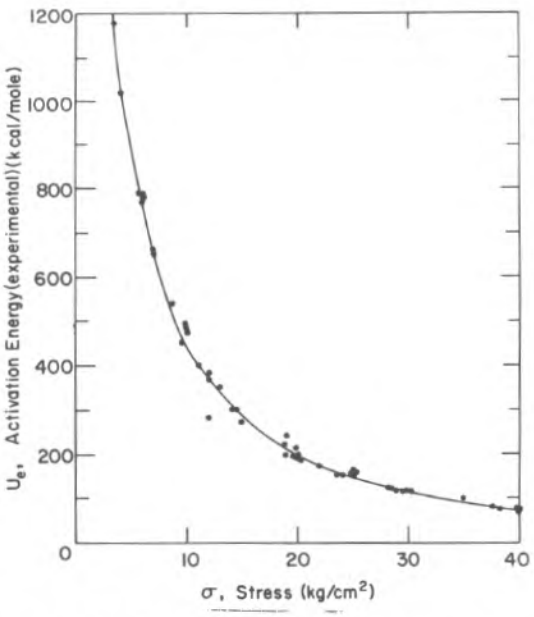

Figure 27. Experimental activation energy U_e as a function of stress.

perature and stress based on RPT. To evaluate the applicability of this theory to our test results, the short-term creep test data for medium density were plotted in the log ($\dot{\varepsilon}_m/T$) vs $1/T$ plane as shown in Figure 26. As expected, all of the isostress curves are straight lines within a temperature range of -0.5° to -7°C. All these isostress curves appear to converge at a common point. Thus, we can present a modified RPT expression for frozen silt as follows:

$$\dot{\varepsilon}_m = \frac{XKT}{h} \exp\left[-\frac{U_e}{R}\left(\frac{1}{T} - \frac{1}{T_0}\right)\right] \tag{12}$$

or

$$\dot{\varepsilon}_m = A_1 T \exp\left[-\frac{U_e}{R}\left(\frac{1}{T} - \frac{1}{T_0}\right)\right] \tag{13}$$

where X = constant (for frozen silt with medium density, $X = 2.4\times10^{-15}$)
K = Boltzman's constant (1.38×10^{-23} J/K)
T = absolute temperature (K)
h = Planck's constant (6.624×10^{-34} Js)
U_e = activation energy (kcal/mole)
R = gas constant (1.987×10^{-3} kcal/mole K)
T_0 = characteristic temperature (for frozen silt with medium density, $T_0 = 273.15$ K)
$A_1 = XK/h$ = constant (for frozen silt with medium density, $A_1 = 5.0\times10^{-5}$ s^{-1} K^{-1}).

To calculate U_e, rearranging eq 13, we have

$$U_e = -2.3R\left(B + \log\frac{\dot{\varepsilon}_m}{T}\right)\Big/\left(\frac{1}{T} - \frac{1}{T_0}\right) \tag{14}$$

where $B = -\log A_1 = 4.3$.

The U_e values calculated from the creep test data as a function of stress are shown in Figure 27; there is a close relationship between activation energy and stress. The activation

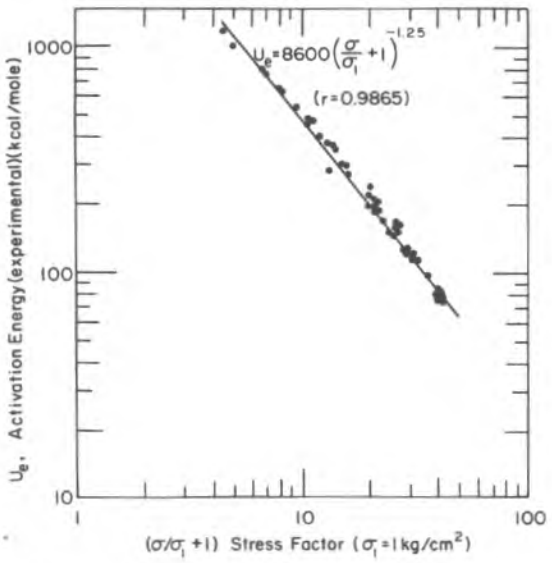

Figure 28. Plot of log U_e *vs log*$(\sigma/\sigma_1 + 1)$.

energy, then, is a useful characteristic by which creep test data can be normalized. Explicitly, U_e strongly depends on stress, especially at the lower stress range tested in this study. Therefore, the values of U_e without specifying stress have no significance. The explicit nonlinearity between U_e and σ indicates that the relation $U_e = \Delta F - \beta\sigma$, which was derived based on an approximation of RPT (i.e. the energy supplied by the action of external stress is greater than the thermal energy) and experimentally verified for a limited range of values by a number of investigators (e.g. Mitchell et al. 1968, Ting 1981), is not valid over a wide range of stresses discussed. The reason for the discrepancy may be that this approximation is not true for low stress or that more than one mechanism could be operating simultaneously in the creep process at low stress levels.

By replotting Figure 27 for the coordinates of $\log U_e$ vs $\log(\sigma/\sigma_1 + 1)$ as shown in Figure 28, we found that experimental energy U_e as a function of stress σ can be well described by

$$U_e = \Delta F(\sigma/\sigma_1 + 1)^{-\delta} \tag{15}$$

where σ_1 = reference stress, taken as 1 kg/cm^2
δ = constant, equal to 1.25
ΔF = free energy, defined in this study as the apparent minimum energy required to overcome the energy barrier when the external stress is zero.

For the frozen silt tested, ΔF was found to be as high as 8600 kcal/mole, which is almost two orders of magnitude greater than the free energy of activation reported by some investigators (Andersland and Douglas 1970, Martin et al. 1981).

Following a modified RPT equation for ice, which includes a power function to describe the stress dependence (Glen 1955, Gold 1973, Langdon 1973, Weertman 1973, Homer and Glen 1978), we wrote another modified RPT equation:

$$\dot{\epsilon}_m = \frac{X'KT}{h}\left(\frac{\sigma}{\sigma_*}\right)^n \exp\left(-\frac{U_a}{RT}\right) \tag{16}$$

where X' = dimensionless constant
σ_* = reference stress
n = exponent of σ/σ_c, defined in eq 9
U_a = apparent activation energy.

To determine U_a and X', eq 16 is rearranged as

$$\log \frac{\dot{\epsilon}_m}{T(\sigma/\sigma_*)^n} = \log \frac{X'K}{h} - \frac{U_a}{2.3R} \cdot \frac{1}{T} \cdot \tag{17}$$

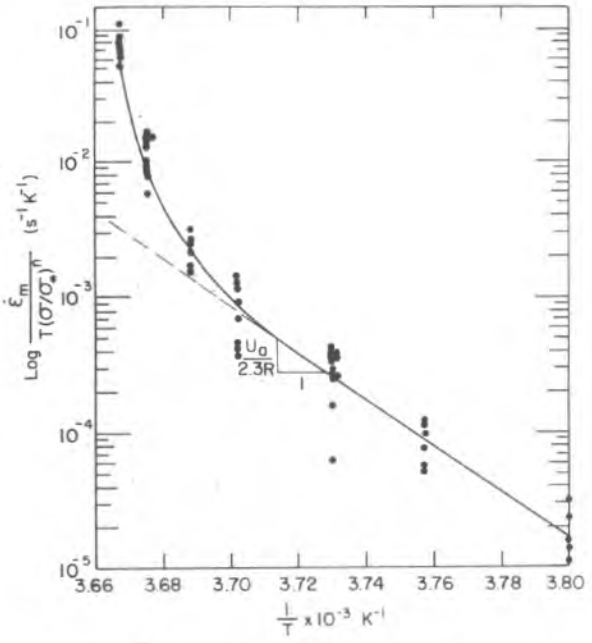

Figure 29. Plot of $\log[\dot{\varepsilon}_m/T(\sigma/\sigma_*)^n]$ vs $1/T$.

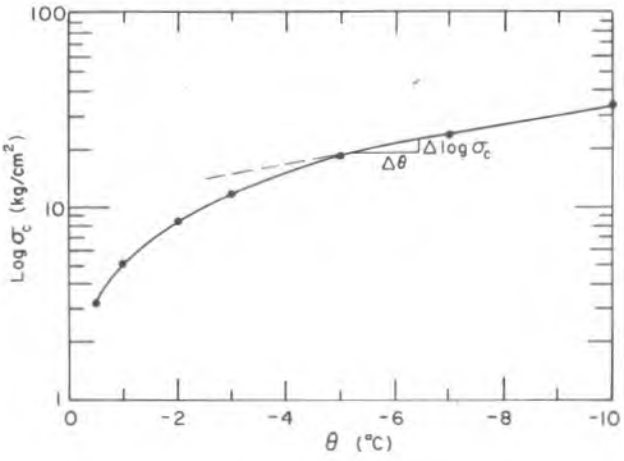

Figure 30. Plot of $\log \sigma_c$ vs temperature.

The creep test data for $\sigma \geq \sigma_c$ was plotted in Figure 29 on the basis of this equation. This plot does not follow a straight line as expected, indicating that there are no identical values of apparent energy U_a and the parameter X' for the entire range of testing temperatures. In other words, both U_a and X' can be approximately considered as constants only within a certain range of temperature. For example, if the curve in Figure 29 approximates a straight line within the temperature range of -3° to -10°C, then $U_a = 81$ kcal/mole and $X' = 3.0 \times 10^{62}$. However, for higher temperatures the curve becomes so steep that it is difficult to calculate the values of U_a and X'. This means that eq 16 does not work for higher temperatures.

Combining his creep law and RPT, Ladanyi (1972) developed a simple way to determine an apparent activation energy:

$$U_a = 2.303 \times 273^2 n R \frac{\Delta \log \sigma_c}{\Delta \theta} \tag{18}$$

where σ_c is the stress corresponding to a given $\dot{\varepsilon}_m$, and θ is temperature (°C). To evaluate U_a with this equation, a plot of $\log \sigma_c$ vs θ was constructed from our test data (Fig. 30). Clearly this plot is nonlinear, illustrating that eq 18 is appropriate for a certain range of lower temperatures but not for high temperatures. The parameter n in eq 18 is also temperature dependent. Taking an average value of $n = 8$, we computed $U_a = 386$ kcal/mole for the tested frozen silt within a temperature range of -5° to -10°C. Unfortunately, we could not compare this computed value with that shown by Ladanyi (1972), because no temperature data are available in his report.

Effect of dry unit weight

The minimum creep rate as a function of dry density for various stress levels at -2°C is illustrated in Figure 31. Obviously, dry density has no significant effect on $\dot{\varepsilon}_m$ for relatively high stresses, but it significantly affects $\dot{\varepsilon}_m$ for lower stresses. For example, $\dot{\varepsilon}_m$ decreases by three orders of magnitude as γ_d increases from 1.07 to 1.40 g/cm³ at a stress level of 10 kg/cm², while it remains almost the same for the same range of γ_d at a stress of 20 kg/cm².

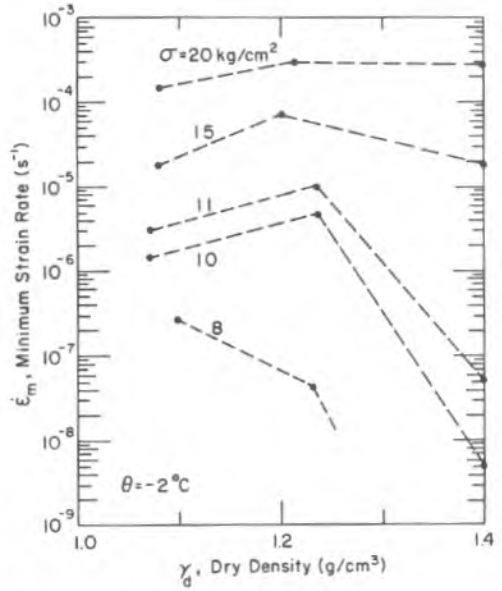

Figure 31. Minimum creep rates as a function of dry density for various stresses at -2 °C.

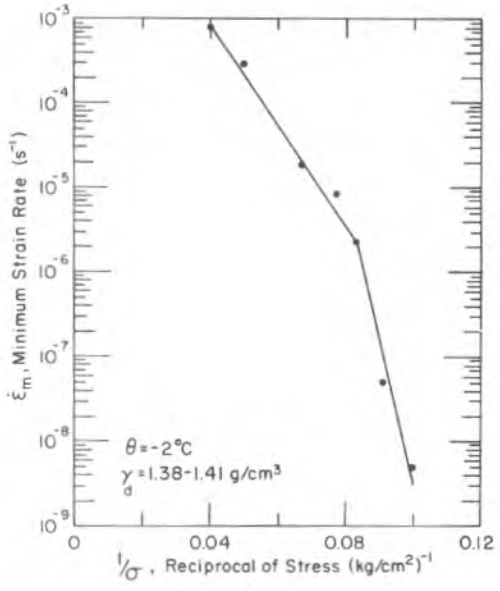

Figure 32. Log$\dot{\varepsilon}_m$ vs 1/σ curves for the specimens with high density at -2 °C.

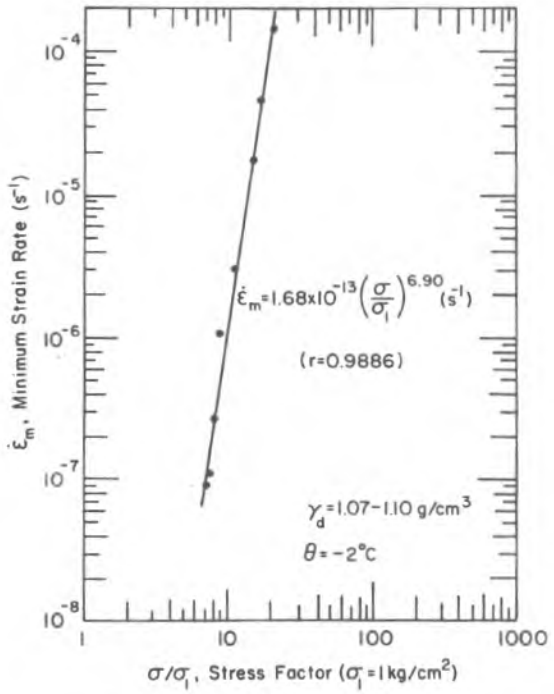

Figure 33. Log$\dot{\varepsilon}_m$ vs log(σ/σ₁) curves for the specimens with low density at -2 °C.

The effect of dry density on creep behavior can also be seen by comparing Figures 32 and 33 with Figure 21. Figure 32 is a plot of $\log\dot{\varepsilon}_m$ vs $1/\sigma$ for high-density samples at -2°C, showing a curve similar to that for medium density. The critical creep rate for samples with high density is also about 10^{-6} s^{-1}, and the critical creep strength σ_c is about 11.5 kg/cm² at -2°C. However, samples with low density possess a different creep behavior. As shown in Figure 33, the $\log\dot{\varepsilon}_m$ vs $\log(\sigma/\sigma_1)$ curve for low density is nearly a straight line over a wide range of $\dot{\varepsilon}_m$, which is similar to the creep response of ice. Consequently, the creep law of ice-rich frozen silt can be described by a simple power-law equation:

$$\dot{\varepsilon}_m = c_1(\sigma/\sigma_1)^n \qquad (19)$$

where c_1 is the mimimum creep rate when $\sigma = \sigma_1$. For the frozen silt tested, $c_1 = 1.68\times10^{-13}$ s^{-1} and $n = 6.90$ for $\theta = -2$°C.

The change in creep behavior due to the variation of density is attributed to the change in deformation mechanism. According to Sayles (1973) and Sayles and Carbee (1981), the stress resistance of a saturated frozen silt is composed of the bonding force and the frictional resistance between soil particles combined with that of the fractured ice crystals. For samples with different densities, different components of the stress resistance domi-

nate the creep process. At low density, most of soil particles are suspended in an ice matrix, so the deformation behavior of the ice matrix dominates the creep process. This explains why the ice-rich frozen silt has a creep behavior similar to that of ice. For dense frozen soil, however, with the increase in the number of contacts between mineral particles, the frictional force between particles (Sayles 1973) becomes more important for governing the creep process. There may exist a threshold for breaking the bonding force between soil particles. When the external shear stress acting on the contact areas is high enough to overcome this threshold, the glide between soil particles will take place. In this case, the frictional resistance between soil particles, as well as between fractured ice crystals, will dominate the creep rate, and the resistance is not so sensitive to the sample density for frozen silt, as is indicated by the curves in Figure 31 for higher stresses. When gliding starts, plastic deformation will continuously grow until creep rupture occurs, resulting in a type of typical ductile failure. This type of creep is called glide creep in this report.

We hypothesize that when external shear stress is less than the threshold, soil particles cannot glide by each other. In this case the creep process is controlled by the dislocation of pore ice, and the dislocation velocity determines the creep rate. This type of creep is called dislocation creep in this report. For the dense frozen soil, the closely packed soil particles greatly impede the movement of dislocation of the pore ice, so that the secondary creep rates at lower stresses are much smaller, as observed. On the basis of dislocation theory, the dislocation is rapidly multiplied along slip planes with increasing strain. The increase in the number of dislocations greatly weakens the shear resistance of frozen soil on the slip planes, so that dislocation creep usually leads to a type of plastic failure with visible $\times$-shaped cracks, as shown in Figure 19, especially for high densities.

Based on this interpretation, the short-term creep is primarily controlled by glide creep, while the long-term creep is governed by dislocation creep. Also, this explanation gives the critical creep strength σ_c a clear physical meaning: It is the macroanalytical measure of the threshold for breaking bonding force between soil particles. Theoretically, the bonding force increases with the decrease in unfrozen water content and the distance between mineral particles. According to this, the critical creep strength should increase with decreasing temperature and increasing dry density. In the preceding discussion, we have shown this to be true.

Effect of saturation

The partially saturated samples discussed here refer to the samples saturated under normal atmospheric pressure at a nominal dry density of 1.2 g/cm^3. The original purpose for making these samples was to examine the degree of saturation of samples saturated without benefit of a vacuum. We expected the degree of saturation to be considerably lower than 100%. However, it was higher than expected. As shown in Tables 3 and 5, the degree of saturation S is as high as 95–96%. Comparing the creep test results of the saturated and the partially saturated samples for the same test conditions (Tables 2 and 3), we found that the minimum creep rates of partially saturated samples are consistently higher than those of partially samples, even though the saturation degree for the former is only 3–4% less than that for the latter. This may be because there is less ice and therefore greater stress in the ice in the partially saturated samples, so the creep rate becomes higher.

Time to creep failure

The test results here and elsewhere indicate that the time to creep failure t_m strongly depends on stress, temperature and dry density.

Stress dependence

Figure 34 presents a set of $\log t_m$ vs $1/\sigma$ curves for the test silt with medium density at vari-

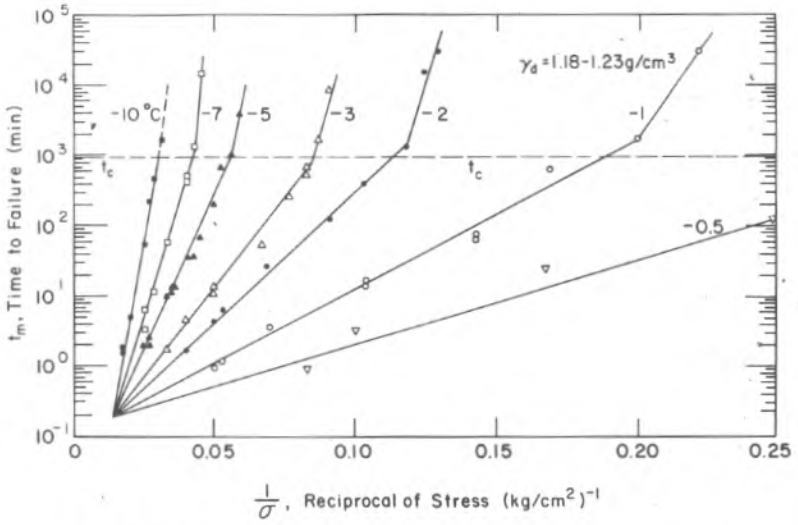

Figure 34. Plot of logt_m vs $1/\sigma$ for various temperatures.

ous temperatures. The shapes of these curves are similar to those of the $\log\dot{\epsilon}_m$ vs $1/\sigma$ curves shown in Figure 21, and hence they can be described for short-term creep by

$$t_m = t_* \exp\left[k_1\left(\frac{1}{\sigma} - \frac{1}{\sigma_*}\right)\right] \tag{20}$$

where t_* is a reference constant independent of temperature. For the frozen Fairbanks silt with densities varying from 1.18 to 1.23 g/cm³, $t_* = 0.19$ min. The parameter k_1 as a function of temperature is shown in Figure 35 and can be determined by

$$\begin{aligned} k_1 &= 49.7(\theta/\theta_0)^{0.75} \qquad \text{for } -0.5° \geq \theta \geq -2°\text{C} \\ k_1 &= 40.3(\theta/\theta_0)^{1.02} \qquad \text{for } -2° \geq \theta \geq -7°\text{C}. \end{aligned} \tag{21}$$

For long-term creep,

$$t_m = t_c \exp k_1' \left(\frac{1}{\sigma} - \frac{1}{\sigma_c}\right) \tag{22}$$

where t_c is the time to failure corresponding to $\dot{\epsilon}_c$, which is independent of temperature. From the test data, t_c has a magnitude of about 900 min for Fairbanks silt with medium density. The parameter k_1' depends on temperature. Its variation with θ is shown in Figure 35 and can be represented by

$$k_1' = 118.8(\theta/\theta_0)^{0.92} \tag{23}$$

for $-0.5° \geq \theta \geq -7°$C.

From the definition of creep failure, the creep stress σ in eq 20 and 22 is the ultimate (maximum) strength (denoted as σ_{ult}) of fro-

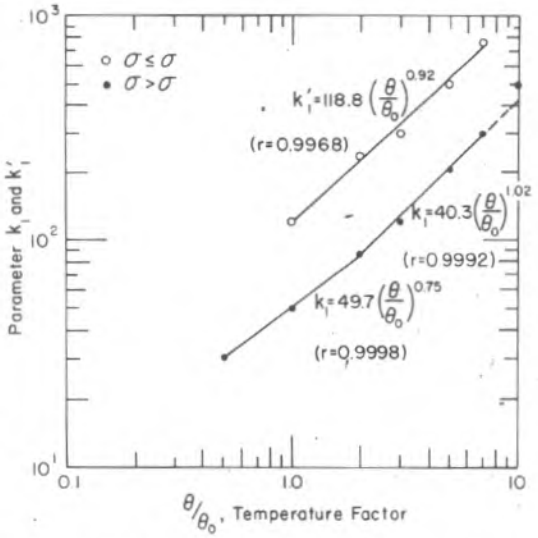

Figure 35. Parameters k_1 and k_1' as a function of temperature.

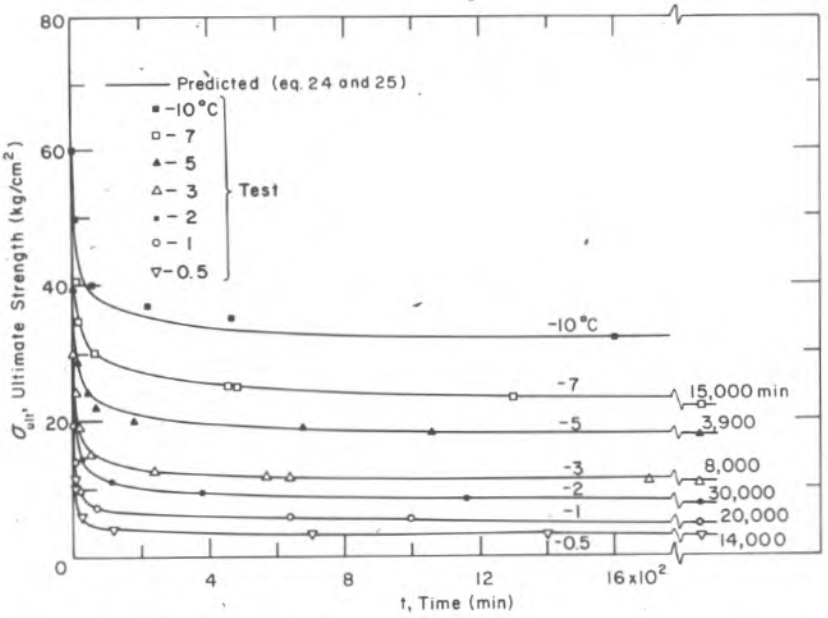

Figure 36. Comparison of the computed strength–time curves with test data.

zen soil when the time of loading is the same as the time of creep failure. Then, from eq 20 and 22 one can write the following strength relaxation equations:

$$\sigma_{ult} = \frac{k_1 \sigma_*}{\sigma_* \ln(t/t_*) + k_1} \qquad \text{for } t < t_c \tag{24}$$

and

$$\sigma_{ult} = \frac{k_1' \sigma_c}{\sigma_c \ln(t/t_c) + k_1'} \qquad \text{for } t \geq t_c. \tag{25}$$

These two equations can be used to predict the ultimate strength of the frozen silt with medium density at any given time of loading. The curves predicted by the two equations agree well with the test data (Fig. 36).

It should be especially noted that one cannot predict long-term strength by simply extrapolating short-term creep data. To predict long-term strength, of course, eq 25 should be used.

Following general criteria, if we assume that the 100-year strength is the limiting long-term strength σ_{lt}, then it can be calculated by eq 25 with t = 100 years = 5.25×10^7 min. The predicted values of σ_{lt} as a function of temperature for frozen Fairbanks silt with the dry densities varying from 1.18 to 1.23 g/cm³ are shown in Table 7 and Figure 37, and can be expressed as

$$\sigma_{lt} = 3.49(\theta/\theta_0)^{0.87} \tag{26}$$

where σ_{lt} is in kg/cm².

The predicted values of σ_{lt} for the Fairbanks silt were compared with those for the same (or similar)

Table 7. Predicted values of σ_{lt} for frozen Fairbanks silt with medium density at various temperatures.

θ (°C)	σ_{lt} (kg/cm²)	θ (°C)	σ_{lt} (kg/cm²)
-0.5	1.95	-3	8.81
-1	3.50	-5	14.22
-2	6.20	-7	18.67

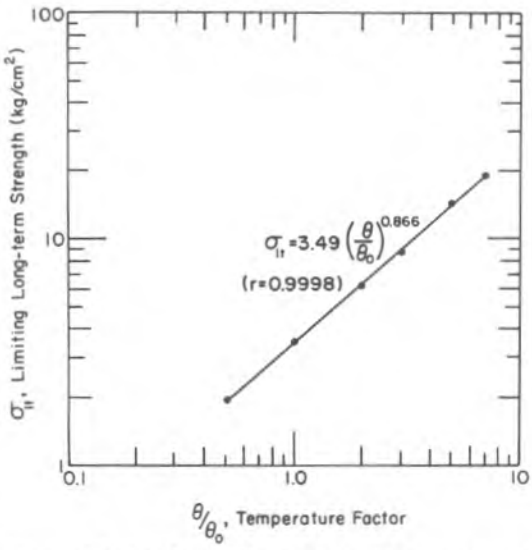

Figure 37. Predicted limiting long-term strength as a function of temperature.

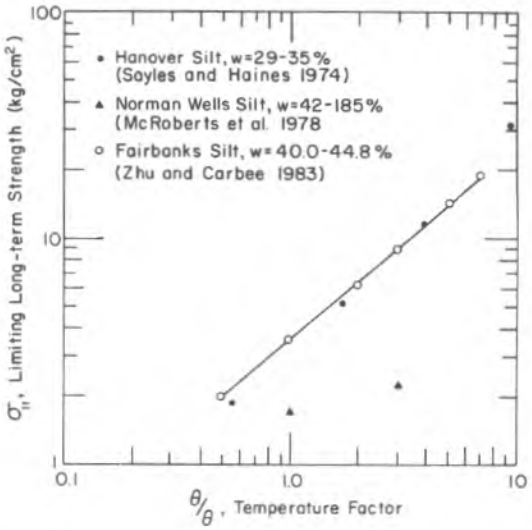

Figure 38. Limiting long-term strengths predicted by various investigators.

material with different water contents (Fig. 38). The values predicted by eq 25 are considerably higher than those for undisturbed ice-rich frozen silt reported by McRoberts et al. (1978). This is reasonable because the dry densities for the latter are much higher than those for the former. The values of σ_{lt} predicted by eq 25 should be lower than those reported by Sayles and Haines (1974), because the dry densities of samples prepared in his investigation are higher than those in this study. However, Figure 38 shows that the results are almost the same. This is probably because the predicted values of σ_{lt} in Sayles's report were obtained by extending short-term creep data, which may considerably underestimate long-term strength.

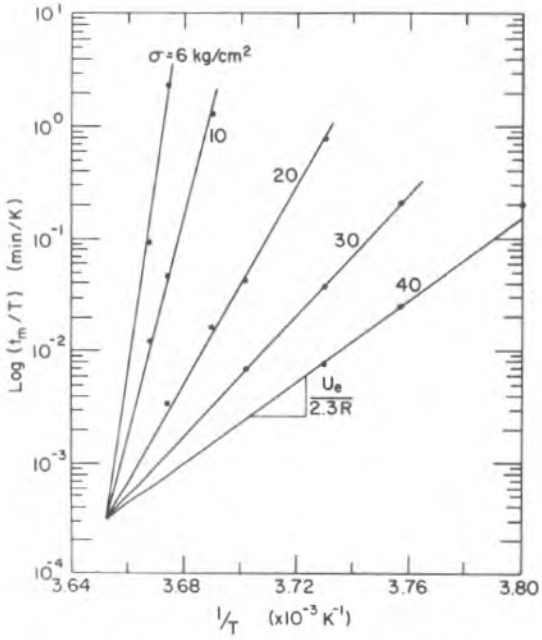

Figure 39. Plot of log(t_m/T) vs 1/T.

Temperature dependence

By plotting a graph of $\log(t_m/T)$ against $1/T$ from the test data (Fig. 39), it was found that the temperature dependence of time to failure t_m can be also evaluated in terms of an exponential expression:

$$t_m = A_2 T \exp\left[\frac{U_e}{R}\left(\frac{1}{T} - \frac{1}{T_0}\right)\right] \tag{27}$$

where A_2 is a constant equal to 2.8×10^{-4} min/K for the silt with medium density.

To compute U_e, eq 27 is rewritten as

$$U_e = 2.3R\,[B_1 + \log(t_m/T)]/\left(\frac{1}{T} - \frac{1}{T_0}\right) \tag{28}$$

where $B_1 = -\log A_2 = 3.55$. The values of U_e from the test data calculated with eq 28 are plotted in Figure 40 in terms of $\log U_e$ vs $\log(\sigma/\sigma_1 + 1)$. Obviously the data in this graph can be also fitted by eq 15 very well. By linear regression analysis, we found from Figure 40 that $\Delta F = 8100$ kcal/mole and $\delta = 1.21$, which are very close to those from Figure 28. This implies that there is a definite relationship between minimum creep rate and time to failure. This will be discussed in detail in the next section.

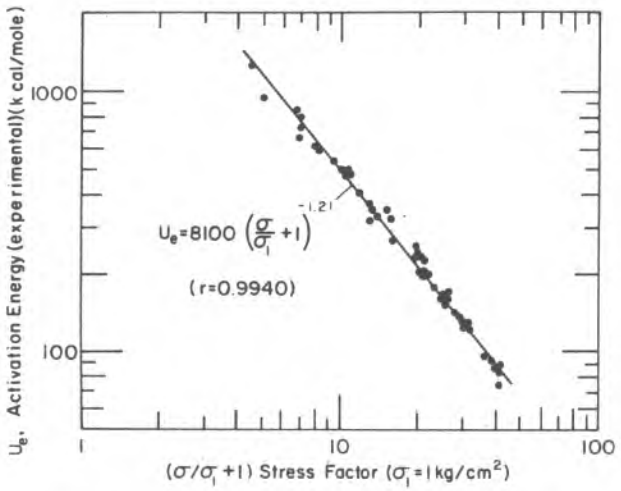

Figure 40. Plot of log U_e vs $\log(\sigma/\sigma_1 + 1)$.

Effect of dry density

Figure 41 shows time to failure t_m as a function of dry density γ_d for different stresses at -2°C. Dry density clearly has a significant influence on t_m: The denser the saturated frozen silt, the longer the time to failure. Especially at lower stresses, the time to failure for the dense frozen silt is much longer than for ice-rich frozen silt.

Figure 42 is a plot of $\log t_m$ vs $\log(\sigma/\sigma_1)$ for the low-density samples at -2°C. The result is a straight line, so the time-to-failure equation for low density has the form

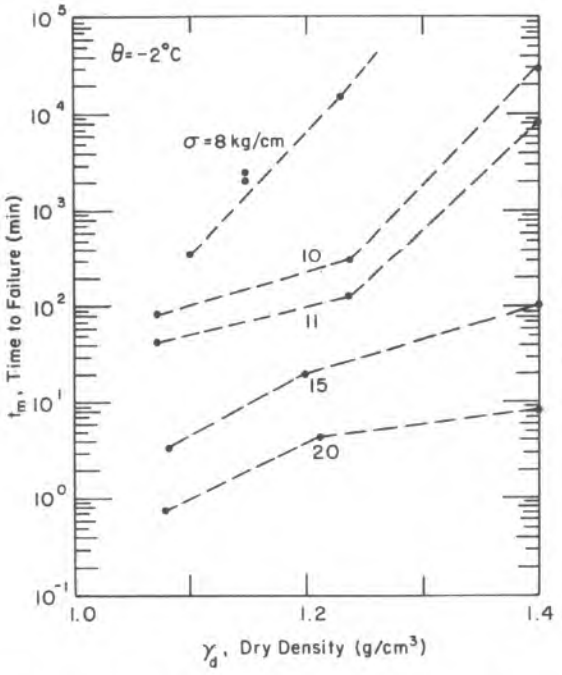

Figure 41. Time to failure as a function of dry density for different stresses at -2°C.

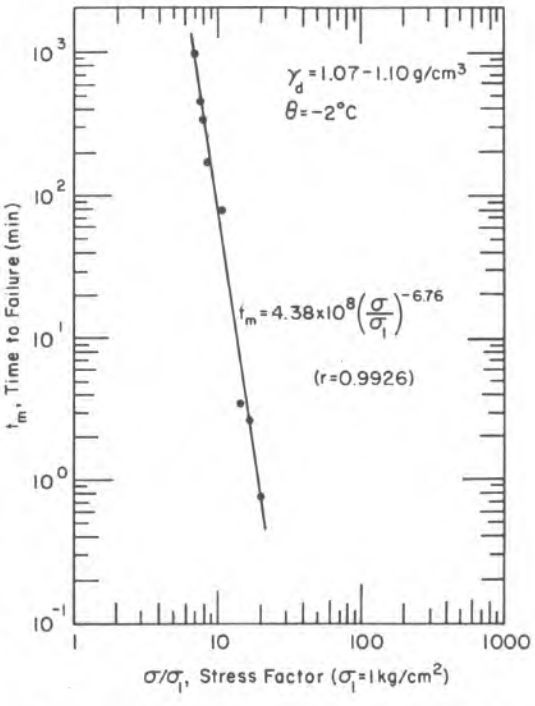

Figure 42. Plot of $\log t_m$ vs $\log(\sigma/\sigma_1)$ for the specimens with low density at -2°C.

$$t_m = t_{m1}(\sigma/\sigma_1)^{-n} \quad (29)$$

where t_{m1} is the time to failure when $\sigma = \sigma_1 = 1$ kg/cm². For the frozen silt, $t_{m1} = 4.38 \times 10^8$ min and $n = 6.76$ for $\theta = -2°C$.

Figure 43 is a plot of $\log t_m$ vs $1/\sigma$ for the high-density samples at -2°C. The curve in this graph seems to break at a critical stress σ_c of about 11.5 kg/cm²; the curve can be described by

$$t_m = t_{mo}\, e^{k_o/\sigma} \quad (30)$$

where t_{mo} and k_o depend upon the stress level for a given temperature. For example, for $\theta = -2°C$, $t_{mo} = 0.03$ min and $k_o = 116.4$ kg/cm² when $\sigma > \sigma_c$, and $t_{mo} = 0.4$ min and $k_o = 109.5$ kg/cm² when $\sigma \leq \sigma_c$.

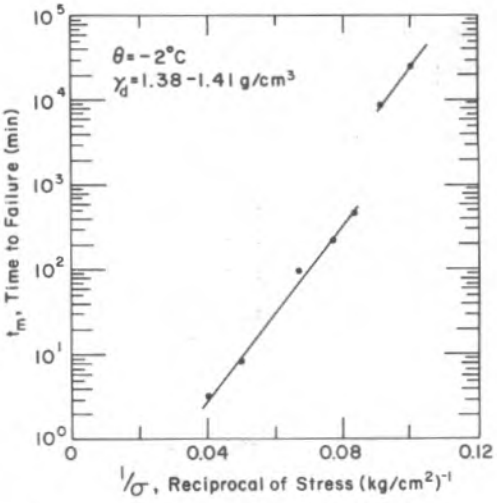

Figure 43. Plot of $\log t_m$ vs $1/\sigma$ for the specimens with high density at -2°C.

Relationship between $\dot{\varepsilon}_m$ and t_m

In each plot in Figure 17, one can draw a straight line that nearly passes through all the minimum points of $\log\dot{\varepsilon}$ vs $\log t$ curves over a certain range of testing stresses. Similar results were reported by Martin et al. (1981) for frozen sand. This suggests that there is a unique relationship between the minimum creep rate $\dot{\varepsilon}_m$ and the time to failure t_m over a certain range of stresses. A plot of all minimum points for various temperatures for medium-density samples (Fig. 44) shows that this relationship is identical for all test temperatures and can be expressed as

$$\dot{\varepsilon}_m = 0.086 t_m^{-1.06} \quad (31)$$

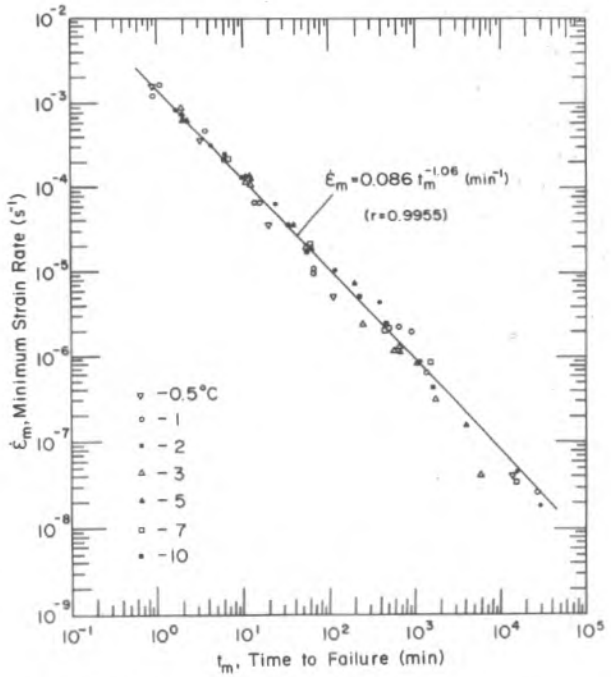

Figure 44. Plot of $\log\dot{\varepsilon}_m$ vs $\log t_m$ for the specimens with medium density.

where t_m is in minutes, and $\dot{\epsilon}_m$ is in min^{-1}. From Figure 17i, this relationship for low-density samples at -2°C is

$$\dot{\epsilon}_m = 0.0083 t_m^{-1.01}. \tag{32}$$

In Figure 17h, one cannot draw a straight line through all of the minimum points over the whole range of test stresses because of the large drop of $\dot{\epsilon}_m$ at lower stresses. However, if only a certain range of stresses (say, $\sigma > \sigma_c$) is considered, the unique relationship between $\dot{\epsilon}_m$ and t_m may still exist and can be written as

$$\dot{\epsilon}_m = 0.18 t_m^{-1.16}. \tag{33}$$

Thus, the relationship between $\dot{\epsilon}_m$ and t_m has the general form

$$\dot{\epsilon}_m = C\, t_m^{-p}$$
or
$$\dot{\epsilon}_m\, t_m^{p} = C \tag{34}$$

where p depends only on dry density, and C depends on the unit of time and the dry density if p is not 1. The values of p and C for different ranges of dry density are summarized in Table 8.

Table 8 shows that the value of p for the lower densities is very close to 1, the same as the reported value for polycrystalline ice (Mellor and Cole 1982, Cox et al. 1984). However, it is significantly greater than 1 for the highest density. Therefore, the simple form $\dot{\epsilon}_m \propto 1/t_m$ is not applicable to dense frozen soil.

Table 8. Values of p and C in eq 34 for different dry densities. The unit of time is minutes.

γ_d (g/cm^3)	p	C
1.07–1.10	1.01	0.0083
1.18–1.23	1.06	0.0860
1.38–1.41	1.16	0.1800

Creep failure strain and failure criterion

The creep failure strains ϵ_f of samples with medium density as a function of $\dot{\epsilon}_m$ for various temperatures are plotted in Figure 45. Within the accuracy of the test, it seems that the failure strain for medium-density samples does not depend on $\dot{\epsilon}_m$ and θ over a wide range of $\dot{\epsilon}_m$. However, some samples did not fail until the strain was more than 15% for high temperatures (≥ -1°C) and low stresses.

Figure 46 shows the creep failure strains as a function of $\dot{\epsilon}_m$ for different dry densities at -2°C. It clearly shows that the failure strain strongly depends on dry density. For example,

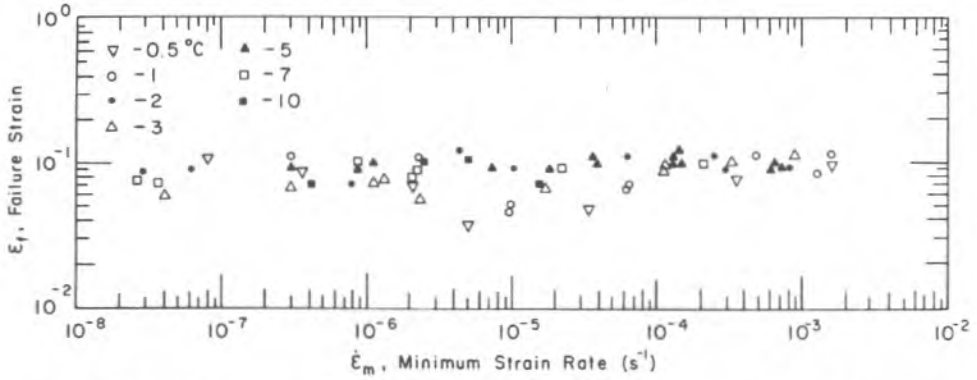

Figure 45. Failure strain as a function of $\dot{\epsilon}_m$ for specimens with medium density at various temperatures.

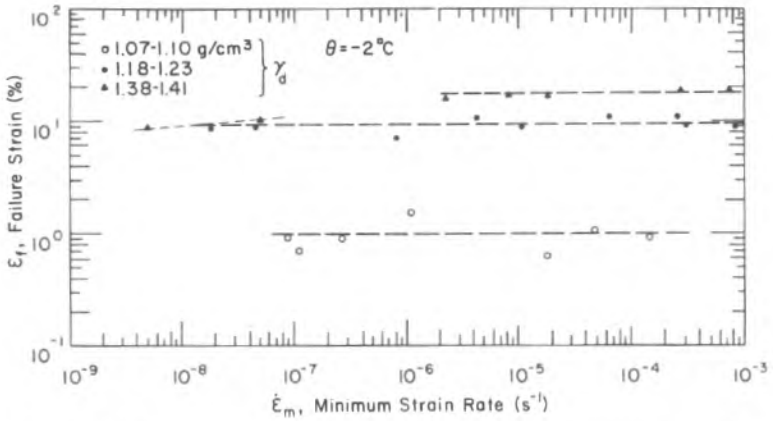

Figure 46. Failure strain as a function of $\dot{\epsilon}_m$ for specimens with various dry densities at -2°C.

Table 9. Average values of ϵ_f for frozen Fairbanks silt with various dry densities at -2°C.

γ_d (g/cm³)	ϵ_f*
1.07–1.10	0.0101
1.18–1.23	0.0870
1.38–1.41	0.1760

*From the constant-stress creep tests.

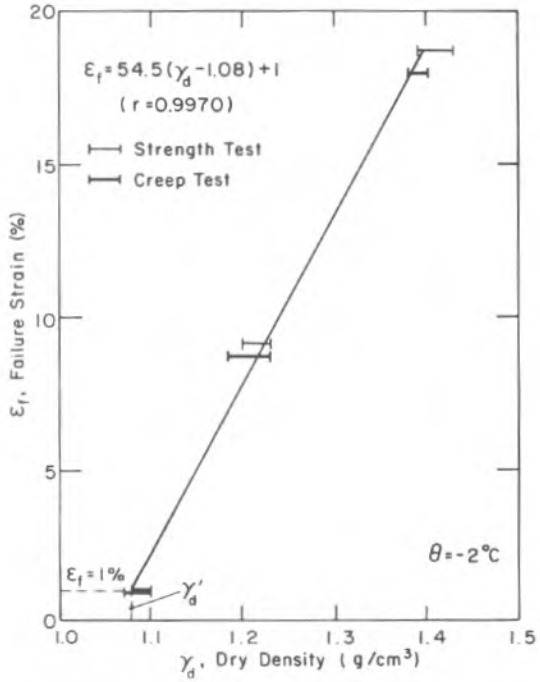

Figure 47. Failure strain as a function of dry density.

the failure strain decreases from about 18% to 1% as dry density decreases from 1.4 to 1.08 g/cm³ at the higher range of $\dot{\epsilon}_m$. Therefore, it is incorrect to take 20% strain as a creep failure criterion for plastic frozen soils without taking into consideration the density or water content. Different failure criteria for frozen soil should be selected in accordance with the density and the failure mode.

Figure 46 shows that the creep failure strain for low-density samples does not vary with $\dot{\epsilon}_m$. It has an average value of about 1%, which is very close to that of polycrystalline ice (Mellor and Cole 1982). But the failure strain for high densities varies with $\dot{\epsilon}_m$; ϵ_f suddenly decreases from about 16% to 10% as $\dot{\epsilon}_m$ decreases from 2.2×10^{-6} to 5.0×10^{-8} s^{-1}. When $\dot{\epsilon}_m$ is greater than 2.2×10^{-6} s^{-1}, ϵ_f increases slightly with increasing $\dot{\epsilon}_m$ but can be considered practically constant. Its average value, together with that of samples of medium and low density at -1°C, is illustrated in Table 9 and Figure 47. From Figure 47 the creep failure strain of saturated frozen silt as a function of dry density can be simply evaluated by

$$\epsilon_f = 54.5(\gamma_d - \gamma_d') + 1 \qquad (35)$$

Table 10. Average values of $\epsilon_f - \epsilon_0$ for different dry density groups at −2°C.

γ_d (g/cm³)	$\epsilon_f - \epsilon_0$
1.07–1.10	0.0086
1.18–1.23	0.084
1.38–1.41	0.173

where ϵ_f is in percent, and γ_d' is the dry density at which $\epsilon_f = 1\%$. For the frozen silt tested, $\gamma_d' = 1.08$ g/cm³.

Using the values of the initial tangent modulus E_i of the frozen silt for constant-strain-rate tests shown in Table 4, we calculated the instantaneous strain ϵ_0 by simply using $\epsilon_0 = \sigma/E_i$. Then the quantity $\epsilon_f - \epsilon_0$ can be computed for each specimen (Table 10). The values of $\epsilon_f - \epsilon_0$ are nearly equal to the values of C in Table 8. Thus, substituting $\epsilon_f - \epsilon_0$ for C in eq 34 we obtained the following creep failure criterion:

$$\dot{\epsilon}_m t_m^p = \epsilon_f - \epsilon_0. \tag{36}$$

Neglecting ϵ_0, eq 36 becomes

$$\dot{\epsilon}_m t_m^p = \epsilon_f. \tag{37}$$

Again, the unit of time in this equation must be in minutes if p is not equal to 1. This criterion is very useful because it links three basic creep failure parameters in a simple mathematical form. When p is 1, eq 37 reduces to

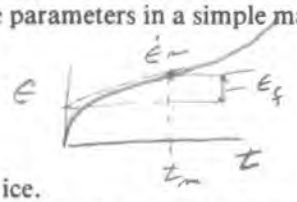

$$\dot{\epsilon}_m t_m = \epsilon_f \tag{38}$$

which is exactly the same as Assur's (1980) criterion for ice.

Ladanyi (1972) proposed a criterion for frozen soil of the same simple form as eq 38. As discussed above, applying eq 38 to ice-rich frozen soil is acceptable, but applying it to dense frozen soil will lead to significant errors.

Creep model and prediction of creep strain

To predict the time-dependent deformation of frozen soil, a number of researchers have been working for many years to establish a quantitative creep model. Since the creep process of frozen soil is very complicated, especially for warm plastic frozen soil, it is difficult to develop a mechanistically based quantitative model involving all the primary creep variables. It is possible, but the model must be exceedingly complex. Therefore, empirical modeling is by far the most popular approach.

To predict creep deformation for frozen soil, various creep models have been developed. In 1962, Vialov proposed a primary creep model that has been widely used in practice and has been successfully applied to various frozen soils (Sayles 1968, Sayles and Haines 1974). Ten years later, Ladanyi (1972) developed a secondary creep model (an engineering creep theory) based on Hult's (1966) creep theory on metals. Ladanyi's model has also been used in engineering because of its simplicity.

However, great care must be taken in using these primary and secondary creep models, since they apply only for the duration for which they were formulated. For example, the secondary creep model overestimates creep strain during primary creep, while both the primary and secondary creep models underestimate strain during tertiary creep.

A similar tertiary creep model, developed from three different perspectives by Assur (1980), Fish (1980) and Ting (1981), can be used to describe the entire process of creep. In this study, Assur's model is used to fit the creep data. Based on the study of creep of ice, Assur (1980) developed a simple creep model that is derived from a differential equation quantifying the physical basis of creep and has the form

$$\dot{\epsilon}(t) = (\dot{\epsilon}_m/\epsilon^\beta)(t_m/t)^\beta \, e^{\beta t/t_m} \tag{39}$$

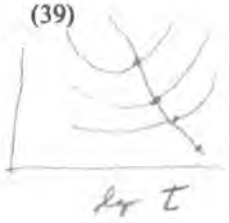

Table 11. Values of β in eq 39.

γ_d	*Values of* β	
(g/cm³)	$\sigma > \sigma_c$	$\sigma \leq \sigma_c$
1.38–1.41	0.7	0.88
1.18–1.23	$0.23\, t_m^{0.11}$	0.6
1.07–1.10	$0.3\ t_m^{0.09*}$	

* (t_m < 1000 min).

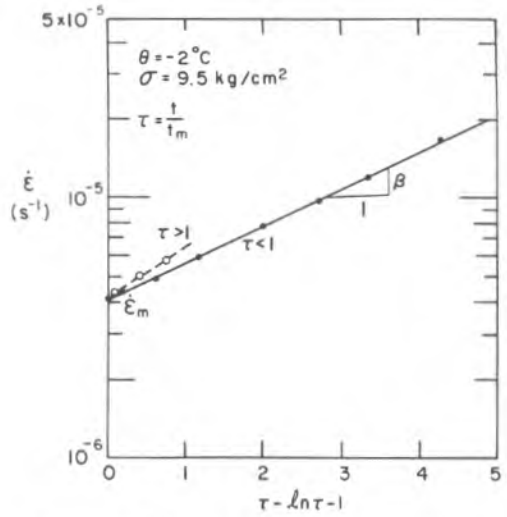

Figure 48. Determination of parameter β.

where β can be determined by taking logarithms of both sides of eq 39 and plotting $\ln\dot{\epsilon}$ vs $(\tau - \ln\tau - 1)$, as shown in Figure 48, in which $\tau = t/t_m$. We found in this investigation that β varies with time to failure t_m and dry density γ_d. Its average values are shown in Table 11.

The curves predicted by eq 39 were compared with the observed $\log\dot{\epsilon}$ vs $\log t$ curves as shown in Figures 17e, h and i. The comparison shows that eq 39 can be used to fit the test curves very well for low-density samples, as well as for medium- and high-density samples for short-term creep, but it does not fit the test curves as well for long-term creep. As is shown in Figures 17e and h, it considerably underestimates $\dot{\epsilon}$ during primary and tertiary long-term creep, because of the large drop of $\dot{\epsilon}_m$.

Integrating eq 39 and taking into consideration eq 37 and instantaneous strain ϵ_0, we derived the following creep equation:

$$\epsilon(t) = \epsilon_0 + \frac{\epsilon_f}{e^{\beta} t_m^{\beta-1}} \left(\frac{t}{t_m}\right)^{1-\beta} e^{\beta t/t_m} \left[\frac{1}{1-\beta} - \frac{\beta t/t_m}{(1-\beta)(2-\beta)} + \frac{(\beta t/t_m)^2}{(1-\beta)(2-\beta)(3-\beta)} - \ldots\right]. \quad (40)$$

Equation 40 is not applicable for long-term creep of frozen silt with a high density because of the invalidity of eq 39. In this case the creep equation obtained from integrating eq 39 has the form

$$\epsilon(t) = \epsilon_0 + \frac{\dot{\epsilon}_m t_m}{e^{\beta}} \left(\frac{t}{t_m}\right)^{1-\beta} e^{\beta t/t_m} \left[\frac{1}{1-\beta} - \frac{\beta t/t_m}{(1-\beta)(2-\beta)} + \frac{(\beta t/t_m)^2}{(1-\beta)(2-\beta)(3-\beta)} - \ldots\right]. \quad (41)$$

All parameters in eq 40 and 41 can be determined by using the equations discussed earlier in accordance with the stress, temperature and dry density of concern.

A comparison was made between the computed curves by eq 40 and 41 and test data in Figure 49, showing that eq 40 can adequately describe the entire creep curves for the samples with low density, as well as for short-term creep of the samples with medium and high density. But eq 40 and 41 do not predict long-term creep as well. They considerably underestimate creep strain during primary and tertiary creep. As a first approximation, they are still applicable for describing the long-term creep deformation of frozen soil.

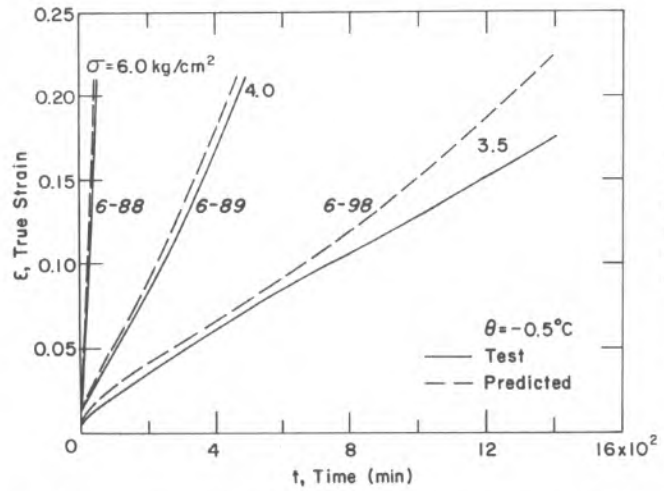

a. Short-term creep for medium-density samples at -0.5 °C.

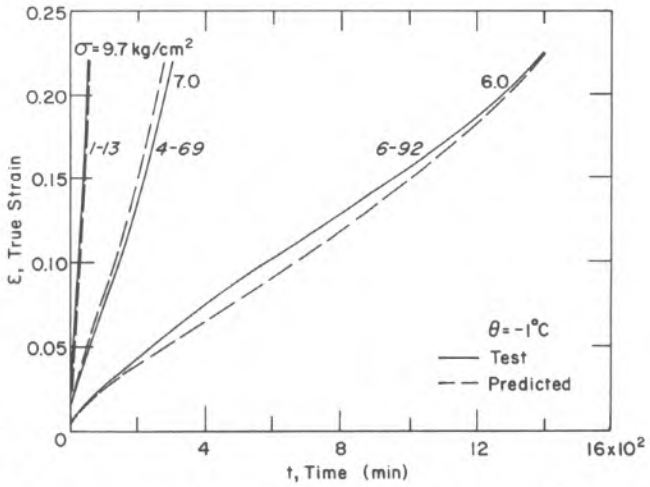

b. Short-term creep for medium density samples at -1 °C.

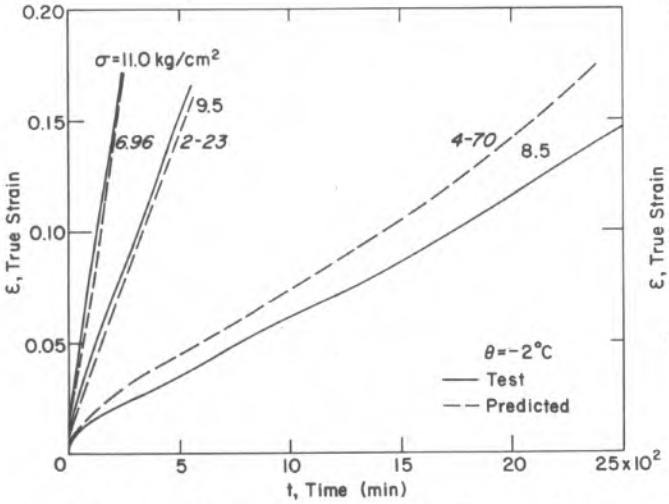

c. Short-term creep for medium-density samples at -2 °C.

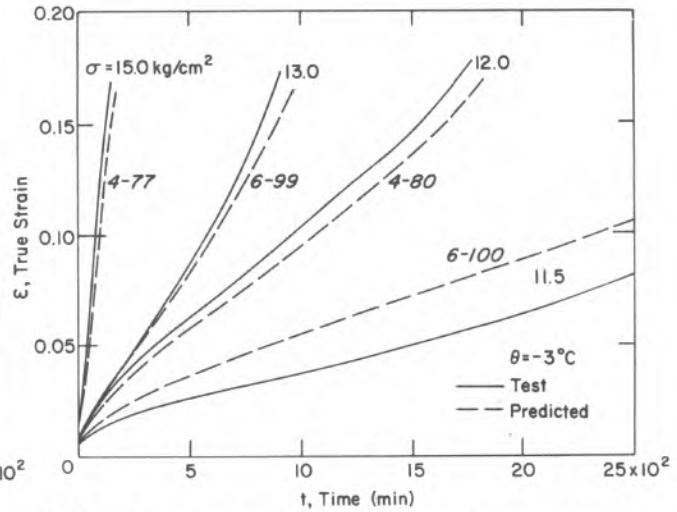

d. Short-term creep for medium-density samples at -3 °C.

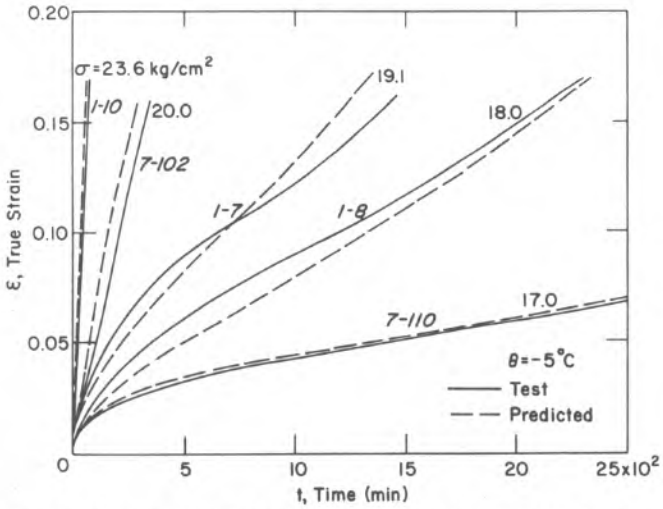

e. Short-term creep for medium-density samples at -5 °C.

Figure 49. Comparison between calculated and test curves.

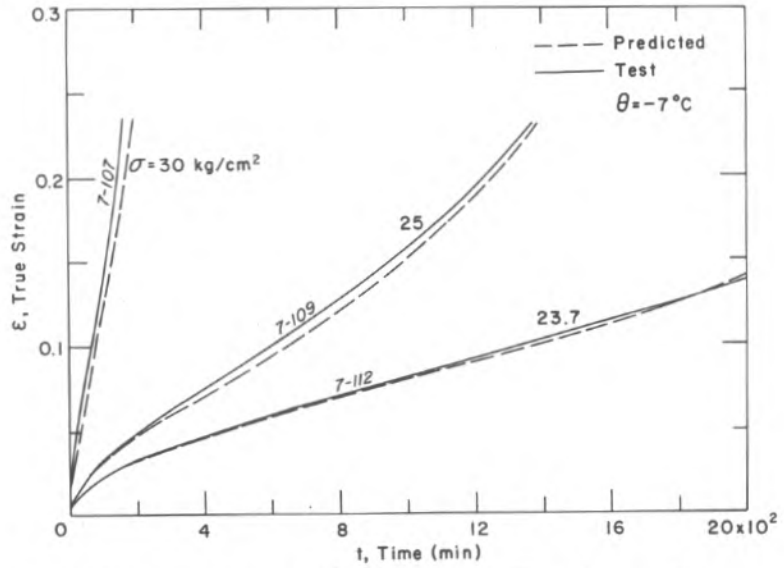

f. Short-term creep for medium-density samples at -7°C.

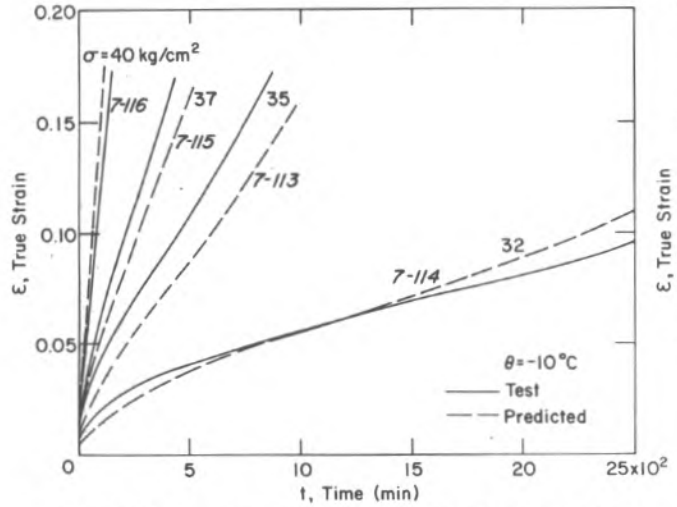

g. Short-term creep for medium-density samples at -10°C.

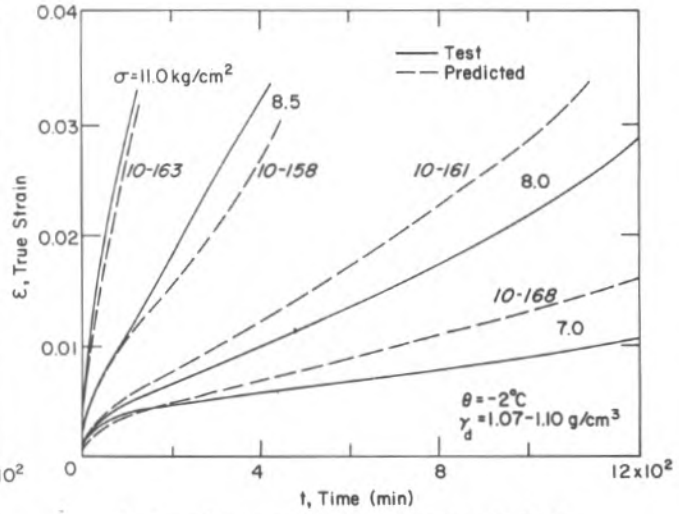

h. Specimens with low density at -2°C.

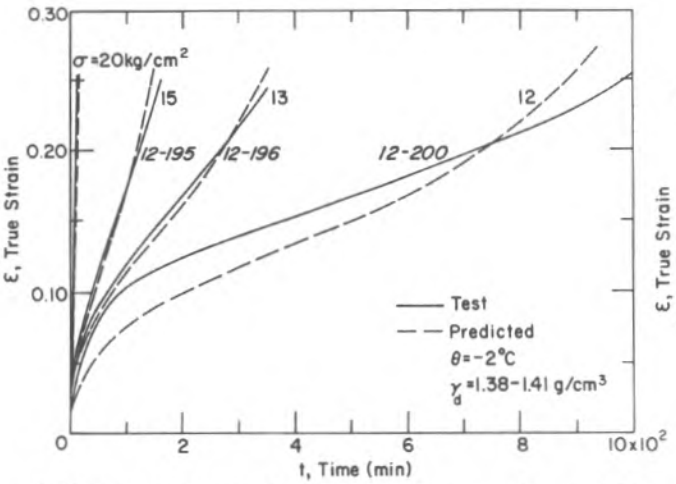

i. Short-term creep for high-density samples at -2°C.

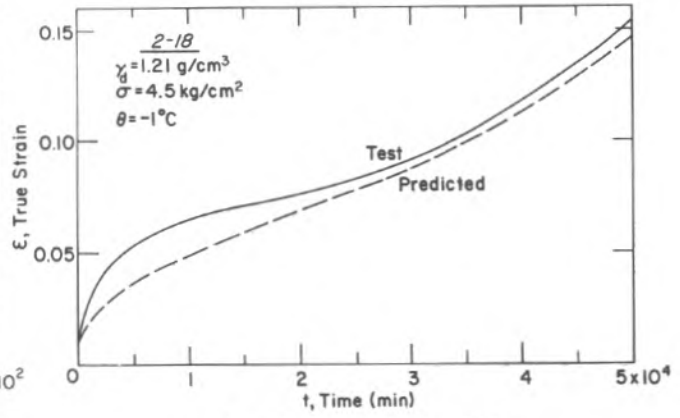

j. Long-term creep at -1°C.

Figure 49 (cont'd). Comparison between calculated and test curves.

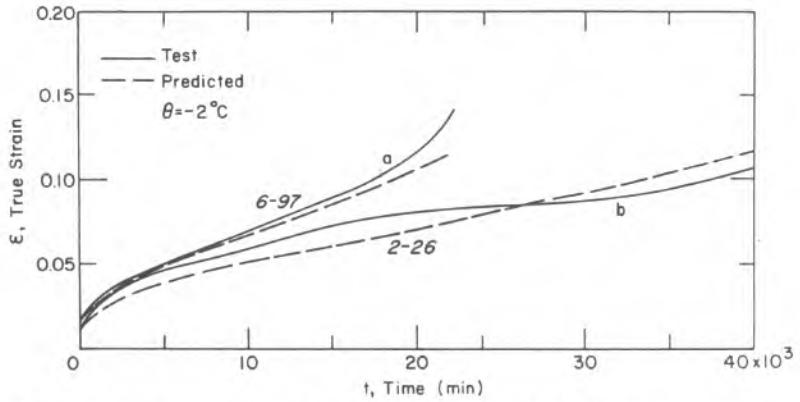

k. Long-term creep at -2°C for: a) γ_d = 1.230 g/cm³, σ = 7.9 kg/cm²; b) γ_d = 1.185 g/cm³, σ = 7.6 kg/cm².

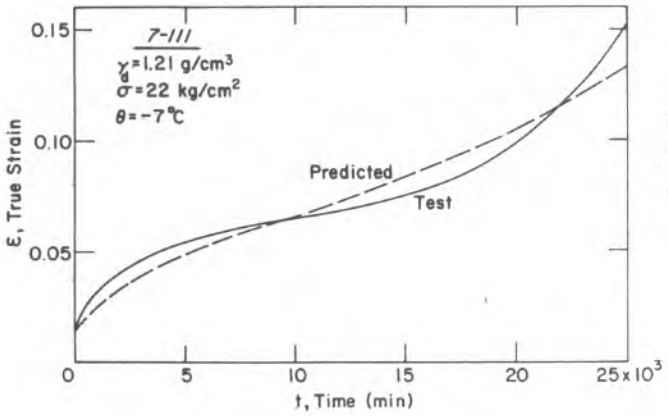

l. Long-term creep at -7°C.

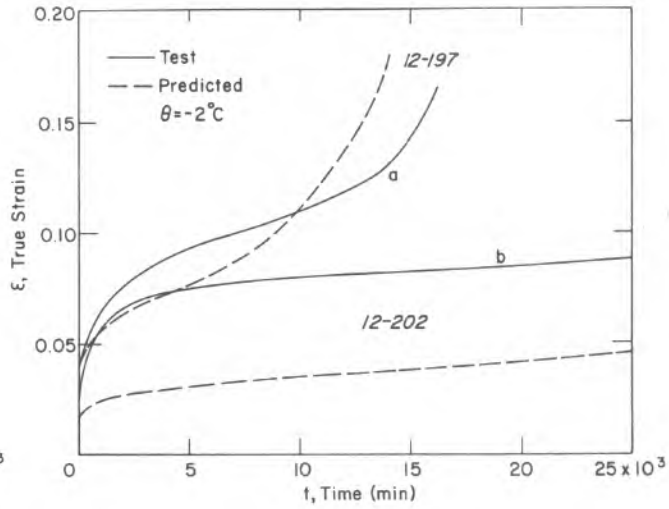

m. Long-term creep for: a) γ_d = 1.410 g/cm³, σ = 11 kg/cm²; b) γ_d = 1.407 g/cm³, σ = 10 kg/cm².

Figure 49 (cont'd).

STRENGTH BEHAVIOR

General stress-strain behavior and failure mode

The constant-strain-rate uniaxial compression tests show that none of the specimens failed in a typically brittle mode, but they failed in a ductile mode at the testing ranges of temperature and strain rate. That is, fracturing did not occur until the axial strain approached more than 25%. However, the results show that there is no sharp difference between ductile and brittle failures. In general, the failure mode gradually shifts from one to the other as the test conditions (such as temperature, strain rate and density) change. This transition can be clearly seen by comparing a series of stress-strain curves. For example, from Figure 14, which presents a set of stress-strain curves for specimens with medium density for various strain rates at -3°C, one can see that the brittleness of the samples gradually increases with increasing strain rates. A more significant change in brittleness seems to occur at a strain rate above 1.1×10^{-3} s^{-1}. As strain rates become greater than 1.1×10^{-3} s^{-1}, the stress-strain curves drop sharply after reaching a peak, indicating a great increase in the brittleness of the soil.

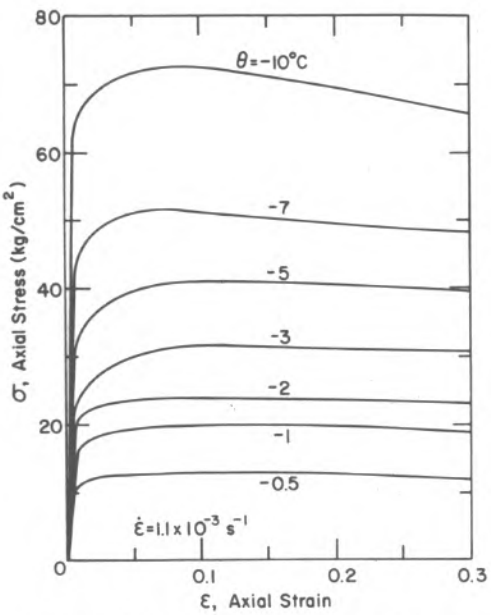

Figure 50. Typical stress–strain curves for various temperatures at a strain rate of $1.1 \times 10^{-3}\ s^{-1}$ for medium-density samples.

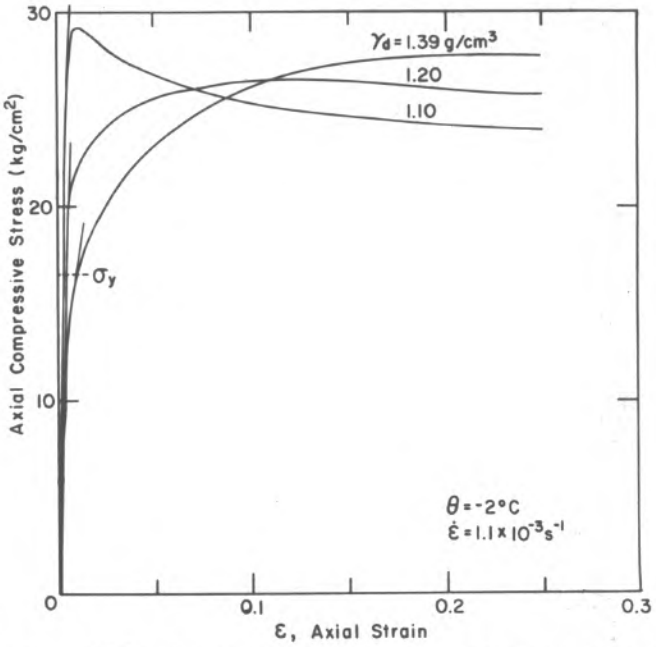

Figure 51. Typical stress–strain curves for various dry densities at a strain rate of $1.1 \times 10^{-3}\ s^{-1}$ and a temperature of –2 °C.

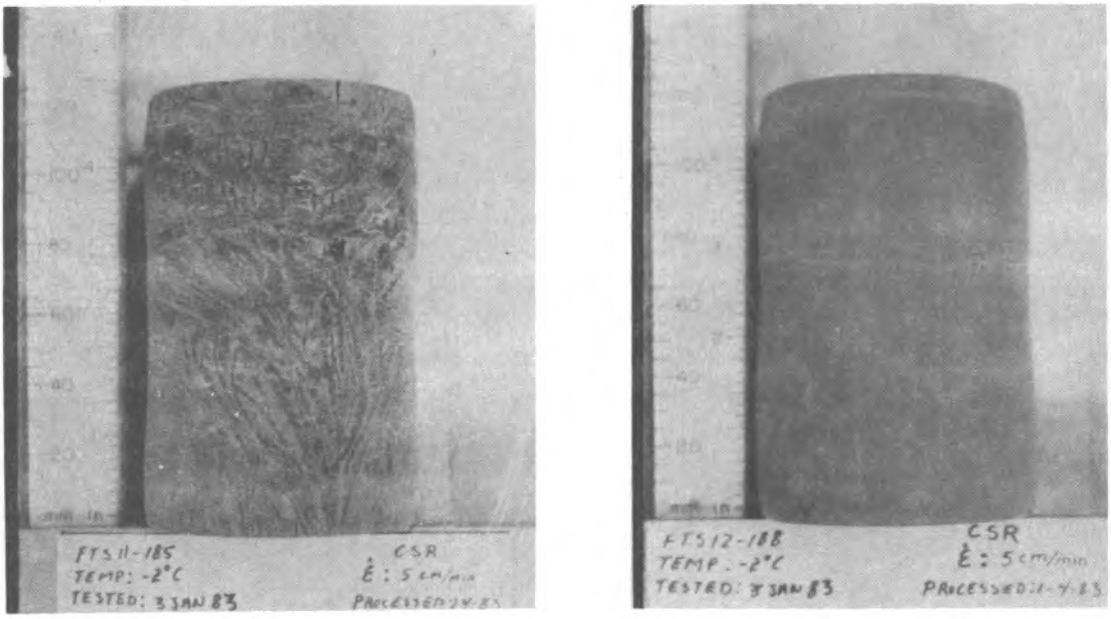

a. Cracks in a low-density sample.

b. No visible cracks in a medium-density sample.

Figure 52. Fairbanks silt specimens with different densities after testing at a fast machine speed of 5 cm/min and a temperature of –2 °C.

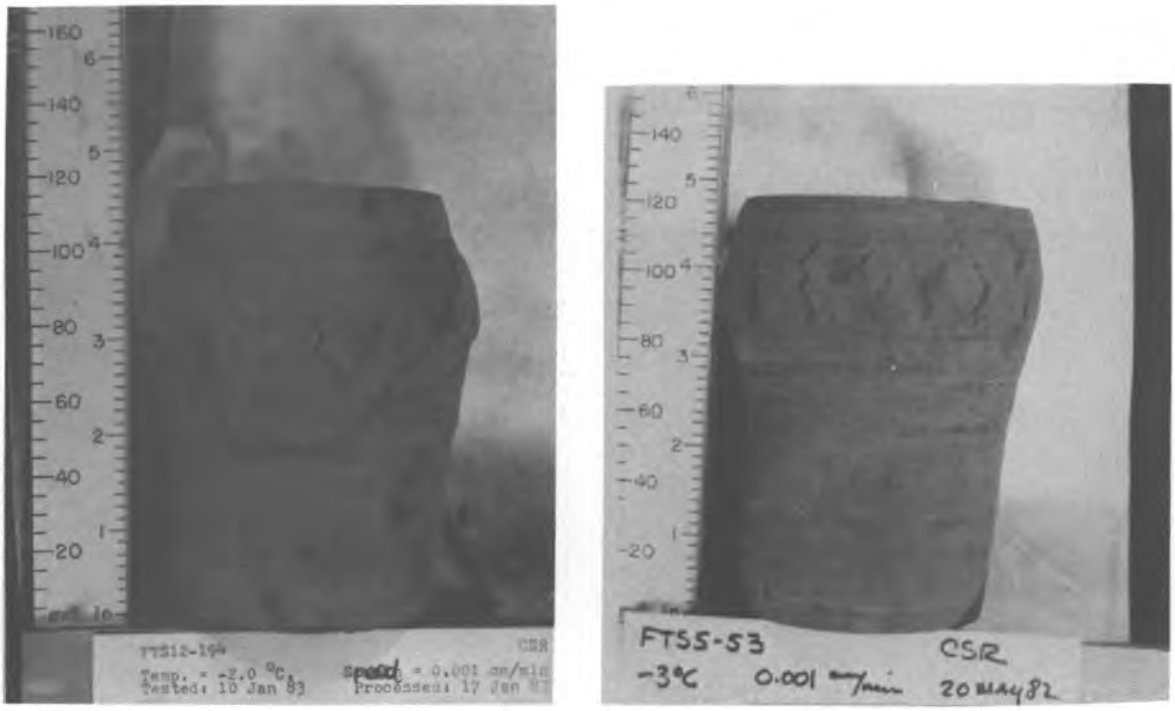

a. $\theta = -2°C$. *b.* $\theta = -3°C$.

Figure 53. Fairbanks silt specimens of medium density after testing at a slow speed of 0.001 cm/min., showing ×*-shaped shear cracks.*

Figure 50 illustrates a set of stress–strain curves for the samples with medium density for various temperatures at a strain rate of 1.1×10^{-3} s^{-1}. It shows that the samples behave as if the soil were more brittle as the temperature decreases. The tests show that the changes in density may also cause a transition of the failure mode. Figure 51 shows a typical set of stress–strain curves for three dry densities at a strain rate of 1.1×10^{-3} s^{-1} and a temperature of –2°C. It is obvious that the lower the dry density, the more brittle the soil. Figure 52 provides clear evidence to confirm this conclusion. Some visible cracks can be seen on the surface of the samples with low density (Fig. 52a), but no cracks can be seen on the samples with high density (Fig. 52b) at the same test temperature and strain rate.

The occurrence of cracks in a specimen does not always indicate that it failed in a brittle mode. In fact, as discussed earlier, ductile failure sometimes may also accompany the formation of larger visible cracks. For instance, the large ×-shaped cracks seen in Figure 53 resulted from a typical plastic failure of the samples deformed under a slow strain rate of about 1.1×10^{-6} s^{-1}.

Peak compressive strength

Figure 54 shows a plot of $\log\sigma_m$ vs $\log(\theta/\theta_0)$ for various applied strain rates $\dot{\varepsilon}$. It is clear from this figure that the peak compressive strength σ_m of the frozen silt significantly increases with decreasing temperature and increasing strain rate. As reported by Sayles and Haines (1974), the peak strength of frozen soil σ_m as a function of temperature can be written as

$$\sigma_m = A(\theta/\theta_0)^m \tag{42}$$

where A is an empirical parameter with the dimension of stress, and m is a dimensionless

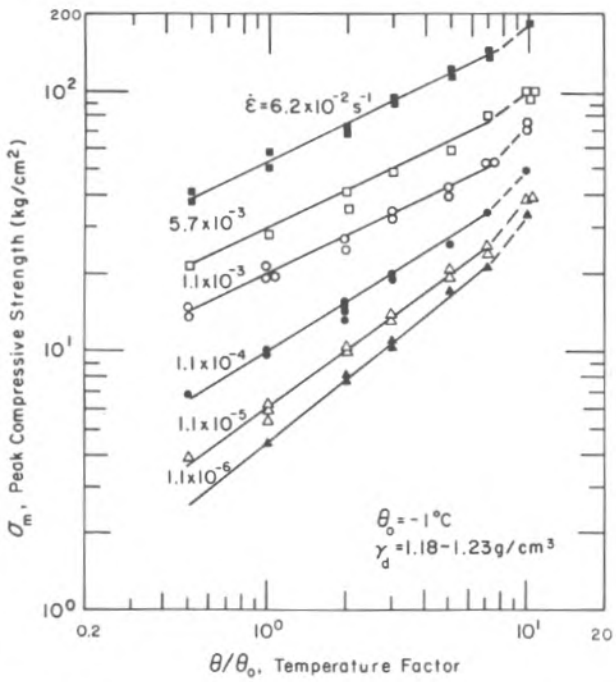

Figure 54. Logσ_m vs log(θ/θ_0) for various strain rates.

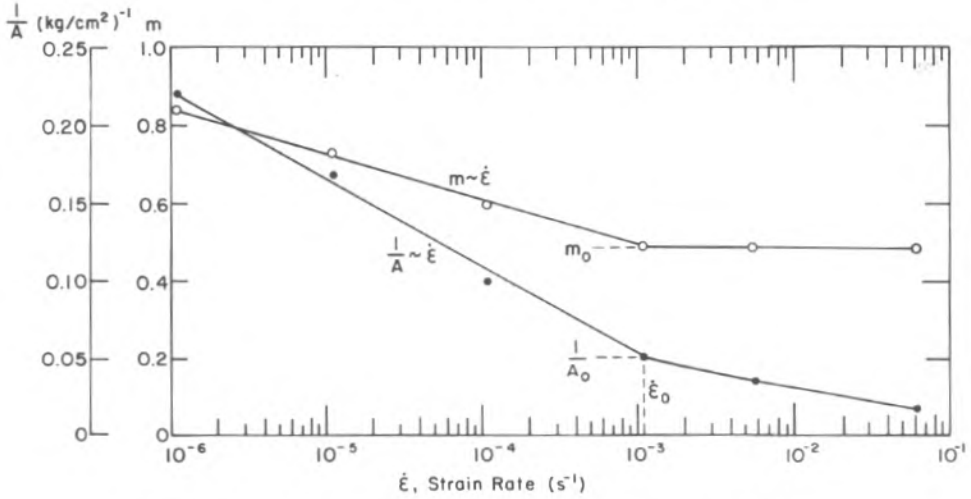

Figure 55. Parameters m *and 1/*A *as a function of strain rate.*

Table 12. Values of A and m in eq 43 for frozen Fairbanks silt with γ_d = 1.18–1.23 g/cm^3 at $\theta \geq$ -7°C.

$\dot{\varepsilon}$ (s^{-1})	A (kg/cm^2)	m	r
6.2×10^{-2}	53.8	0.49	0.9931
5.7×10^{-3}	29.0	0.49	0.9931
1.1×10^{-3}	19.1	0.49	0.9908
1.1×10^{-4}	10.2	0.59	0.9970
1.1×10^{-5}	6.0	0.73	0.9976
1.1×10^{-6}	4.5	0.84	0.9981

parameter. For a particular soil type and a certain range of temperature, parameters A and m depend on strain rates. The values of A and m, which were obtained by linear regression analysis, for various strain rates at $\theta \geq -7$°C are listed in Table 12 (including the values of correlation coefficient r) and plotted in Figure 55.

There is a significant change in the functional relationships of A and m with the strain rate at $\dot{\varepsilon} = 1.1\times10^{-3}$ s^{-1}. This may imply that different deformation mechanisms are dominant at different ranges of

strain rate. For $\dot{\epsilon} > 1.1\times10^{-3}$ s^{-1}, the deformation process of the frozen silt behaves as if the soil were more brittle, while for $\dot{\epsilon} < 1.1\times10^{-3}$ s^{-1}, it behaves as if the soil were more ductile. Hawkes and Mellor (1972) reported similar observations for fine-grained polycrystalline ice. Therefore, we suggest that a strain rate of about 1.1×10^{-3} s^{-1} be considered the critical strain rate characterizing the ductile–brittle transition of the failure mode for frozen silt.

From Figure 55, parameter A as a function of strain rate $\dot{\epsilon}$ can be expressed as

$$A = \frac{\alpha A_0}{\alpha + A_0 \ln(\dot{\epsilon}_0/\dot{\epsilon})} \tag{43}$$

where $\dot{\epsilon}_0 = 1.1\times10^{-3}$ s^{-1} is the strain rate hypothesized to be the transition of failure mode from ductile to moderate brittle for this frozen silt, $A_0 = 19.1$ kg/cm^2 is the value of A when $\dot{\epsilon} = \dot{\epsilon}_0$, and α is the reciprocal of the slope of the $\ln\dot{\epsilon}$ vs $1/A$ curve and has a value of 40 kg/cm^2 when 1.1×10^{-6} s^{-1} $\leq \dot{\epsilon} \leq \dot{\epsilon}_0$ and 86 kg/cm^2 for $\dot{\epsilon} \geq \dot{\epsilon}_0$.

Parameter m as a function of $\dot{\epsilon}$ can be written as

$$m = m_0 + 0.0517 \ln(\dot{\epsilon}_0/\dot{\epsilon}) \qquad \text{for } 1.1\times10^{-6} \text{ s}^{-1} \leq \dot{\epsilon} \leq \dot{\epsilon}_0$$

and (44)

$$m = m_0 = 0.49 \qquad \text{for } \dot{\epsilon} \geq \dot{\epsilon}_0.$$

Combining eq 42 and 43 yields a constitutive equation as follows:

$$\sigma_m = \frac{\alpha A_0 (\theta/\theta_0)^m}{\alpha + A_0 \ln(\dot{\epsilon}_0/\dot{\epsilon})}. \tag{45}$$

From eq 4, which is obtained from the constant-stress creep test data, a similar constitutive equation can be derived.

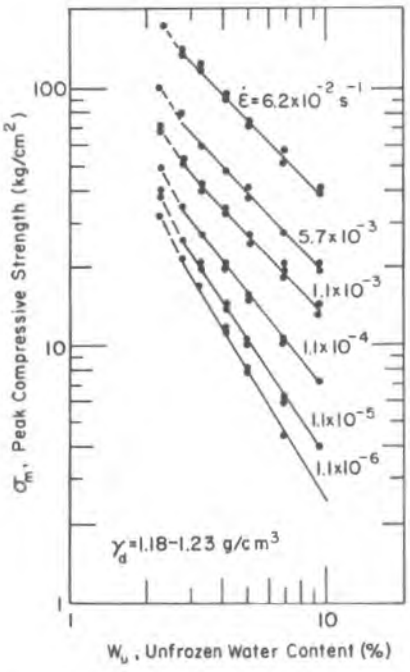

Figure 56. Log σ_m vs log W_u for various strain rates.

It is obvious from Figure 54 that the peak strength increases more rapidly as the temperature decreases below -7°C. From Figure A1, Appendix A, the unfrozen water content W_u (%) of the samples with medium dry density (corresponding to a water content of 40.5%) for various temperatures can be calculated by

$$W_u = 6.90(\theta/\theta_0)^{-0.47}. \tag{46}$$

Equation 46 was used to calculate values of W_u for the various testing temperatures shown in Figure 54 to produce Figure 56, using the same peak strength data. All of the curves in this graph also break at a W_u corresponding to -7°C. If the peak strength is evaluated in terms of unfrozen water content, a functional relationship similar to that relating the peak strength to temperature can be easily obtained.

The variation of peak strength with dry density for various strain rates at -2°C is shown in Figure 57. Under a relatively high strain rate, the peak strength remains almost constant over the test range of dry density of 1.07–1.43 g/cm^3 at -2°C. But under rela-

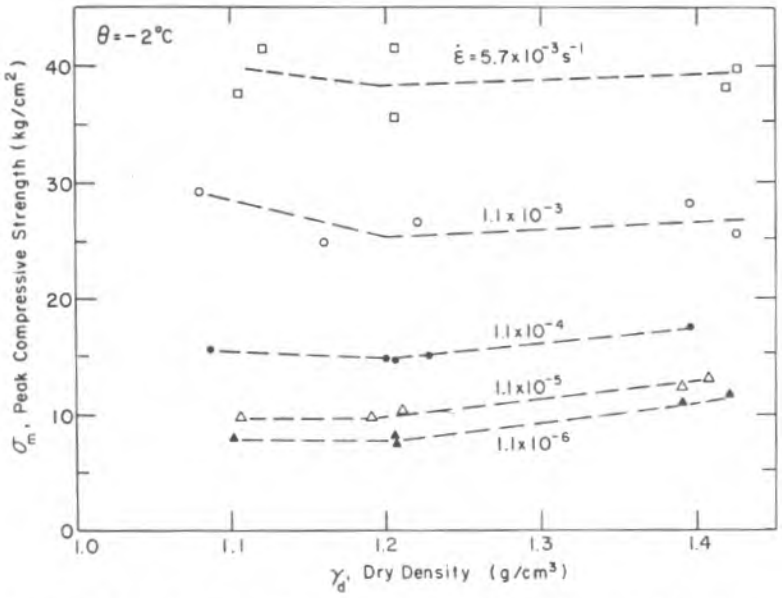

Figure 57. Peak strength as a function of dry density for various strain rates at -2°C.

tively low strain rates, the peak strength significantly increases with increasing dry density for the higher dry density range. For lower strain rates, there is enough time for the sample to mobilize its interparticle frictional resistance. The higher the dry density, the greater the frictional resistance, so the higher the peak strength.

Table 13 compares the peak strength of saturated and partially saturated samples of medium dry density. The peak strength of the partially saturated samples is about 7–20% less than that of saturated ones, even though the saturation degree (including ice and unfrozen water) for the partially saturated soil is only 3–4% less than for the saturated soil. This indicates that for a given density the saturation degree may significantly influence the peak strength of frozen silt.

Table 13. Peak strength of saturated and partially saturated samples with an average dry density of 1.2 g/cm³.

		σ_m (kg/cm²)	
θ (°C)	$\dot{\varepsilon}$ (s^{-1})	Partially saturated*	Saturated†
-1	1.2×10^{-3}	16.4	19.3
-1	1.2×10^{-4}	9.4	10.1
-2	1.2×10^{-3}	20.6	25.6
-2	1.2×10^{-4}	13.8	14.8
-3	1.2×10^{-4}	17.1	19.7
-3	1.2×10^{-6}	9.7	11.0

* Samples saturated under a normal air pressure, with an average saturation degree of about 96–97%.

† Average of a number of tested samples.

Initial yield strength

Figure 58 shows the relationship between the initial yield strength σ_y and the peak strength σ_m for various testing temperatures at dry densities ranging from 1.18 to 1.23 g/cm³. For a particular dry density there is a unique relationship between σ_y and σ_m, which for this investigation does not depend on temperature or strain rate. By linear regression analysis on the test data, it can be simply expressed by a linear equation:

$$\sigma_y = k\,\sigma_m + c. \tag{47}$$

For γ_d between 1.18 and 1.23 g/cm³, $k = 0.79$ and $c = -0.6$ kg/cm². Since the small value of c may result from the test error, it can be neglected. Thus, eq 47 can be written as

$$\sigma_y = k\,\sigma_m. \tag{48}$$

The initial yield strength vs peak strength for various dry densities is plotted in Figure 59. It indicates that the coefficient k in eq 48 depends significantly on dry density. Through a multiple linear regression analysis, it was found from the test data that the initial yield strength σ_y of frozen silt can be determined in terms of peak strength σ_m and dry density γ_d by the following equation (with $r^2 = 0.9865$ for 69 data points):

$$\sigma_y = 2.15\sigma_m - 1.15\gamma_d\sigma_m - 0.28 \tag{49}$$

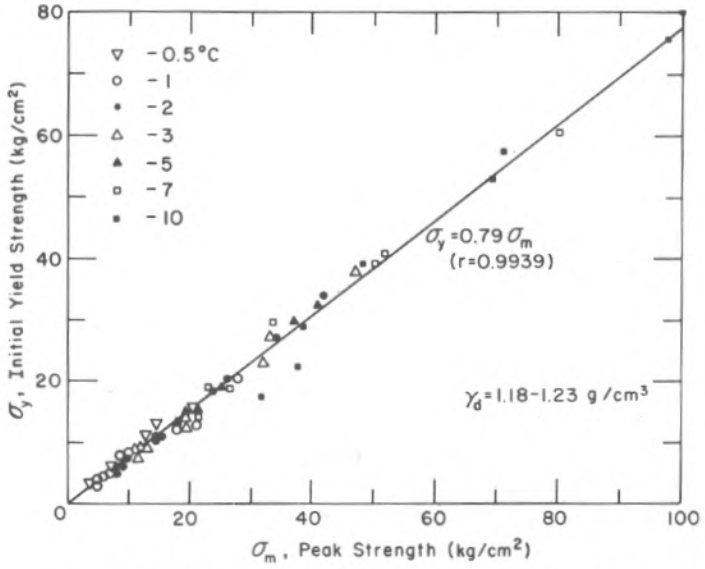

Figure 58. Relationship between σ_m and σ_y for the specimens with medium density at various temperatures.

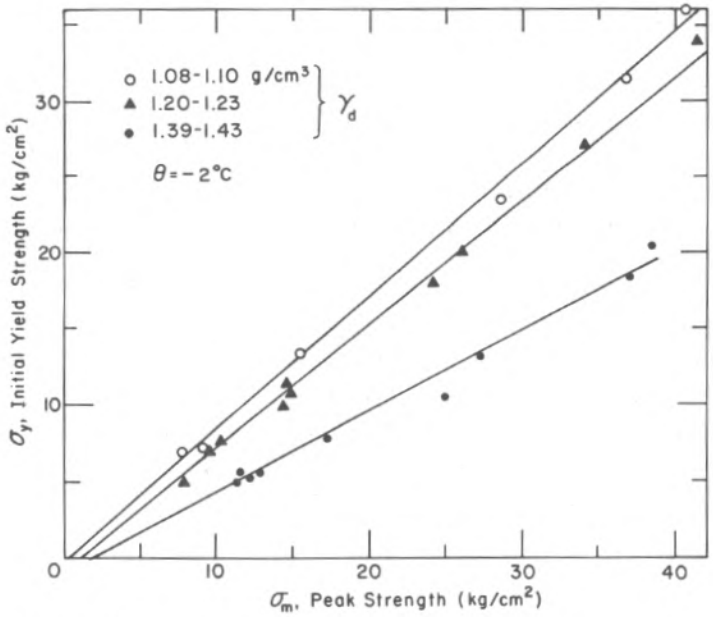

Figure 59. Relationship between σ_m and σ_y for various dry densities at -2°C.

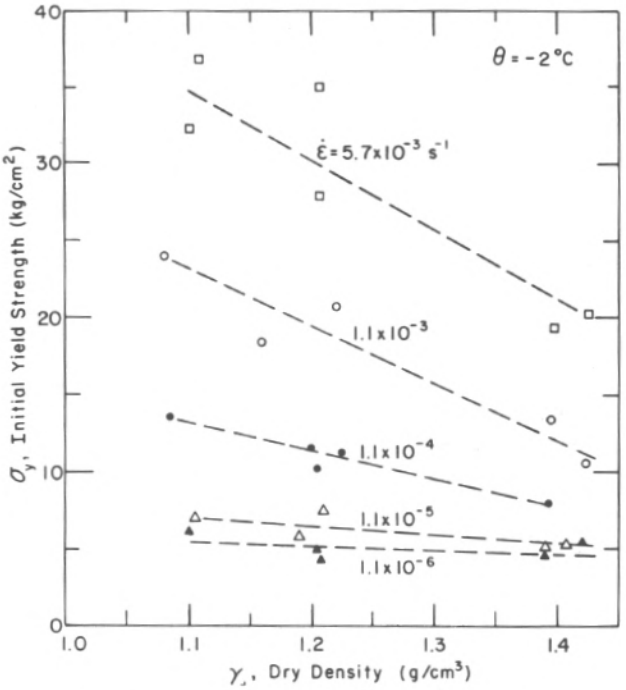

Figure 60. Initial yield strength as a function of dry density for various strain rates at -2°C.

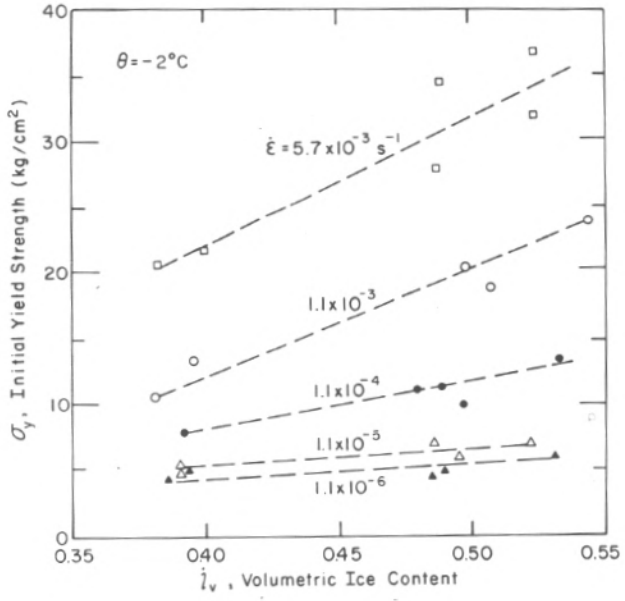

Figure 61. Initial yield strength as a function of volumetric ice content for various strain rates at -2°C.

where γ_d is in g/cm³ and σ_m is in kg/cm². Neglecting the third term on the right side of eq 49, we have the simple form of the equation:

$$\sigma_y = 2.15\sigma_m - 1.15\gamma_d\sigma_m \tag{50}$$

or

$$\sigma_y = (2.15 - 1.15\gamma_d)\sigma_m. \tag{51}$$

This equation indicates that the initial yield strength σ_y increases with decreasing dry density for the saturated frozen silt. This can be clearly seen from Figure 60, which presents the yield strength as a function of dry density for various strain rates at -2°C. The initial yield strength also increases with increasing volumetric ice content, as shown in Figure 61. Figures 60 and 61 also show that the initial yield strength is much less sensitive to dry density and ice content at low strain rates than at high strain rates at the test temperature. Again, this simply means that the initial yield strength relaxes much faster for ice-rich frozen soil than for dense frozen soil. Sayles and Carbee (1981) reported a similar observation for the same soil at a temperature of -1.67°C and strain rate of 5×10^{-3} s^{-1}. They interpreted this stress as being the stress at which the initial fracture of pore ice in frozen soil occurs. This conclusion was reached by referring to the stress-strain behavior of polycrystalline ice where the ice fractured at nearly the same strain (Hawkes and Mellor 1972).

Equation 50 also implies that the difference between σ_y and σ_m decreases with decreasing dry density. Figure 51 illustrates this trend. The peak strength is almost twice the yield strength for γ_d = 1.39 g/cm³, but there is no significant difference between them for γ_d = 1.10 g/cm³. For higher dry densities the fully mobilized frictional resistance between soil particles at a large failure strain accounts for a major part of the peak strength of the frozen soil. For lower dry densities, the strength of frozen soil is substantially governed by the ice matrix, which fails at a small strain of about 1% soon after its plastic yielding (Sayles and Carbee 1981).

Failure strain

Test results of failure strain ϵ_f at various temperatures and strain rates for medium-density samples are shown in Figure 62. Within a certain range of strain rate the failure strain does

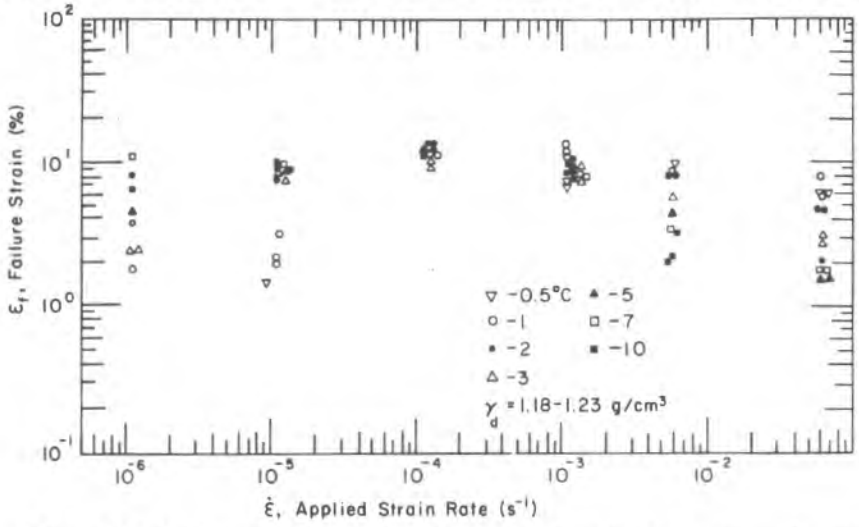

Figure 62. Failure strain as a function of strain rate for medium-density samples at various temperatures.

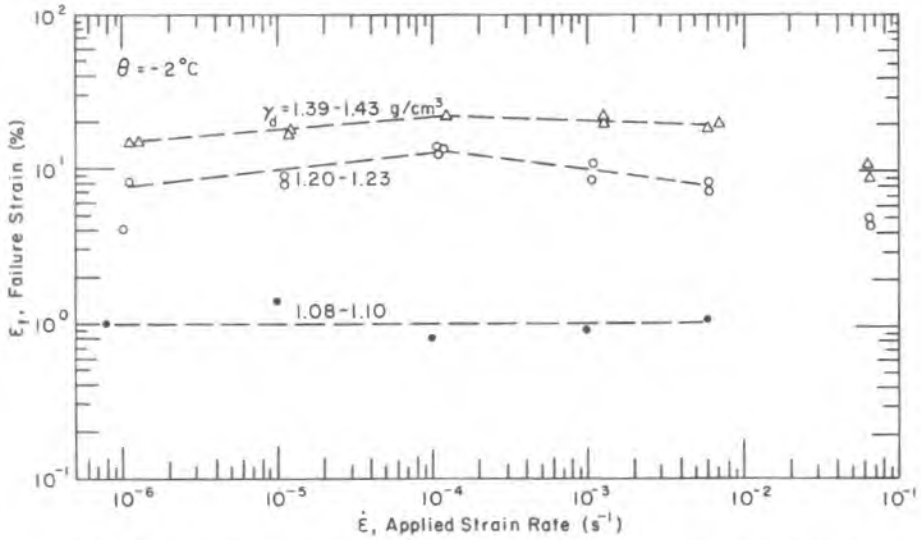

Figure 63. Variation of failure strain with strain rate for various dry densities at -2°C.

not depend on temperature, but it varies slightly with strain rate and has a maximum value at a moderate strain rate of about 10^{-4} s^{-1}. However, at relatively high and low strain rates, the failure strain apparently does depend on temperature. The decrease in failure strain at higher strain rates and lower temperatures indicates the transition of failure mode from ductile to brittle.

Figure 63 demonstrates the effect of dry density on failure strain at -2°C. Failure strain decreases greatly with decreasing dry density. For each density group, the failure strain is approximately constant within the strain rate range of about 10^{-6} to 6×10^{-3} s^{-1}. The average values of failure strain for various dry density groups are listed in Table 14 and plotted in Figure 47, showing a good agreement with the values from the creep tests discussed earlier.

Initial yield strain

The initial yield strain discussed here refers to the strain at the yield stress σ_y. Its variation with strain rate at various test temperatures for medium-density samples is shown in Figure 64. It appears that for a given dry density, initial yield strain ϵ_y significantly depends on strain rate but is almost independent of temperature. There is a break point in the ϵ_y vs $\ln\dot{\epsilon}$ curve: the initial yield strain increases exponentially with increasing strain rate when $\dot{\epsilon} > 10^{-5}$ s^{-1}, but it remains almost the same when $\dot{\epsilon} < 10^{-5}$ s^{-1}. The same observation was reported by Mellor and Cole (1982) for polycrystalline ice. This evidence strongly supports Sayles and Carbee's (1981) and our conclusion that the initial yielding of frozen silt can be substantially attributed to the initial fracture of the ice matrix. Based on Figure 64, initial yield strain as a function of strain rate for dry densities ranging from 1.18 to 1.23 g/cm³ can be expressed as

$$\epsilon_y = 0.27 + 0.045\ln(\dot{\epsilon}/10^{-5}) \quad \text{when } \dot{\epsilon} \geq 10^{-5}\text{ s}^{-1}$$
and
$$\epsilon_y = 0.27 \quad \text{when } \dot{\epsilon} < 10^{-5}\text{ s}^{-1} \qquad (52)$$

where ϵ_y is in percent.

Figure 65 shows the variation of the initial yield strain ϵ_y with strain rate for different dry densities at -2°C. There seems no sig-

Table 14. Average values of ϵ_f for frozen Fairbanks silt with different dry densities at -2°C.

γ_d (g/cm³)	ϵ_f*
1.08–1.10	0.0106
1.20–1.23	0.0913
1.39–1.43	0.1868

*From constant-strain-rate tests.

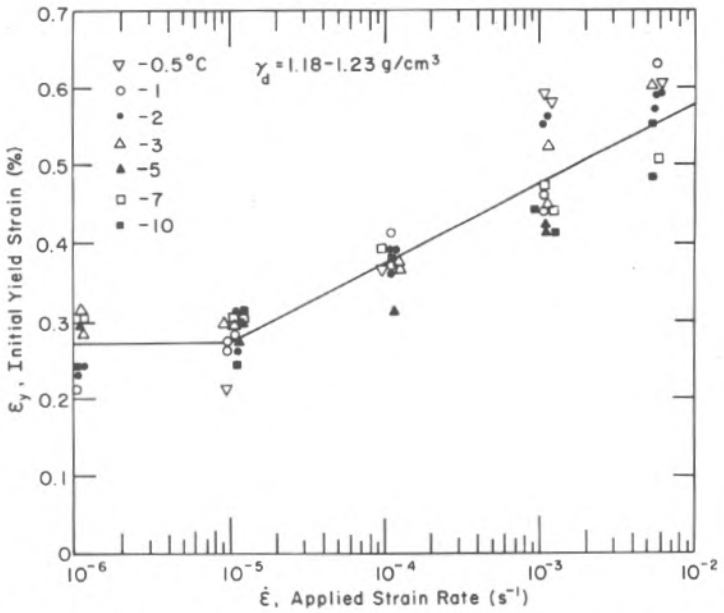

Figure 64. Initial yield strain as a function of strain rate at various temperature for medium-density samples.

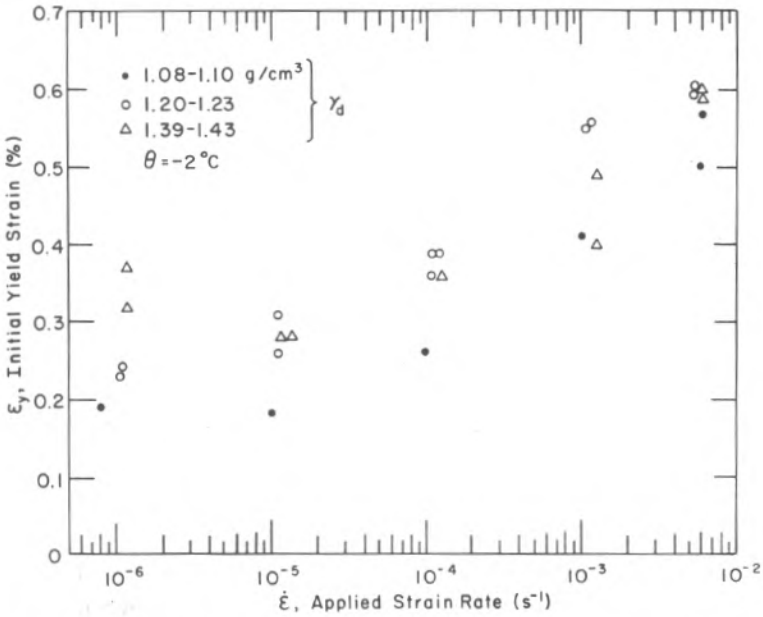

Figure 65. Initial yield strain as a function of strain rate for various dry densities at -2°C.

nificant difference of ϵ_y between medium and high densities. However, the values of ϵ_y for low-density samples appear to be slightly less than those described by eq 52. Its magnitude ranges from about 0.2% to 0.5% as strain rate increases from 8.1×10^{-7} to 5.6×10^{-3} s^{-1}, which is very close to that for polycrystalline ice (Hawkes and Mellor 1972, Mellor and Cole 1982).

Initial tangent modulus

The initial tangent modulus E_i as a function of temperature at various strain rates is shown in Figure 66. Using a multivariable regression analysis, we obtained the following equation

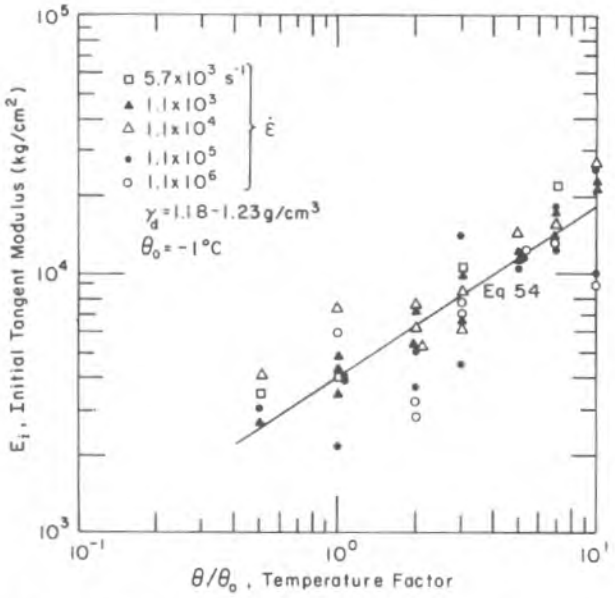

Figure 66. LogE_i vs log(θ/θ_0) for medium-density samples at various strain rates.

to describe the initial tangent modulus E_i as a function of temperature and strain rate for γ_d ranging from 1.18 to 1.23 g/cm³:

$$E_i = 6.1\times10^3(\theta/\theta_0)^{0.651}(\dot{\epsilon}/\dot{\epsilon}_1)^{0.046} \tag{53}$$

where E_i is in kg/cm², and $\dot{\epsilon}_1$ is a reference strain rate taken as 1 s⁻¹. The correlation coefficient is equal to 0.8899, and the standard error is 2.1×10^3 kg/cm².

It is obvious from eq 53 that the initial tangent modulus is much less sensitive to strain rate than to temperature. Similar results were reported by Hawkes and Mellor (1972) for polycrystalline ice and by Haynes et al. (1975) for frozen silt. It is therefore reasonable to consider that for a particular material the initial tangent modulus depends only on temperature and is independent of strain rate. Thus, eq 53 can be approximately written as (with r = 0.8690 and $s = 2.1\times10^3$ kg/cm² for 52 data points):

$$E_i = 4.0\times10^3(\theta/\theta_0)^{0.626}. \tag{54}$$

Figure 66 shows that the data on E_i are rather scattered. This scattering is believed to be due to the graphical determination of E_i and the lack of stress-strain data at the initial test period for higher strain rates. It is, therefore, essential to develop standard techniques for determining the initial tangent modulus and for precisely recording more stress-strain data for the fast constant-strain-rate tests.

The test results in Table 4 show that there is no significant difference in E_i between samples with medium and high densities for $\dot{\epsilon} > 10^{-5}$ s⁻¹ and θ = -2°C. But the values of E_i for low-density samples are considerably greater than those for medium-density samples. E_i increases from about 5×10^3 to 2×10^4 kg/cm² as the dry density decreases from about 1.23 to 1.08 g/cm³ at -2°C. This indicates that the initial tangent modulus of dense frozen silt can be considerably less than that of ice. According to Hawkes and Mellor (1972) the initial tangent modulus of fine-grained polycrystalline ice has a magnitude of 2.8×10^4 to 7.4×10^4 kg/cm² at -7°C. We have shown that the average value of E_i for frozen Fairbanks silt with an aver-

age dry density of 1.20 g/cm³ ranges from 1.3×10^4 to 2.2×10^4 kg/cm² at the same temperature.

Plas-Tech Corporation (1966) reported that the modulus values of Hanover silt at -9.4°C are from 6.2×10^3 to 1.7×10^4 kg/cm², which is close to that of the tested Fairbanks silt. Our test results of the initial tangent modulus are also similar to those reported by Haynes et al. (1975) under comparable conditions.

50% peak strength modulus

The variation of 50% peak strength modulus E_1 with temperature for various strain rates is plotted in Figure 67 for dry densities in the range of 1.20 to 1.23 g/cm³. The 50% strength modulus varies with both temperature and strain rate, and it can be evaluated by

$$E_1 = a(\dot{\varepsilon}/\dot{\varepsilon}_1)^b (\theta/\theta_0)^{n_1}. \tag{55}$$

A multiple linear regression analysis showed that the parameters in this equation have the values of $a = 7.6 \times 10^3$ kg/cm², $b = 0.122$, and $n_1 = 0.624$ with $r = 0.9447$ and $s = 1.1 \times 10^3$ kg/cm² for 54 data points.

The 50% strength modulus as a function of strain rate is shown in Figure 68 for different dry densities at -2°C. Dry density obviously has a significant influence on the 50% strength modulus. The curves in this plot are nearly parallel to each other, so parameter b in eq 55 is nearly independent of dry density at a temperature of -2°C. The coefficient a is the only parameter that determines the modulus dependence on dry density if the parameter n in this equation is also independent of dry density. Assuming that b does not depend on dry density for all test temperatures, we determined from the test data that $a = 9.3 \times 10^3$ kg/cm² when γ_d ranged from 1.08 to 1.10 g/cm³, and $a = 1.2 \times 10^3$ kg/cm³ when γ_d ranged from 1.39 to 1.43 g/cm³.

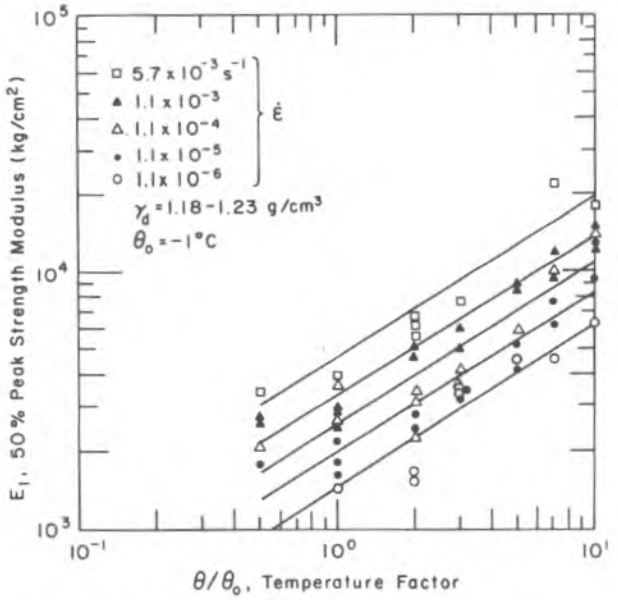

Figure 67. Log E_1 vs log(θ/θ_0) for medium-density samples at various strain rates.

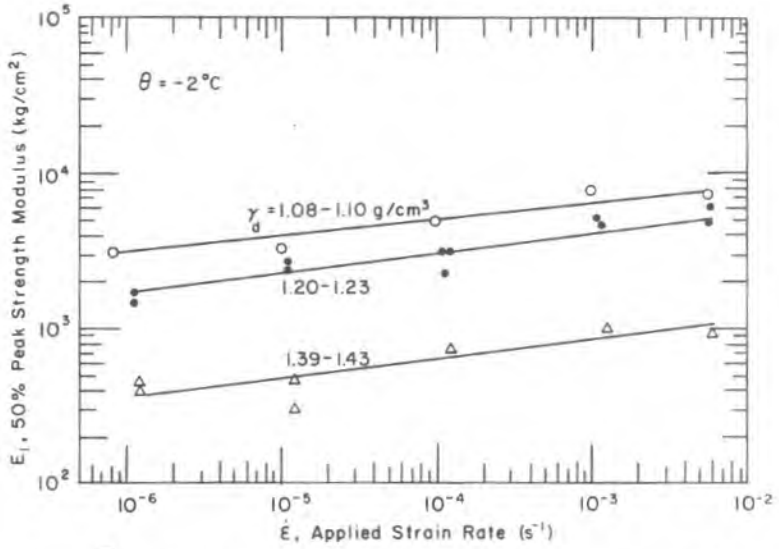

Figure 68. Log E_i *vs log* $\dot{\epsilon}$ *for various dry densities at -2°C.*

In eq 54 and 55 the values of the exponent n_i of (θ/θ_0) are nearly equal. If n_i is considered to be invariant, then combining these two equations results in the following approximate expression:

$$E_i = 0.54(\dot{\epsilon}/\dot{\epsilon}_i)^{-0.122} E_i \tag{56}$$

which can be used to estimate the initial tangent modulus of frozen silt according to its 50% strength modulus. This relation is helpful for determining E_i because E_i is easier to determine.

CORRESPONDENCE BETWEEN CONSTANT-STRESS TESTS AND CONSTANT-STRAIN-RATE TESTS

Mellor and Cole (1982) and Sego and Morgenstern* recently summarized some possible points of correspondence between constant-stress tests (creep tests) and constant-strain-rate tests (strength tests) on polycrystalline ice. Ladanyi (1981) reported that this correspondence is also valid for frozen soils. Our work shows that there is a correspondence between the results of these two types of tests on frozen silt. The results of the failure strain and σ_m (or σ) vs $\dot{\epsilon}$ (or $\dot{\epsilon}_m$) curve from these two types of tests are nearly the same. The former can be clearly seen in Figure 47, in which the failure strains from both the creep and the strength tests show a good correspondence when plotted vs dry density. The latter is shown in Figures 69 and 70, in which σ_m vs $\dot{\epsilon}$ from the strength tests and σ vs $\dot{\epsilon}_m$ from the creep tests are plotted together in a semi-log scale, showing a very good agreement within a wide overlap range of strain rate.

Because of the correspondence, one can use the constant-stress and constant-strain-rate test data equivalently to evaluate the time-dependent stress-strain behavior of frozen soils. In view of the difficulties in gaining creep test data at very high stresses and strength test data at very low strain rates, it might be appropriate to run creep tests at relatively low stresses and strength tests at relatively high strain rates, and then combine the results from the two types of tests to establish a "complete" σ–$\dot{\epsilon}$ curve. Figure 71 represents such a generalized σ–$\dot{\epsilon}$ curve in a semi-log scale for the frozen silt tested. For discussion purposes, this curve is di-

* Personal communication, University of Alberta, 1982.

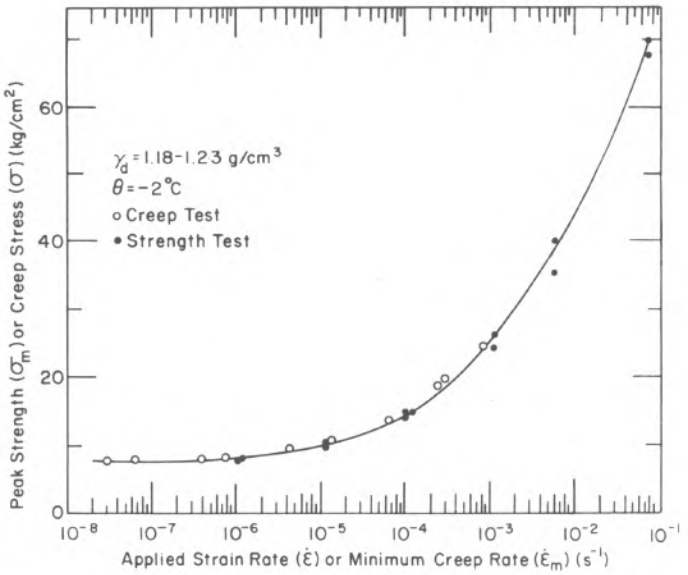

Figure 69. Log$\dot{\varepsilon}_m$ or log$\dot{\varepsilon}$ vs σ or σ_m for the frozen silt with medium density at -2°C.

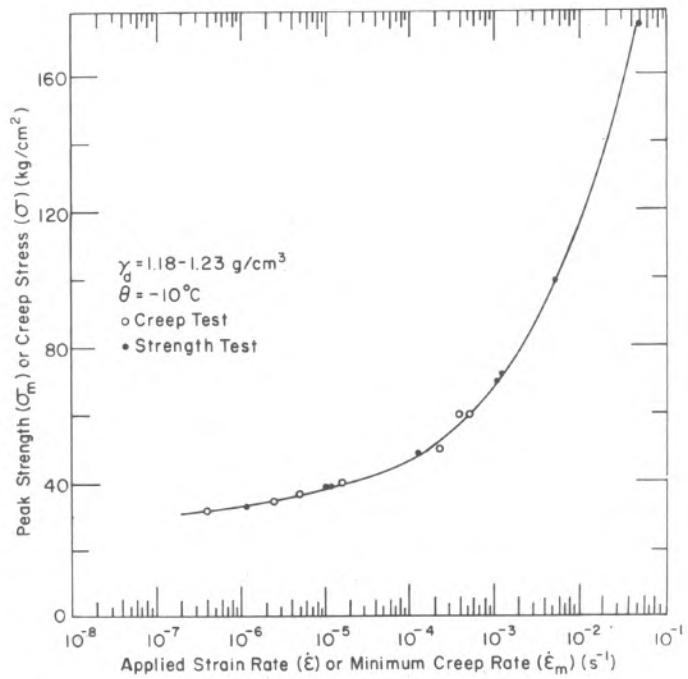

Figure 70. Log$\dot{\varepsilon}_m$ or log$\dot{\varepsilon}$ vs σ or σ_m curve for the frozen silt with medium density at -10°C.

vided into three sections by two characteristic strain rates, $\dot{\varepsilon}_c$ and $\dot{\varepsilon}_0$, corresponding to different deformation mechanisms. As discussed earlier, different constitutive equations should be used to describe the stress-strain behavior of frozen soil in accordance with different stress-temperature fields.

We could not get the upper limit of the σ-$\dot{\varepsilon}$ curve, that is, the limiting instantaneous strength (denoted as σ_{in} in Fig. 71), in this investigation because of the head-speed limit of the test machine. Many other researchers may also have this kind of problem. Therefore, it is

appropriate to define an identical instantaneous strength such that it corresponds to a certain strain rate. In the present study, instantaneous strength (denoted as σ_0) is defined as the peak strength for which $\dot{\epsilon} = 10^{-3}$ s^{-1}. Then, from eq 26 and 42 we obtain

$$\sigma_{lt} = 0.18(\theta/\theta_0)^{0.38}\sigma_0 \qquad (57)$$

which can be used for predicting the limiting long-term strength for saturated frozen Fairbanks silt with dry densities ranging from 1.18 to 1.23 g/cm^3.

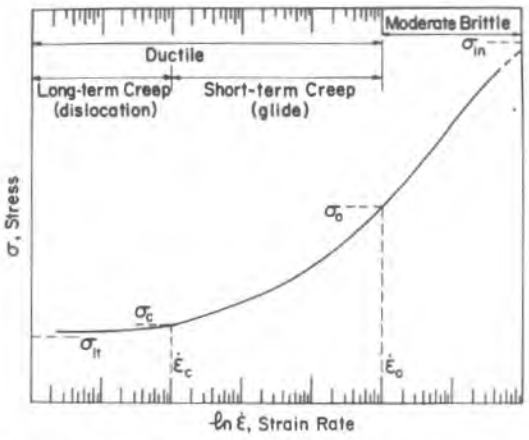

Figure 71. Generalized curve of log$\dot{\epsilon}$ vs σ.

CONCLUSIONS

The constant-stress and constant-strain-rate compression tests lead to the following conclusions.

There exists a critical creep strength σ_c, which can be used to classify the creep of frozen silt into two basic types: short-term creep for which $\sigma > \sigma_c$, and long-term creep for which $\sigma \leq \sigma_c$. Short-term creep is controlled by glide creep, while long-term creep is governed by dislocation creep. They obey different creep laws and thus different constitutive equations.

The rate process theory is applicable for frozen soil. However, the linear function, $U_e = \Delta F - \beta\sigma$, is not valid for the lower stress range. Instead, a power-law function, $U_e = \Delta F(1 + \sigma/\sigma_1)^{-\delta}$, works very well over a wide range of stresses. A free activation energy ΔF of about 8600 kcal/mole was obtained for frozen Fairbanks silt with medium dry density, which is much higher than that reported by other investigators.

Dry density has a significant effect on the creep behavior. The flow law of ice-rich frozen silt is similar to that of polycrystalline ice and can be described by a simple power law over a wide range of creep stresses. For the dense frozen silt, though, the closely packed soil particles greatly impede the creep process within secondary creep at lower stresses, so its creep law cannot be described by a single power law over a wide range of creep stress but requires more than one constitutive equation.

Different types of creep have different strength-loss equations. One cannot predict long-term strength by simply extrapolating the short-term creep data. The 100-year strength σ_{lt} of frozen Fairbanks silt with medium density can be determined by

$$\sigma_{lt} = 3.49(\theta/\theta_0)^{0.87} \qquad (58)$$

or

$$\sigma_{lt} = 0.18(\theta/\theta_0)^{0.38}\sigma_0 \qquad (59)$$

where σ_{lt} is in kg/cm^2 and σ_0 is the peak strength of the silt at $\dot{\epsilon} = 10^{-3}$ s^{-1}.

Failure strain ϵ_f does not seem to be sensitive to temperature within the accuracy of the test data, and it also is not sensitive to $\dot{\epsilon}_m$ for a particular failure mode or deformation mechanism. However, it is very sensitive to dry density. It increases proportionally from about 1% to 18% as dry density increases from 1.08 to 1.40 g/cm^3.

The creep failure criterion for this frozen soil can take the general form of $\dot{\epsilon}_m t_m^p = \epsilon_f$, where p depends only on dry density, and t_m is in minutes if p is not 1. For frozen Fairbanks silt, the values of p are given in Table 7.

Assur's (1980) creep model for ice can well describe the complete creep curve for ice-rich frozen silt as well as the short-term creep curve for dense frozen silt, but it cannot describe long-term creep as well. It considerably underestimates creep deformation during primary and tertiary creep for long-term creep.

The frozen Fairbanks silt samples generally failed in a ductile mode under the constant-strain-rate test conditions. But at very high strain rates and low temperatures, a moderate brittle failure may occur.

The compressive peak strength σ_m of the frozen silt is very sensitive to temperature and strain rate. Both A and m in the equation $\sigma_m = A(\theta/\theta_0)^m$ depend on the strain rate and temperature range. It has been found that for $\theta \geq -7°C$ both the $1/A$ vs $\ln\dot{\epsilon}$ and the m vs $\ln\dot{\epsilon}$ curves break at a strain rate of 1.1×10^{-3} s^{-1}, perhaps indicating the transition of failure mode from ductile to brittle.

For the material tested at -2°C, peak strength was found to be not sensitive to dry density at relatively high strain rates, but it decreases considerably with decreasing dry density at lower strain rates.

The initial yield strength σ_y is sensitive not only to temperature and strain rate, but also to dry density, indicating that it is essentially related to the initial fracture of pore ice in frozen soil. There is a definite relationship between σ_m and σ_y for the silt that is not dependent on temperature and strain rate:

$$\sigma_y = (2.15-1.15\gamma_d)\sigma_m. \tag{60}$$

For a certain range of applied strain rates, the failure strain of the silt does not vary with temperature, but it depends strongly on dry density. For the saturated frozen Fairbanks silt, failure strain decreases from 18.7% to 1% as dry density decreases from about 1.40 to 1.08 g/cm^3 over a range of applied strain rates from 1.1×10^{-6} to 1.1×10^{-3} s^{-1}.

The initial yield strain of the frozen silt does not depend on temperature but increases with increasing strain rate when $\dot{\epsilon} \geq 10^{-3}$ s^{-1}. When $\dot{\epsilon} < 10^{-3}$ s^{-1}, it remains almost constant. It decreases slightly with decreasing dry density. For the samples with low dry unit weight, it has a magnitude of 0.2–0.5% over a strain rate range of 1.1×10^{-3} to 1.1×10^{-6} s^{-1}.

The initial tangent modulus E_i of the frozen silt is not sensitive to strain rate in the range of ratios used, but it varies with temperature. The value of E_i for the tested silt with γ_d ranging from 1.18 to 1.23 g/cm^3 can be determined (in kg/cm^2) by

$$E_i = 4.0\times10^3(\theta/\theta_0)^{0.636}. \tag{61}$$

The 50% peak strength modulus E_1 of the silt as a function of temperature, strain rate and dry density can be expressed as

$$E_1 = a(\dot{\epsilon}/\dot{\epsilon}_1)^b(\theta/\theta_0)^n \tag{62}$$

where $b = 0.122$, $n = 0.624$, and a depends on dry density as follows:

γ_d (g/cm^3)	a (kg/cm^2)
1.08–1.10	9.3×10^3
1.20–1.23	7.6×10^3
1.39–1.43	1.2×10^3

The initial tangent modulus E_i and the 50% strength modulus E_1 can be related to each other by

$$E_i = 0.54(\dot{\epsilon}/\dot{\epsilon}_1)^{-0.122} E_1. \tag{63}$$

There is a correspondence between the constant-stress and constant-strain-rate tests for the frozen silt under the test conditions in this study. In particular, the average failure strains over a certain range of $\dot{\epsilon}$ (or $\dot{\epsilon}_m$) from the two types of tests are approximately the same, and the σ_m–$\dot{\epsilon}$ curves from the strength tests and the σ–$\dot{\epsilon}_m$ curves from the creep tests are in good agreement.

Creep tests at a relatively low stress and strength tests at a relatively high strain rate can be used to yield a complete σ–$\dot{\epsilon}$ curve for a soil.

LITERATURE CITED

Akili, W. (1966) Stress effect on creep rates of a frozen clay soil from the standpoint of rate process theory. Ph.D. thesis, Michigan State University.

Akili, W. (1970) On the stress-creep relationship for a frozen clay soil. *Materials Research and Standards,* **10:** 16–22.

Andersland, O.B. and W. Akili (1967) Stress effect on creep rates of a frozen clay soil. *Geotechnique,* **17**(1): 27–39.

Andersland, O.B. and W. Douglas (1970) Soil deformation rates and activation energies. *Geotechnique,* **20**(1): 1–16.

Arctic Construction and Frost Effects Laboratory (1952) Investigation of description, classification and strength properties of frozen soils. Vol. 1 and 2. USA Arctic Construction and Frost Effects Laboratory (ACFEL), Technical Report 40. AD721745 and AD 721746.

Assur, A. (1980) Some promising trends in ice mechanics. In *Physics and Mechanics of Ice.* Berlin: Springer-Verlag, pp. 1–15.

Cox, G.F.N., J.A. Richter, W.F. Weeks, M. Mellor and H.W. Bosworth (1984) The mechanical properties of multi-year sea ice. Phase I: Test results. USA Cold Regions Research and Engineering Laboratory, CRREL Report 84-9.

Fish, A.M. (1979) Mechanical properties of frozen soils. Research Proposal, contract no. DAAR 29-77-0016, part B, Massachusetts Institute of Technology.

Fish, A.M. (1980) Kinetic nature of the long-term strength of frozen soils. In *Proceedings of the Second International Symposium on Ground Freezing.* Trondheim: Norwegian Institute of Technology, pp. 95–108.

Glen, J.W. (1955) The creep of polycrystalline ice. *Proceedings, Royal Society of London,* **A228:** 519–538.

Gold, L.W. (1973) Activation energy for creep of columnar-grained ice. In *Physics and Chemistry of Ice.* Toronto: University of Toronto Press, pp. 362–364.

Goughnour, R.R. (1967) The soil-ice system and the shear strength of frozen soils. Ph.D. thesis, Michigan State University.

Goughnour, R.R. and O.B. Andersland (1968) Mechanical properties of a sand-ice system. *ASCE Journal of the Soil Mechanics and Foundations Division,* **94**(SM4): 923–950.

Hawkes, I. and M. Mellor (1972) Deformation and fracture of ice under uniaxial stress. *Journal of Glaciology,* **11**(61): 103–131.

Haynes, F.D. and J.A. Karalius (1977) Effect of temperature on the strength of frozen silt. USA Cold Regions Research and Engineering Laboratory, CRREL Report 77-3.

Haynes, F.D., J.A. Karalius and J. Kalafut (1975) Strain rate effect on the strength of frozen silt. USA Cold Regions Research and Engineering Laboratory, Research Report 350.
Homer, D.R. and J.W. Glen (1978) The creep activation energies of ice. *Journal of Glaciology,* **21**(85): 429–444.
Hult, J.A.H. (1966) *Creep in Engineering Structures.* Waltham, Mass.: Blaisdell Publishing Company.
Ladanyi, B. (1972) An engineering theory of creep of frozen soils. *Canadian Geotechnical Journal,* 9(63): 63–80.
Ladanyi, B. (1981) Mechanical behavior of frozen soils. In *Proceedings of the International Symposium on the Mechanical Behavior of Structured Media, Ottawa, May 18–21.* Amsterdam: Elsevier Scientific Publishing Company.
Langdon, T.G. (1973) Creep mechanisms in ice. In *Physics and Chemistry of Ice.* Toronto: University of Toronto Press, pp. 356–361.
Martin, R.T., J.M. Ting and C.C. Ladd (1981) Creep behavior of frozen sand. Final report, Part I. Massachusetts Institute of Technology.
McRoberts, E.C., T.C. Law and T.K. Murray (1978) Creep tests on undisturbed ice-rich silt. In *Proceedings of the Third International Conference on Permafrost, July 10–13, 1978, Edmonton, Alberta, Canada.* Vol. 1. Ottawa: National Research Council of Canada, pp. 539–545.
Mellor, M. (1980) Mechanical properties of polycrystalline ice. In *Physics and Mechanics of Ice.* Berlin: Springer-Verlag, pp. 217–245.
Mellor, M. and D.M. Cole (1982) Deformation and failure of ice under constant stress or constant strain-rate. *Cold Regions Science and Technology,* **5**: 201–219.
Mitchell, J.K., R.G. Campanella and A. Singh (1968) Soil creep as a rate process. *ASCE Journal of the Soil Mechanics and Foundations Division,* **94**: 231–253.
Mitchell, J.K. (1976) *Fundamentals of Soil Behavior.* New York: J. Wiley and Sons.
Plas-Tech Corporation (1966) Interim report on the compressive testing of two frozen soils versus strain rate at 15°F. USA Cold Regions Research and Engineering Laboratory, Project R-351.
Sanger, F.J. and C.W. Kaplar (1963) Plastic deformation of frozen soils in unconfined compression. In *Proceedings of First International Conference on Permafrost.* Building Research Advisory Board, National Academy of Sciences, Publication 1287.
Sayles, F.H. (1968) The creep of frozen sand. USA Cold Regions Research and Engineering Laboratory, Technical Report 190.
Sayles, F.H. (1973) Triaxial and creep tests on frozen Ottawa sand. In *Permafrost: North American Contribution to the Second International Conference.* Washington, D.C.: National Academy of Sciences, pp. 384–391.
Sayles, F.H. and D. Haines (1974) Creep of frozen silt and clay. USA Cold Regions Research and Engineering Laboratory, Technical Report 252.
Sayles, F.H. and D.L. Carbee (1981) Strength of frozen silt as a function of ice content and dry unit weight. *Engineering Geology,* **18**: 55–66.
Ting, J.M. (1981) The creep of frozen sands—qualitative and quantitative models. Final report, Part II. Massachusetts Institute of Technology.
Ting, J.M., R.T. Martin and C.C. Ladd (1983) Mechanisms of strength for frozen sand. *Journal of Geotechnical Engineering,* **109**(10): 1286–1302.
Tsytovich, N.A. (1930) Permafrost as a base for structures. Materials of the Permanent Commission for the Study of the Natural Productive Forces of the U.S.S.R., No. 80. U.S.S.R. Academy of Sciences Press.
Tsytovich, N.A. (1952) *Principles of the Mechanics of Frozen Soils.* U.S.S.R. Academy of Sciences Press.

Tsytovich, N.A. (1954) Instructions for determining the cohesive strength of frozen soil. USA Cold Regions Research and Engineering Laboratory, Draft Translation 162. AD 715072.

Tsytovich, N.A. (1958) Bases and foundations on frozen soil. Highway Research Board Translation, Special Report 58.

Tsytovich, N.A. and M.I. Sumgin (1937) *Fundamentals of the Mechanics of Frozen Ground.* U.S.S.R. Academy of Sciences Press.

Vialov, S.S. (1959) Rheological properties and bearing capacity of frozen soils. USA Snow, Ice and Permafrost Research Establishment, Translation 74. AD 48156.

Vialov, S.S. (1962) Strength and creep of frozen soils and calculations in ice-soil retaining structures. USA Cold Regions Research and Engineering Laboratory, Translation 76. AD 484093.

Vialov, S.S. (1963) Rheology of frozen soil. In *Proceedings of First International Advisory Board.* National Academy of Sciences, Publication 1287.

Vialov, S.S. (1973) Long-term rupture of frozen soil as a thermally activated process. In *Permafrost, U.S.S.R. Contribution to the Second International Conference.* pp. 222–228.

Weertman, J. (1973) Creep of ice. In *Physics and Chemistry of Ice.* Toronto: University of Toronto Press, pp. 320–337.

Wu Ziwang, Zhang Jiayi and Zhu Yuanlin (1982) Experimental research on rheology of frozen soils. In *Proceedings of China National Symposium on Glaciology and Cryopedology, Lanzhou.* China Science Publishing House.

Zhu Yuanlin, Liu Yongzhi and Xian Xiande (1982) Field creep tests on massive ground ice with soil. In *Proceedings of China National Symposium on Glaciology and Cryopedology, Lanzhou.* China Science Publishing House.

Zhu Yuanlin and D.L. Carbee (1983) Constant stress and constant strain rate compression test data of frozen Fairbanks silt. USA Cold Regions Research and Engineering Laboratory, Internal Report 839 (unpublished).

APPENDIX A: UNFROZEN WATER CONTENT DATA

Table A1. Unfrozen water content data for the samples with three typical water contents. The data are plotted in Figure A1.

W = 30.3%*		W = 40.5%†		W = 49.9%†	
Temperature θ, °C	Unfrozen water content W_u, %	Temperature θ, °C	Unfrozen water content W_u, %	Temperature θ, °C	Unfrozen water content W_u, %
-15.55	3.06	-18.45	1.90	-18.50	2.17
-14.12	3.18	-15.44	1.98	-15.57	2.21
-10.85	3.13	-13.15	2.06	-13.39	2.23
-8.95	3.48	-11.06	2.13	-11.09	2.26
-6.86	3.55	-8.40	2.53	-8.48	2.71
-4.96	4.13	-7.36	2.27	-7.44	2.80
-3.86	4.43	-6.15	2.80	-6.09	3.03
-2.62	4.90	-4.43	3.19	4.51	3.56
-1.76	5.55	-3.62	3.65	-3.52	3.86
-1.48	6.42	-2.36	4.31	-2.44	4.54
-1.06	7.83	-1.40	6.25	-1.61	5.57
-0.88	7.95	-0.82	6.78	-0.82	6.90
-0.54	8.12	-0.30	13.77	-0.28	13.85
-0.51	8.53				
-0.38	9.64				
-0.33	11.86				
-0.28	16.31				

* After Tice (personal communication).
† After Xu (personal communication).

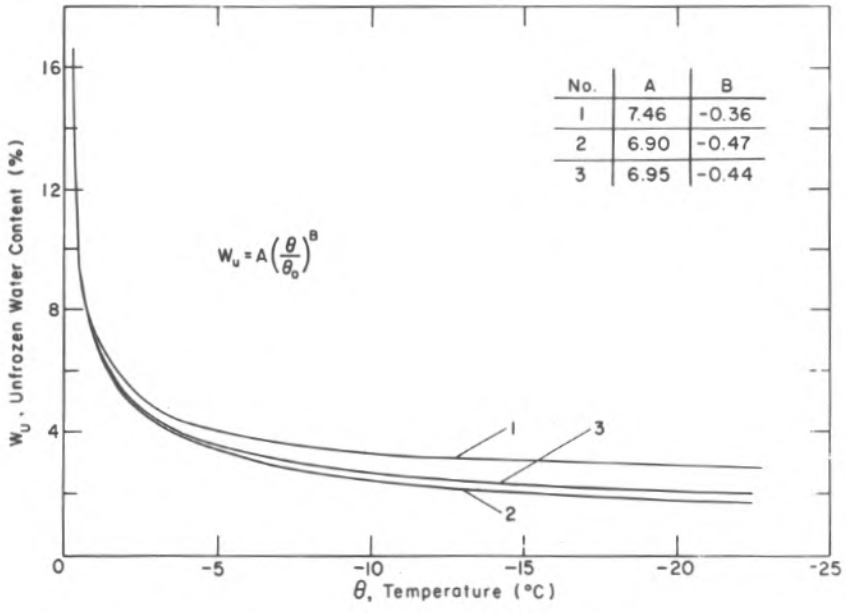

Figure A1. Unfrozen water content as a function of temperature: 1) w = 30.3% (Tice, pers. comm.); 2) w = 40.5%, and 3) w = 49.9% (Xu, pers. comm.).

APPENDIX B: PHYSICAL PROPERTIES OF SAMPLES TESTED

Sample No.	Water content w (%)	Dry density γ_d (g/cm^3)	Volume ice content† i_v	Saturation degree** s (%)	Void ratio e	Porosity n
1-1	42.7	1.191	0.513	99.1	1.251	0.556
1-2	44.1	1.174	0.523	99.9	1.282	0.562
1-3	42.9	1.189	0.514	99.5	1.254	0.556
1-4	43.2	1.184	0.516	99.5	1.262	0.558
1-5	44.7	1.166	0.527	100.0	1.298	0.565
1-6	43.9	1.177	0.522	100.0	1.276	0.561
1-7	42.8	1.179	0.509	98.4	1.272	0.560
1-8	43.4	1.182	0.518	99.8	1.265	0.559
1-9	44.0	1.173	0.521	99.4	1.285	0.562
1-10	43.1	1.187	0.516	99.6	1.257	0.557
1-11	47.7	1.120	0.498	98.8	1.394	0.582
1-12	43.3	1.185	0.470	99.0	1.261	0.558
1-13	44.5	1.174	0.481	100.0	1.281	0.562
1-14	43.4	1.181	0.470	98.8	1.270	0.559
1-15	44.8	1.160	0.479	99.1	1.311	0.567
1-16	43.5	1.183	0.472	99.0	1.266	0.559
1-17	45.0	1.160	0.482	99.2	1.309	0.567
2-18	42.1	1.199	0.460	98.6	1.235	0.552
2-19	44.2	1.170	0.476	99.1	1.291	0.563
2-20	42.1	1.200	0.461	99.0	1.234	0.552
2-21	41.6	1.206	0.456	99.2	1.200	0.550
2-22	42.6	1.200	0.467	99.6	1.234	0.552
2-23	42.0	1.206	0.487	99.5	1.222	0.550
2-24	42.5	1.198	0.490	99.5	1.236	0.553
2-25	42.9	1.190	0.492	99.8	1.250	0.556
2-26	43.3	1.185	0.495	99.3	1.262	0.558
2-27	42.2	1.205	0.464	99.6	1.222	0.550
2-28	41.7	1.211	0.460	99.6	1.213	0.548
2-29	42.8	1.195	0.468	99.5	1.240	0.554
2-30	42.2	1.203	0.463	99.2	1.228	0.551
2-31	43.5	1.185	0.473	99.4	1.261	0.558
2-32	42.6	1.198	0.466	99.4	1.237	0.553
2-33	42.7	1.187	0.463	99.4	1.257	0.557
2-34	43.2	1.189	0.495	99.9	1.253	0.556
3-35	43.0	1.194	0.470	99.5	1.246	0.555
3-36	42.8	1.206	0.497	100.0	1.221	0.550
3-37	41.3	1.210	0.479	99.8	1.215	0.548
3-38	43.6	1.183	0.498	99.8	1.266	0.559
3-39	41.3	1.219	0.483	99.9	1.198	0.545
3-40	40.8	1.227	0.479	99.9	1.184	0.542
3-41	42.4	1.206	0.489	100.0	1.221	0.550
3-42	41.7	1.213	0.485	99.9	1.210	0.548
3-43	41.3	1.219	0.494	100.0	1.198	0.545
3-44	41.2	1.221	0.494	100.0	1.195	0.545
3-45	41.5	1.216	0.496	100.0	1.204	0.546
3-46	41.9	1.208	0.498	99.8	1.219	0.549
3-47	41.5	1.216	0.496	100.0	1.204	0.546
3-48	42.4	1.198	0.500	99.7	1.235	0.552
3-49	41.8	1.208	0.485	99.7	1.217	0.549
3-62	41.8	1.210	0.486	99.5	1.216	0.549
4-50	42.3	1.200	0.488	99.6	1.232	0.552
4-51	45.4	1.155	0.509	99.7	1.320	0.569
5-52	40.9	1.200	0.481	96.2	1.232	0.552

Sample No.	Water content w (%)	Dry density γ_d (g/cm^3)	Volume ice content† i_v	Saturation degree** s (%)	Void ratio e	Porosity n
5-53	44.2	1.162	0.508	98.1	1.307	0.567
5-54	40.9	1.200	0.470	96.0	1.233	0.552
5-55	43.0	1.191	0.494	96.2	1.251	0.556
5-56	40.7	1.205	0.469	96.2	1.224	0.550
5-57	42.0	1.186	0.454	96.0	1.261	0.558
5-58	40.2	1.212	0.440	95.7	1.211	0.548
3-59	41.9	1.202	0.459	99.5	1.230	0.552
4-60	43.5	1.182	0.472	99.6	1.265	0.558
4-61	42.4	1.200	0.465	99.2	1.234	0.552
5-63	41.3	1.192	0.447	95.5	1.247	0.555
5-64	41.6	1.191	0.451	95.9	1.252	0.556
5-65	41.2	1.196	0.447	95.5	1.242	0.554
5-66	40.7	1.200	0.442	95.3	1.232	0.552
5-67	41.2	1.196	0.472	96.1	1.243	0.554
5-68	41.2	1.197	0.473	96.2	1.238	0.553
4-69	43.1	1.182	0.467	98.5	1.265	0.559
4-70	43.8	1.181	0.500	100.0	1.269	0.559
4-71	42.2	1.203	0.500	99.8	1.228	0.551
4-72	43.4	1.184	0.507	99.7	1.262	0.558
4-73	41.5	1.214	0.495	99.7	1.207	0.547
4-74	42.0	1.205	0.498	99.7	1.225	0.551
4-75	43.2	1.189	0.495	99.8	1.254	0.556
4-76	41.6	1.210	0.495	100.0	1.215	0.549
4-77	42.0	1.195	0.494	98.0	1.242	0.554
5-78	41.2	1.199	0.473	96.3	1.237	0.553
5-79	40.5	1.205	0.466	95.7	1.225	0.550
4-80	41.8	1.206	0.496	99.3	1.220	0.550
4-81	45.2	1.173	0.525	100.0	1.285	0.562
5-82	41.9	1.186	0.418	95.3	1.261	0.558
4-83	46.0	1.144	0.522	99.5	1.343	0.573
5-84	40.9	1.200	0.410	95.2	1.233	0.552
5-85	42.7	1.175	0.425	95.7	1.281	0.562
6-86	40.0	1.240	0.412	99.0	1.162	0.537
6-87	40.9	1.227	0.419	99.8	1.183	0.542
6-88	41.6	1.214	0.424	99.6	1.206	0.547
6-89	42.0	1.210	0.428	99.5	1.214	0.548
6-90	41.1	1.222	0.456	99.4	1.193	0.544
6-91	40.4	1.229	0.449	99.0	1.179	0.541
6-92	40.8	1.224	0.452	99.2	1.188	0.543
6-93	41.9	1.206	0.425	98.6	1.220	0.549
6-94	41.3	1.219	0.457	99.4	1.198	0.545
6-95	41.5	1.214	0.423	99.0	1.206	0.547
6-96	40.2	1.237	0.475	99.8	1.166	0.538
6-97	40.6	1.230	0.478	99.7	1.179	0.541
6-98	40.1	1.238	0.412	99.0	1.164	0.538
6-99	42.7	1.203	0.506	100.0	1.227	0.551
6-100	41.8	1.214	0.499	100.0	1.207	0.547
6-101	40.9	1.226	0.504	100.0	1.186	0.542
7-102	41.4	1.213	0.505	99.6	1.209	0.547
7-103	42.1	1.205	0.511	99.8	1.224	0.550
7-104	41.5	1.214	0.513	100.0	1.207	0.547
7-105	40.2	1.222	0.493	98.4	1.191	0.544
7-106	41.0	1.218	0.508	99.3	1.201	0.546
7-107	42.2	1.197	0.515	99.2	1.239	0.553
7-108	40.6	1.214	0.495	98.6	1.207	0.547
7-109	41.4	1.190	0.501	99.1	1.250	0.556
7-110	40.9	1.221	0.501	99.5	1.194	0.544

Sample No.	Water content w (%)	Dry density γ_d (g/cm^3)	Volume ice content† i_v	Saturation degree** s (%)	Void ratio e	Porosity n
7-111	40.5	1.214	0.500	98.7	1.205	0.546
7-112	41.2	1.216	0.510	99.4	1.204	0.546
7-113	40.6	1.221	0.509	98.8	1.195	0.544
7-114	41.2	1.208	0.512	98.3	1.219	0.549
7-115	40.2	1.227	0.507	98.8	1.183	0.542
7-116	41.6	1.182	0.506	98.8	1.265	0.559
7-117	41.0	1.218	0.513	99.5	1.201	0.546
7-118	41.7	1.210	0.519	99.9	1.215	0.549
8-119	45.9	1.168	0.555	100.0	1.295	0.564
8-120	41.8	1.210	0.521	100.0	1.214	0.548
8-121	42.6	1.198	0.526	100.0	1.236	0.553
8-122	43.7	1.179	0.532	100.0	1.272	0.560
8-123	42.3	1.202	0.524	100.0	1.229	0.552
8-124	42.4	1.202	0.520	100.0	1.231	0.552
8-125	42.3	1.203	0.519	100.0	1.227	0.551
8-126	43.3	1.174	0.519	99.8	1.282	0.562
8-127	41.4	1.211	0.510	99.6	1.211	0.548
8-128	43.1	1.187	0.522	99.6	1.257	0.557
8-129	40.7	1.222	0.506	99.4	1.190	0.543
8-130	43.1	1.184	0.515	99.4	1.262	0.558
8-131	42.5	1.195	0.512	99.5	1.241	0.554
8-132	40.6	1.229	0.501	100.0	1.181	0.541
8-133	42.0	1.203	0.508	99.5	1.226	0.551
8-134	41.4	1.221	0.508	99.7	1.195	0.544
8-135	42.0	1.211	0.512	100.0	1.212	0.548
9-136	43.0	1.190	0.516	99.8	1.252	0.556
9-137	43.5	1.182	0.531	100.0	1.267	0.559
9-138	44.2	1.168	0.522	99.2	1.293	0.564
9-139	44.6	1.165	0.532	99.7	1.301	0.565
9-140	41.7	1.206	0.494	100.0	1.221	0.550
9-141	44.2	1.171	0.501	99.4	1.289	0.563
9-142	42.9	1.187	0.502	100.0	1.257	0.557
9-143	42.0	1.190	0.492	97.8	1.250	0.556
9-144	42.8	1.195	0.504	100.0	1.241	0.554
9-145	44.2	1.200	0.513	100.0	1.039	0.510
9-146	41.6	1.200	0.479	97.3	1.233	0.552
9-147	44.0	1.173	0.499	98.9	1.283	0.562
9-148	43.3	1.182	0.435	99.2	1.265	0.558
9-149	43.0	1.177	0.429	97.0	1.275	0.560
9-150	42.9	1.205	0.473	100.0	1.223	0.550
9-151	43.6	1.184	0.440	99.1	1.263	0.558
9-152	43.6	1.179	0.438	98.3	1.272	0.560
10-153	45.2	1.155	0.449	98.3	1.321	0.569
10-154	47.8	1.123	0.468	99.0	1.385	0.581
10-155	44.4	1.163	0.522	100.0	1.304	0.506
10-156	45.2	1.155	0.529	99.6	1.320	0.569
10-157	49.6	1.096	0.533	99.4	1.444	0.591
10-158	49.8	1.091	0.533	99.0	1.457	0.593
10-159	49.8	1.085	0.530	98.9	1.472	0.595
10-160	50.1	1.088	0.535	99.1	1.462	0.594
10-161	48.8	1.105	0.528	99.1	1.424	0.588
10-162	49.3	1.099	0.531	99.1	1.439	0.590
10-163	50.8	1.070	0.534	98.1	1.505	0.601
10-164	49.8	1.086	0.531	98.2	1.468	0.595
10-165	48.5	1.104	0.524	98.4	1.425	0.588
10-166	51.2	1.080	0.544	100.0	1.480	0.597

Sample No.	Water content w (%)	Dry density γ_d (g/cm^3)	Volume ice content† i_v	Saturation degree** s (%)	Void ratio e	Porosity n
10-167	50.0	1.086	0.533	98.8	1.465	0.594
10-168	50.0	1.083	0.531	98.3	1.473	0.596
10-169	48.3	1.104	0.521	98.1	1.424	0.587
11-170	44.1	1.171	0.528	99.4	1.289	0.563
11-171	44.5	1.166	0.531	99.8	1.296	0.564
11-172	43.3	1.181	0.522	99.3	1.269	0.559
11-175	44.4	1.166	0.535	99.7	1.298	0.565
11-176	45.6	1.147	0.541	99.5	1.334	0.572
11-177	44.3	1.171	0.536	100.0	1.287	0.563
11-178	45.6	1.155	0.545	100.0	1.320	0.569
11-179	44.5	1.171	0.538	100.0	1.289	0.563
11-180	45.2	1.160	0.542	100.0	1.310	0.567
11-181	44.3	1.168	0.501	99.4	1.294	0.564
11-182	44.7	1.161	0.479	99.0	1.306	0.566
11-183	47.8	1.131	0.528	99.4	1.394	0.582
11-184	43.9	1.177	0.441	99.0	1.274	0.560
11-185	47.7	1.120	0.522	99.4	1.393	0.582
12-186	31.5	1.397	0.392	99.3	0.918	0.479
12-187	30.9	1.410	0.386	99.4	0.899	0.474
12-188	30.3	1.426	0.381	99.5	0.879	0.468
12-189	30.3	1.426	0.381	99.8	0.879	0.468
12-190	31.7	1.394	0.394	99.3	0.922	0.480
12-191	31.5	1.395	0.391	99.3	0.919	0.479
12-192	31.2	1.408	0.390	99.9	0.903	0.475
12-193	31.6	1.389	0.391	98.4	0.928	0.481
12-194	31.3	1.389	0.386	97.3	0.930	0.482
12-195	31.1	1.400	0.386	98.6	0.813	0.477
12-196	32.3	1.381	0.399	99.6	0.939	0.484
12-197	31.0	1.410	0.387	99.4	0.901	0.475
12-198	31.0	1.422	0.391	99.2	0.885	0.470
12-199	31.0	1.411	0.387	99.8	0.898	0.473
12-200	31.8	1.395	0.396	100.0	0.921	0.479
12-201	30.7	1.417	0.385	99.5	0.892	0.472
12-202	31.3	1.407	0.391	100.0	0.905	0.475
13-203	31.4	1.415	0.395	100.0	0.894	0.472
13-204	31.2	1.410	0.391	100.0	0.900	0.474
13-205	32.1	1.391	0.399	100.0	0.928	0.481
14-207	42.0	1.207	0.487	99.7	1.220	0.550
14-208	41.6	1.204	0.481	99.9	1.208	0.547
14-210	42.5	1.201	0.491	100.0	1.230	0.552
14-211	42.0	1.208	0.487	99.9	1.217	0.549
14-212	42.0	1.210	0.488	100.0	1.318	0.569
14-213	43.3	1.196	0.475	100.0	1.238	0.553
14-214	40.8	1.220	0.451	98.6	1.195	0.544
14-215	40.8	1.222	0.416	98.8	1.191	0.544
14-216	39.4	1.239	0.403	98.0	1.161	0.537
14-217	42.4	1.194	0.510	99.3	1.241	0.544
14-218	41.8	1.204	0.506	99.3	1.222	0.550
14-219	41.9	1.204	0.496	99.4	1.223	0.550
14-220	41.1	1.215	0.490	99.0	1.204	0.546
14-221	40.3	1.230	0.509	99.6	1.178	0.541
14-222	41.7	1.207	0.513	99.6	1.217	0.549
14-223	41.8	1.207	0.514	100.0	1.213	0.548

* The data for dry density γ_d were taken before testing.

† The volume ice content i_v is defined as

$$i_v = \frac{\text{Volume of ice}}{\text{Total volume of soil mass}}$$

and calculated by

$$i_v = \frac{(w - w_u)\,\gamma_d}{G_i\,\gamma_w}$$

where

G_i = specific gravity of ice, equal to 0.917

γ_w = unit weight of water, taken as 1 g/cm^3

w = water content (%)

w_u = unfrozen water content of samples, which can be found in Appendix A.

** The saturation degree s_i is defined as

$$s_i = \frac{\text{Volume of ice and unfrozen water}}{\text{Volume of pore}}$$

and calculated by

$$s_i = \frac{100[w-(1-G_i)w_u]G}{G_i\,e}$$

where G is the specific gravity of the soil particles, equal to 2.680, and e is the void ratio of samples.

*U.S. GOVERNMENT PRINTING OFFICE:1987-700-050:62022